Mi-2β-targeted inhibition induces immunotherapy response in melanoma

Bo Zhu
Harvard Medical School
Zhengyu Wang
University of Arkansas for Medical Science
Licheng Yao
Tsinghua University
Xingyu Lin
Tsinghua University
Jie Zhang
New Jersey Institute of Technology
Xin Li
Shanghai University of Traditional Chinese Medicine
James Hagman
National Jewish Health
Jingwei Shao
University of Arkansas for Medical Science
Phuc Tran
University of Arkansas for Medical Science
Meng Cao
Nanjing University of Chinese Medicine
Jianming Zhang
Shanghai JiaoTong University School of Medicine
Colin Goding
University of Oxford https://orcid.org/0000-0002-1614-3909
Xuebin Liao
Tsinghua University
Hong-yu Li
University of Arkansas for Medical Sciences
Peng Cao
Nanjing University of Chinese Medicine
Xiao Miao
Shanghai University of Traditional Chinese Medicine
Rutao Cui (✉ rutaocui@zju.edu.cn)

Zhejiang University

Article

Keywords: melanoma, immune checkpoint inhibitors, immunotherapy

Posted Date: December 16th, 2020

DOI: https://doi.org/10.21203/rs.3.rs-118153/v1

Mi-2β-targeted inhibition induces immunotherapy response in melanoma

Bo Zhu[1], Zhengyu Wang[2], Licheng Yao[3], Xingyu Lin[3], Jie Zhang[4], Xin Li[5], James R. Hagman[6], Jingwei Shao[2], Phuc D. Tran[2], Meng Cao[7], Jianming Zhang[8], Colin R. Goding[9], Xuebin Liao[3*], Hong-yu Li[2*], Peng Cao[7*], Xiao Miao[5*], Rutao Cui[10*]

[1]Department of Cancer Immunology and Virology, Dana Farber Cancer Institute, Harvard Medical School, Boston, MA 02115, USA

[2]Department of Pharmaceutical Sciences, College of Pharmacy, University of Arkansas for Medical Science, Little Rock, AR 72205, USA

[3]Key Laboratory of Bioorganic Phosphorus Chemistry and Chemical Biology, Beijing Advanced Innovation Center for Human Brain Protection, School of Pharmaceutical Sciences, Tsinghua University, Beijing 100084, China

[4]Adobe Inc., San Jose, CA 95110, USA

[5]Department of Dermatology, Yueyang Hospital of Integrated Traditional Chinese and Western Medicine, Shanghai University of Traditional Chinese Medicine, Shanghai 200437, China

[6]Department of Biomedical Research, National Jewish Health, Denver, CO 80206, USA

[7]1 Affiliated Hospital of Integrated Traditional Chinese and Western Medicine, School of Pharmacy, Nanjing University of Chinese Medicine, Nanjing 210023, China

[8]National Research Center for Translational Medicine, Shanghai State Key Laboratory of Medical Genomics, Rui-Jin Hospital, Shanghai JiaoTong University School of Medicine, 197 Ruijin second Rd， Shanghai 200025, China

[9]Ludwig Institute for Cancer Research, University of Oxford, Headington, Oxford OX3 7DQ, UK

[10]Skin Disease Institute, Department of Dermatology, The 2nd Hospital, School of Medicine, Zhejiang University, 88 Jiefang Road, Hangzhou, Zhejiang 310009, China

*To whom correspondence should be addressed, Rutao Cui: rutaocui@zju.edu.cn, Xiao Miao: 0000002623@shutcm.edu.cn, Peng Cao: cao_peng@njucm.edu.cn, Hong-yu Li: HLi2@uams.edu, and Xuebin Liao: liaoxuebin@mail.tsinghua.edu.cn

Abstract

Recent development of some new immune checkpoint inhibitors has been particularly successfully in melanoma, but the majority of melanoma patients exhibit resistance. Understanding and targeting the potential underlying mechanism/targets, especially the tumor-intrinsic modulators to convert resistant melanomas to immunotherapy sensitivity will potentially provide a significant improvement in patient outcome. Here, Mi-2β, a chromatin remodeling enzyme was identified as a key melanoma-intrinsic effector regulating the adaptive anti-tumor immune response. Loss of Mi-2β rescued the immune response to immunotherapy *in vivo*. Mechanistically, targeting Mi-2β induced the adaptive immune response by transcriptionally enhancing expression of a set of IFN-γ-responsive genes including CXCL9, CXCL10 and IRF1. Finally, we developed a Mi-2β-targeted inhibitor Z36-MP5, which specifically and effectively induced a response to immune checkpoint blockades in otherwise resistant melanomas. Our work provides a new insight into the epigenetic regulation in adaptive immune response, and highlights a viable strategy to improve immunotherapies in melanoma.

The cutaneous melanoma represents the most common form of melanoma and causes around 75% of deaths related to skin cancer [1]. Recent development of immunotherapies, especially some new immune checkpoint inhibitors, has been particularly successfully in melanoma. Since 2011, FDA and EMA have approved four new immunotherapies for advanced melanoma, including the anti-CTLA-4 antibody ipilimumab (Yervoy), the anti-PD-1 antibodies nivolumab (Opdivo) and pembrolizumab (Keytruda), and the oncolytic virus talimogene laherparepvec (TVEC, Imlygic) [2]. Clinical data shows that 20% of melanoma patients respond to ipilimumab (anti-CTLA-4) [3], 33% respond to pembrolizumab (anti-PD-1) [4] and 58% respond to a dual immune checkpoint blockade (anti-PD-1+anti-CTLA-4), but with significant toxicity [5, 6]. It is critical to note that even though most responsive cancer patients maintain long-lasting disease control, one third of those still relapse [7, 8].

Failure of immunotherapy is normally induced by: 1) poor pre-existing antitumor T cell immunity [9, 10], 2) inadequate function of tumor-specific T cells [11, 12], and 3) the impaired formation of T-cell memory [13, 14]. Most of studies have focused on identifying and overcoming T cell inhibitory mechanisms. However, the critical role of tumor-intrinsic modulation in regulating adaptive resistance to immune checkpoint blockades are getting more and more attentions [15]. Tumor-intrinsic interferon signaling has been demonstrated to control tumor sensitivity to T cell rejection and subsequently regulates adaptive resistance to immune checkpoint blockades [16, 17]. Furthermore, inhibition of p21-activated kinase 4 (PAK4) increased T cell infiltration and reversed resistance to PD-1 blockade through modulating WNT signaling [18]. *STK11/LKB1* alterations are the prevalent genomic driver for primary resistance to PD-1 inhibitors in *KRAS*-mutant lung adenocarcinoma [19]. In addition, the loss of PTEN decreases T-cell infiltration in tumors, causing reduced T cell-mediated cell death to enhance immune resistance [20]. Given the significance of chromatin in modulating gene expression and maintaining genome stability, some chromatin regulatory factors and enzymes are being identified to involve in the development of resistance to immunotherapies

[15]. For example, chromatin remodeling PBAF was found to contribute to cancer cell immune resistance [21, 22]. BRG1, a chromatin-remodeling enzyme, has also been implicated in enhancing IFN-stimulated gene transcription [23]. The overexpression of PRC2, a multiprotein enzyme complex (EZH2, SUz12, EED) regulating the trimethylation of lysine 27 on histone H3 (H3K27me3) [24] is detected in cancer cells and mediates the repression of IFN-γ-stimulated genes. Moreover, EZH2 inhibition enhances T cell-targeting immunotherapies in mouse models of melanoma [25, 26]. Interestingly, ARID1A, a member of the SWI/SNF family is found to interact with EZH2 to inhibit IFN-responsiveness gene expression in cancer cells, whose mutations can shape cancer immune phenotype and immunotherapy [27]

Here we find that Mi-2β played a key role in regulating adaptive immune response in melanoma. The human Mi-2β protein was discovered as autoantigens in dermatomyositis in 1995 [28]. Mi-2β, also named as CHD4 (chromodomain helicase DNA-binding protein 4), is a CHD family remodeling enzyme in the NuRD complex, which include the histone deacetylases 1 and 2 (HDAC1 and HDAC2), RBBP4/RBBP7, MBD2/MBD3, MTA-1/MTA-2/ MTA-3 and GATAD2A/B [29], and plays important roles in chromatin assembly, genomic stability and gene repression [30]. Chromatin remodeling enzymes dynamically modulate gene accessibility by using ATP-derived energy to change nucleosome occupancy, position and composition. They contain a highly conserved ATPase motor domain of helicase family, which are classified as SWR1, ISWI, INO80 and CHD according to the sequence homologous [31]. The well-studied function of Mi-2/NuRD is the indispensable role in cardiac muscle cell identity [32] and haematopoietic development, including T and B lymphocyte [33, 34, 35]. The conditional knockout of Mi-2β in mouse keratinocytes induced pro-inflammatory gene expression [36]. In cancer cells, Mi-2/NuRD processes tumor development and metastasis [37, 38]. We find that Mi-2β silencing induced the immune response of anti-PD-1 antibody treatment in "cold" melanoma *in vitro* and *in vivo*, and the effects were directly mediated by factors in IFN-γ signaling, such as Irf1, Cxcl9 and Cxcl10. Moreover, we developed a specific Mi-2β-targeted inhibitor Z36-MP5. Treatment of Z36-MP5 induced response of immune checkpoint blockades in “cold” melanoma *in vivo*. Our work provides new insights into the epigenetic regulation in adaptive immune response in melanoma and developed a new immune therapeutic strategy in melanoma.

Results

Tumor intrinsic expression of Mi-2β modulates resistance to T cell-mediated killing in melanoma.

Cytotoxic T cells are key effectors to detect and eliminate transformed tumor cells. However, some tumors are lacking T cells infiltration (cold tumor) and subsequently adaptive immune response, including response of the treatment of immune checkpoint blockades [39]. More and more evidence indicate that tumor-intrinsic chromatin regulatory factors are crucial in regulating adaptive immune response in melanoma [15]. We therefore focused on identifying tumor-intrinsic epigenetic factors which are crucial in regulating adaptive immune response in melanoma. To preliminarily identify the key epigenetic factors that regulate cell sensitivity and resistance to T cell-mediated attack in melanoma, we analyzed the hazard ratio of the different epigenetic factors in melanoma with different levels of T cell infiltrations. Tumor-intrinsic CD8 levels served as a marker to indicate T cell infiltration [40]. Epigenetic factors were preliminarily recognized as a potential regulator of immune response if its expression level was significantly correlated with hazard ratio in patients with high CD8 T cell infiltration only, but not in patients with low CD8 T cell infiltration. Fifty-five epigenetic factors were identified (**Extended Data Fig. 1a**). The melanoma and T cell co-culture system was used to further identify the role of the most correlated genes (n=18) identified in the hazard ratio analysis in regulating T cell mediated cytotoxicity. In this co-culture system, B16F10 melanoma cells and the activated Pmel-1 T cells were co-cultured. Pmel-1 T cells carry a rearranged T cell receptor transgene specific for the mouse homologue of human pre-melanosome protein of gp100 [41], and B16F10 cells are resistant to immunotherapies, including checkpoint blockade antibodies against PD-1 [42, 43]. Each candidate gene was silenced by specific gRNA and labeled by GFP in B16F10 cells. The resulted B16F10 cells were mixed with no labeled parent control B16F10 cells (1:1) and then co-cultured with the activated Pmel-1 cells. The number of GFP^+ cells were detected by flow cytometry to determine B16F10 cell response to cytotoxic T cells (**Fig. 1a**). *Mi-2β, Eif4a1, USP7* or *Parp1* silencing significantly induced the response to T cell attack in melanoma cells, and led more than half of melanoma cells to be eliminated by Pmel-1 T cell-mediated killing (**Fig. 1b**). Mi-2β was picked for further analysis due to the epidermal inflammation phenotypes in conditional keratinocyte-specific Mi-2β knockout mouse [36]. Mi-2β is a chromatin remodeling enzyme with a SNF2-like ATPase domain and plays critical roles in chromatin assembly and genomic stability. To validate the significance of Mi-2β in regulating immune microenvironment in human melanoma, the correlations between Mi-2β mRNA level and CD8A and CD8B mRNA levels were first analyzed in melanoma patients collected in The Cancer Genome Atlas (TCGA). Mi-2β mRNA level was negatively correlated with both CD8A and CD8B mRNA levels ($p<0.01$) (**Fig. 1c**). These results indicate that lower Mi-2β expression correlates with enrichment of CD8 T cell infiltration in melanoma. Next, to identify the role of Mi-2β in the immune response in melanoma, the correlations between Mi-2β and GZMB or PRF1 were analyzed. GZMB and PRF1 are crucial for the rapid induction of target cell apoptosis by cytotoxic T lymphocytes (CTL) in cell-mediated immune response [44]. Mi-2β mRNA level was also negatively correlated with both GZMB and PRF1 mRNA level ($p<0.01$) in melanoma (**Fig. 1d**). These results suggest that expression levels of Mi-2β are associated with T cell-mediated killing in melanoma. Consistently, the repression of Mi-2β expression were found to correlate with a substantial survival benefits only in melanoma patients with higher CD8 T cell infiltration ($p<0.05$), but not in melanoma with low CD8 T cell infiltration (**Fig. 1e**). To further validate the role of Mi-2β in modulating sensitivity to T cell-mediated killing in melanoma, the melanoma-T-cell co-culture system (B16F10/Pmel-1) was used. Mi-2β silencing (**Extended Data Fig. 1b**) induced T cell-mediated cytotoxicity *in vitro* (**Fig. 1f**). All these results demonstrate the critical role of Mi-2β in regulating melanoma resistance to T cell-meditated cytotoxicity. Tumor intrinsic Mi-2β level regulates melanoma sensitivity to the anti-tumor immunotherapy.

Mi-2β silencing synergizes with immune checkpoint blockades to promote anti-tumor immunity. To identify whether Mi-2β depletion induced immune response in B16F10 melanoma cells, mouse graft melanomas with shMi-2β virus-infected B16F10 cells were treated by anti-PD-1 antibodies (10mg/kg) at day 6, 9, 12, 15 and 18 after tumor cell inoculation in immunocompetent C57BL/6 mice. In consistence with the previous reports [18, 43], mice injected with control B16F10 cells with shScramble were not sensitive to anti-PD-1 treatment. However, Mi-2β silencing combined with anti-PD-1 treatment conferred a substantial inhibition on the tumor growth in B16F10 melanoma (**Fig. 2a-b**), and subsequently extended the survival of the treated mice (**Fig. 2c**). Analysis of graft tumor microenvironment by flow cytometry (**Extended Data Fig. 2a**) shows that increases of $CD8^+$ and $CD4^+$ T cell infiltration were detected in B16F10 tumor graft with Mi-2β silencing, which was strongly augmented by the anti-PD-1 treatment (**Fig. 2d**).

At the same time, a minor, but non-significant, increase in tumor-infiltrating Treg cells was also detected in the B16F10 tumor graft following Mi-2β silencing, which was not inhibited by anti-PD-1 treatment and/or Mi-2β silencing (**Extended Data Fig. 2b**). Moreover, a minor to medium increase of GZMB expression and upregulation of activation of CD69, IFN-γ, CD25 and CD107 were detected in tumor-infiltrating $CD8^+$ T cells of B16F10 tumor graft with Mi-2β silencing, which were strongly augmented by anti-PD-1 treatment (**Fig. 2e-f**). All these data indicate that Mi-2β silencing sensitizes tumor cells and confers a more favorable tumor microenvironment to induce an adaptive immune response to immune checkpoint blockades treatment in melanoma.

Loss of Mi-2β induces responses to immune checkpoint blockades in BRaf^{V600E}/Pten^{null} melanoma *in vivo*. To further examine whether Mi-2β depletion induced an adaptive immune response in melanoma *in vivo, Tyr::CreER;BRaf^{CA};Pten$^{lox/lox}$* mice were used for anti-PD-1 antibody experimental treatment. In this mouse strain, induction of Cre-mediated recombination leads to Braf^{V600E} expression and Pten inactivation (BRaf^{V600E}/Pten^{null}) in cutaneous melanocytes, which results in rapidly progression of malignant melanoma [45]. *Mi-2β$^{lox/lox}$* mice [36] were crossed with *Tyr::CreER;BRaf^{CA};Pten$^{lox/lox}$* mice to deplete *Mi*-2β in BRaf^{V600E}/Pten^{null} melanoma after the tamoxifen injection. Mice with visible melanomas were randomly treated with either control IgG antibodies (10mg/kg) or anti-PD-1 (10mg/kg) starting at day 9, 12, 15, 18 and 21 after Cre activation (**Fig. 3a**). The tumor free survival was analyzed. In consistence with the previous reports [20], BRaf^{V600E}/Pten^{null} melanoma is a kind of "cold" tumor and was insensitive to anti-PD-1 antibody treatment, and there was no significant difference of mouse free survival observed in BRaf^{V600E}/Pten^{null} melanoma with different *Mi-2β* status (**Fig. 3b**). IHC staining for the melanoma marker S100 and proliferation marker Ki-67 showed no difference between BRaf^{V600E}/Pten^{null} melanomas with different Mi-2β status (**Extended Data Fig. 3a-b**). Intriguingly, treatment of anti-PD-1 significantly extended the mouse survival with BRaf^{V600E}/Pten^{null}/Mi-2β^{null} melanoma compared with that of BRaf^{V600E}/Pten^{null} melanoma (**Fig. 3b**). To further identify whether Mi-2β knockout-induced anti-PD-1 response correlates with T cell activation, tumor-infiltrating lymphocytes (TILs) were measured in BRaf^{V600E}/Pten^{null} melanomas with different Mi-2β status by flow cytometry. The populations of infiltrating CD8^{+} and CD4^{+} T cells were minorly increased in TILs of BRaf^{V600E}/Pten^{null}/Mi-2β^{null} melanoma. This increase was significantly augmented by the anti-PD-1 treatment (**Fig. 3c-d**). At the same time, a minor, but not-significant, increase in the Treg population was also detected in BRaf^{V600E}/Pten^{null} melanoma after Mi-2β knockout. However, the anti-PD-1 treatment did not change Treg cell population in BRaf^{V600E}/Pten^{null}melanomas significantly after Mi-2β knockout (**Extended Data Fig. 3c**). Moreover, an increase of GZMB expression and upregulation of $CD8^+$ T cell activation markers, such as CD69, IFN-γ, CD25 and CD107, were detected in $BRaf^{V600E}/Pten^{null}/Mi\text{-}2\beta^{null}$ melanomas after Mi-2β knockout. These increase were all further strongly augmented by anti-PD-1 treatment (**Fig. 3e-f**). Taken together, all these results indicate that loss of Mi-2β in melanocytes activates CTLs to induce response of anti-PD-1 treatment in "cold" melanoma *in vivo*.

Mi-2β-regulated immune response is mainly mediated by IFN-γ signaling pathways. To identify how Mi-2β regulated immune response is mediated in melanoma, Mi-2β-CRISPR/Cas9-knocked and IFN-γ-treated B16F10 cells [46] were used to perform microarray assay. The expressions of 1209 genes were identified to be significantly repressed (>1.5 folds, $p<0.05$), and the expressions of 1283 genes were identified to be significantly up-regulated (>1.5 folds, $p<0.05$) after Mi-2β silencing. The deregulated genes identified were further analyzed by Gene Set Enrichment Analysis (GSEA) to identify Mi-2β-regulated gene sets and pathways. Interestingly, IFN-γ signal was activated after Mi-2β knockout (**Fig. 4a and Extended Data Table 1-2**). IFN-γ production is essential in the response to immunotherapy, especially in patients with melanoma [47, 48]. Many of Mi-2β-controlled IFN-γ-responsive genes, such as *Cxcl9, Cxcl10, CD74, Irf1, and CD40*, functions in T cell chemoattractant, antigen presentation, and T cell targeting and activation (**Fig. 4b**). Specifically, cytokine expressions, such as *Cxcl9, Cxcl10, Cxcl11* and *Ccl5* were upregulated by Mi-2β silencing (**Fig. 4b**), and these cytokines are crucial in inducing and recruiting effector T cells with CXCR3 chemokine receptor into tumor microenvironment to induce anti-tumor immunity [47, 48, 49]. Several antigen presentation genes, such as *Tap1* and *CD74* and some regulators involving in tumor cell immunogenicity, such as *Irf1*, *Icam1* and *CD40* were also upregulated by Mi-2β knockout *in vitro* (**Fig. 4b**).

To confirm the regulation of Mi-2β on those downstream targets in IFN-γ pathways, the expressions of ISGs in IFN-γ pathway were measured in B16F10 cells with Mi-2β silencing. Mi-2β silencing significantly upregulated the mRNA expressions of *Cxcl9, Cxcl10, Cxcl11, Ccl5, Tap1, CD74, Irf1, Icam1, CD40, Fas* and *PD-L1* (**Fig. 4c**), and enhanced the paracrine secretions of Cxcl9 and Cxcl10 both before and after addition of IFN-γ (**Fig. 4d-e**). *In vivo*, TIMER analysis [50] indicated that Mi-2β mRNA level negatively correlated with CCL5, CD74 and CD40 mRNA level in melanoma patients collected in TCGA melanoma cohort ($p<0.01$) (**Extended Data Fig. 4a**). These data indicate that Mi-2β-regulated immune response is mediated by IFN-γ signaling pathways in melanoma. To identify how Mi-2β involves in the responses of anti-PD-1 treatment, the expression levels of Cxcl9 and Cxcl10 were measured with ELISA assay in melanomas collected in Fig. 2C-D. Upregulation of Cxcl9 and Cxcl10 were detected after Mi-2β silencing and the anti-PD-1 treatment in melanomas (**Fig. 4f-g**). In addition, we also measured these factors in the downstream targets of IFN-γ pathways in BRaf^{V600E}/Pten^{null} melanoma collected in Fig. 3B. Upregulation of *Cxcl9, Cxcl10, Cxcl11, Ccl5, Tap1, CD74, Irf1, Icam1, CD40, Fas* and *PD-L1* were detected after Mi-2β silencing and the anti-PD-1 treatment in BRaf^{V600E}/Pten^{null} melanomas (**Extended Data Fig. 4b**).

Mi-2β, a member of the SNF2/RAD54 helicase family, is a main component of the nucleosome remodeling and deacetylase complex. Mi-2β are highly enhanced at the transcription starting sites and plays an important role in the epigenetic transcriptional repression [51]. To investigate the molecular mechanisms underlying Mi-2β-regulated repression of factors in IFN-γ pathways, chromatin immunoprecipitation (ChIP) assays were performed to identify whether Mi-2β protein binds to the promoters of *Cxcl9, Cxcl10* and *Irf1*. We found that Mi-2β bound to promoters of *Cxcl9, Cxcl10* and *Irf1,* with anti-Stat1 served as a positive control (**Extended Data Fig. 4c-e**). These data indicate that Mi-2β is directly involved in regulating transcription of *Irf1, Cxcl9* and *Cxcl10.*

Development of Z36-MP5 as a specific small molecule inhibitor targeting Mi-2β. Given the pivotal role of Mi-2β in regulating immune response, targeting Mi-2β would represent a potential therapeutic strategy in melanoma immunotherapy, especially in combination with immune checkpoint blockades. To screen small molecules that inhibit Mi-2β activity, Homology Modeling was carried out using Structure Prediction Wizard in Prime [52, 53]. Mi-2β belongs to the CHD family of chromatin remodelers, which share the highly conserved ATPase/helicase domains [54, 55]. The Homology Model of Mi-2β was generated using the yeast CHD1 structure (PDB code: 3MWY) as template and the receptor sequence was obtained from Uniprot [56], which clearly depicted the interaction of Mi-2β binding pocket and ATP (**Extended Data Fig. 5a**). Virtual screening was done with enzyme hinge region ligands database and nucleoside mimetic database from Enamine. All ligands of ~23,010 compounds were docked to the ATP binding site using SP docking and post-processed with Prime MM-GBSA. The ligands with methyldihydroimidazopyridinone structure were predicted to bind best to ATP warhead binding region of Mi-2β. To biochemically analyze the inhibitory activity of those inhibitors, a Fluorescence Resonance Energy Transfer (FRET)-based nucleosome repositioning assay [57, 58] was designed and modified using recombinant purified human Mi-2β protein to screen an in-house library of small molecular compounds with methyldihydroimidazopyridinone structure (**Fig. 5a**). Briefly, the recombinant nucleosome substrates consist of a Cy5-labeled human histone octamer (H2A T120C-Cy5) wrapped with 5' Cy3-labeled DNA, which contains a terminal nucleosome 601 positioning sequence. The 601 sequence provides the most preferred locations on DNA for histone octamer thermodynamically [59]. The FRET signaling was monitored by exciting the nucleosomes at the Cy3 absorption maximum and measuring the Cy5 emissions. FRET signaling is at a maximum level at the assembled starting point. The chromatin remodeler Mi-2β modulates histone octamer to move along the DNA in the presence of ATP. Therefore, Cy3-labeled DNA

5’ end is moved away from the Cy5-labeled octamer and consequently the FRET signal is decreased (**Fig. 5a**). The reaction conditions of nucleosome repositioning were modified through multiple rounds of optimization and validation (**Extended Data Fig. 5b-c**). Z36 was initially identified as the best hit with IC50 values of 6.971 ± 2.072 μM (**Extended Data Fig. 5d**). Structure Activity Relationship (SAR) studies were further used to improve the specificity and efficacy of Z36 for Mi-2β inhibition. Through iterative rounds of structure-activity optimization and *in vitro* assay screens, Z36-MP5 (**Fig. 5b**) was identified to have a high inhibitory activity on Mi-2β function where it was predicted to docked into the ATP binding pocket of Mi-2β (**Fig. 5c**), with its methyl group extended to a solvent-exposed channel lined with the side chains of Tyr729, Leu755, Met966, and Ile1163. Z36-MP5 could generate H-bonds with Mi-2β via the O atom of keto group with His727, O atom of amide group with Gly756, and protonated N atom of imidazole group with Asp873. *In vitro* assay indicated that Z36-MP5 had an efficient IC50 values of 0.082 ± 0.013 μM against Mi-2β (**Fig. 5d**), ~85 folds more inhibitory potential than the original compound Z36. Moreover, an ATP acyl phosphate probe assay [60] was performed by ActivX Biosciences to profile of Z36-MP5 inhibition on ATPases in native cell lysates, in which the protein-protein interactions remained intact. Z36-MP5 showed less than 35% inhibition at a concentration of 1 μM against a panel of 233 diverse ATPases (**Extended Data Table 3**). These results suggest that Z36-MP5 has a high Mi-2β ATPase selectivity and specificity.

Z36-MP5 was chosen for further validation and experimental therapeutics *in vivo*. The IC_{50} of Z36-MP5 against Mi-2β was increased with increasing concentration of ATP (10 μM to 300 μM) (**Fig. 5e**), suggesting Z36-MP5 functions as an ATP-competitive inhibitor. To investigate the cellular inhibitory activity, B16-F10 cells were treated with Z36-MP5 at variety of concentrations ranging from 5 to 100 μM, and the activation of Mi-2β target genes were measured by RT-qPCR. Z36-MP5 stimulation (25 μM) inhibited Mi-2β function to recover target gene expressions, such as *Cxcl9*, *Cxcl10* and *Irf1* (**Fig. 5f**) in

B16F10 cells, indicating its high inhibitory capacity. We also performed the co-culture assay of B16F10 and activated Pmel-1 T cells to identify whether Z36-MP5 stimulation activates T cell mediated cytotoxicity. Z36-MP5 stimulation significantly induced T cell-mediated killing of B16F10 cells (**Fig. 5g**). Importantly, monitoring mouse weight (**Extended Data Fig. 5e**) and organ tissue histological staining (**Extended Data Fig. 5f**) showed Z36-MP5 treatment was tolerated without significant toxicity in C57BL/6 mice. In addition, the pharmacokinetic properties of Z36-MP5 in Sprague-Dawley rats with administration of intraperitoneal injection dose of 1.0 mg/kg. The results showed that Z36-MP5 exhibited favorable pharmacokinetic parameters with a half-life $T_{1/2}$ of 0.45 hours and C_{max} of 3.96 μg/mL (**Extended Data Fig. 5g**). These data suggest that Z36-MP5 is a potent and effective inhibitor for Mi-2β and stimulates T cell mediated cytotoxicity *in vitro*, which warranted further *in vivo* studies.

Z36-MP5 induces melanoma response to immune checkpoint blockades *in vivo*. To determine whether Z36-MP5 represented a potential therapeutic option for melanoma immunotherapy, especially in combination with anti-PD-1 treatment *in vivo*, syngeneic mouse melanoma developed by subcutaneously grafted B16F10 in C57BL/6 mice were randomly treated with Z36-MP5 (30 mg/kg) and/or anti-PD-1 (10mg/kg) accordingly. The results showed that only the combinational treatment of Z36-MP5 and anti-PD-1 conferred a substantial inhibition on tumor growth (**Fig. 6a-b**) and extended mouse survival (**Fig. 6c**) compared with control treatment. Treatment with Z36-MP5 or anti-PD-1 alone did not impact tumor growth or mouse survival.

Z36-MP5 treatment alone induced a moderate increase in the $CD8^+$ T cell TILs in graft melanomas that was augmented by combining with anti-PD-1 therapy (**Fig. 6d and Extended Data Fig. 6a**). However, the population of $CD4^+$ T cell and Treg cells were not changed significantly by either the individual or combinational treatments (**Extended Data Fig. 6b-c**). An upregulation of GZMB expression in tumor-infiltrating CD8$^+$ T cells was detected in tumors treated with Z36-MP5, as well as the activation markers CD69, IFN-γ, CD25 and CD107, which increase was also augmented by the combinational treatment of anti-PD-1 (**Fig. 6e-f**). These results indicate that Z36-MP5 represents an effectively combinational therapeutic option of anti-PD-1 treatment in melanoma.

Z36-MP5 therapy potential was further tested in the *Tyr::CreER;BRaf*^{CA}*;Pten*$^{lox/lox}$ mouse melanoma. After tamoxifen administration, mice with visible melanomas were randomly treated with Z36-MP5 (30mg/kg) once a day starting at day 9 and/or anti-PD-1 (10mg/kg) five times at day 9, 12, 15, 18 and 21 after Cre activation. Z36-MP5 in combination with the anti-PD-1 antibody treatment significantly extended the mice tumor survival in BRaf^{V600E}/Pten^{null} melanoma mice (**Fig. 6g**). However, Z36-MP5 or anti-PD-1 treatment alone cannot extend the tumor free survival in BRaf^{V600E}/Pten^{null} mice, which is consistent with the previous reports that BRaf^{V600E}/Pten^{null} melanoma was insensitive to anti-PD-1 treatment [20] (**Fig. 6g**). To identify the role of Z36-MP5 treatment in regulating tumor immune microenvironment, TILs were collected and assayed with flow cytometry. Z36-MP5 treatment alone moderately induced CD8$^+$ T cell population, which was further augmented by anti-PD-1 treatment (**Fig. 6h**). However, the CD4$^+$ T cell and Treg populations in BRaf^{V600E}/Pten^{null} mouse melanomas were not affected by either Z36-MP5 alone or in combination with anti-PD-1 treatment in BRaf^{V600E}/Pten^{null} melanoma (**Extended Data Fig. 6d-6e)**. An increased expression of GZMB, CD69, IFN-γ, CD25 or CD107 in CD8$^+$ T cells was detected in BRaf^{V600E}/Pten^{null} melanoma, and their induction was further augmented by the anti-PD-1 treatment (**Fig. 6i-6j and Extended Data Fig. 6f**). These data indicate that Z36-MP5 treatment confers a more favorable tumor microenvironment to cytotoxic CD8$^+$ T cells for overcoming the resistance of melanoma to anti-PD-1 treatment.

Discussion

Given heterogeneity of cancer cells and dynamic evolvement of tumor microenvironment, identifying and demonstrating the potential regulatory factors, which target and modulate interferon signaling pathways and antigen presentation, will be promising in inducing response, or resistance recovery in cancer immunotherapy. Tumor cell-intrinsic resistance mechanisms of immunotherapies are deeply explored and identified, including processing and presentation of neoantigen by the major histocompatibility complex (MHC) [61, 62] and absence of pre-existing T cell infiltration caused by a lack of T cell-recognized antigens [63] or MHC [14]. Melanoma-intrinsic Wnt pathway was demonstrated to contribute to a lack of T cell-melanoma recognition to prevent anti-tumor immunity [64]. The alteration of antigen presentation also regulates the interaction and recognition of tumor cell and T cell recognition, and of interferon signaling pathways to induce resistance of immunotherapy [7].

Over recent years there has been increasing evidence that some chromatin regulatory factors are crucial in regulating resistance to anti-PD-1 antibody treatment in melanoma, [15], such as EZH2 [26] and ARID1A [27]. EZH2 inhibition enhances T cell-targeting immunotherapies *in vivo* [25, 26] whereas ARID1A interacts with EZH2 to inhibit IFN-response gene expression in cancer cells [27]. In addition, the PBAF form of the SWI/SNF chromatin remodeling complex, especially the Pbrm1, Arid2, and Brd7 components, regulate tumor cell resistance to T cell-mediated killing through control of interferon-stimulated gene (ISG) expression. The expression of PBRM1 and ARID2 inhibits the expression of T cell cytotoxicity genes and subsequent repress infiltrated cytotoxic T cells [21, 22]. Mutations in other PBAF complex members, such as ARID2 and BRD7, occur in melanoma and overcome resistance of tumor cells to T cell-mediated cytotoxicity [22, 65]. Here we show that Mi-2β, a chromatin remodeling enzyme, regulates resistance to T cell-mediated cytotoxicity and immunotherapy.

A successful anti-tumor immune response following immune checkpoint blockades is believed to require reactivation and proliferation of clone of antigen-experienced T cells in the tumor microenvironment [14, 66]. Inadequate anti-tumor T-cell effector function may preclude proper T cell function to limit the efficacy of immune checkpoint inhibitors [14, 67]. Those important factors include high levels of immune suppressive cytokines or chemokines, and recruitment of immune suppressive cells, such as myeloid-derived suppressor cells (MDSCs) and regulatory T cells (Tregs) [66]. Our data show that depletion or inhibition of a cancer cell-intrinsic epigenetic modulator, Mi-2β, changes the tumor microenvironment to fuel CD8 T cell-mediated anti-tumor immunity, at least in part because Mi-2β is involved in suppression of genes downstream from IFN-γ, and IFN-α signaling.

Mi-2β functions in chromatin assembly, genomic stability and transcriptional repression [30]. Our data indicates that Mi-2β inhibition is directly involved in transcriptional activation of cytokines in IFN-γ pathways, such as Irf1, CXCL5, CXCL9 and CXCL10 and synergizes with anti-PD-1 treatment-induced checkpoint blockage to induce CTL to overcome the resistance to anti-PD-1 treatment. All these cytokines are crucial in inducing and recruiting effector T cells with CXCR3 chemokine receptor into tumor microenvironment to induce anti-tumor immunity [47, 48, 49]. The tumor-intrinsic CCL5 is required in T cell infiltration. In addition, CXCL9 induces T cell infiltration. Thus, co-expression of CCL5 and CXCL9 usually indicates tumor response to the immune checkpoint blockade treatment [68]. Antigen presentation genes, such as *TAP1* and *CD74,* and regulatory genes of tumor cell immunogenicity, such as *Irf1*, *Icam1* and *CD40* are also regulated by Mi-2β, all of which are crucial in regulating immune response in melanoma. Specifically, TAP1 is a key factor to specifically restrict anti-tumor responses through recognizing MHC-1/β2m-peptide complex on tumor surface in immunotherapy [69, 70, 71]. At the same time, CD74 plays a role in cross-presentation on HLA class I molecules to contribute cytotoxic T cell antitumor response [72]. One recent report indicates that the acquired resistance of anti-PD-1 treatment is associated with defects in interferon-receptor signaling (mutations in JAK1/2) and antigen presentation (B2M) [47].

JAK1/2 loss-of-function mutations result into a lack response to IFN-γ, also causing a primary resistance to PD-1 blockade therapy [73].

Our microarray data indicates that other signaling pathways, including TNF, NF-κB and PD-L1/PD-1 signaling pathways are also regulated by Mi-2β and contribute to Mi-2β-regulated immune responses. The selective reducing TNF cytotoxicity threshold has been demonstrated to increase the response to immunotherapy in a complementary research with genome-wide CRISPR/Cas9 screen [74]. With a pooled *in vivo* genetic screening approach using CRISPR-Cas9 genome editing, genes involved in NF-κB signaling are also identified to be a resistant mechanism to immunotherapy [75]. In addition, decoupling NF-κB signaling from cell dying of necroptosis or inflammatory apoptosis reduces $CD8^+$ T cell cross-priming efficiency and anti-tumor immunity, suggesting a possible mechanism for NF-κB role in orchestrating immunotherapy [76]. Metastatic melanoma was reported to release extracellular vesicles with PD-L1 on their surface, which suppresses CD8 T cell anti-tumor immunity [77].

Targeted therapies have significantly improved clinical outcomes in patients with various cancers including BRAF and MEK/ERK inhibitors in metastatic melanoma [78, 79, 80]. Targeted therapies have been tested widely in combination with anti-PD-1 therapies, and substantially contribute to anti-tumor immunity with immunotherapy [14, 81, 82], including by increasing tumor antigen expression [83, 84], enhancing the function of effector T cells [85, 86], and overcoming the immune suppressive microenvironment of tumor [87, 88]. A variety of clinical trials using a combination of MAPK pathway targeted therapy and immunotherapy in advanced metastatic melanoma have been performed and evaluated [89]. However, unexpected toxic side effects are reported in combinational clinical trials [90, 91, 92]. In addition, the immune microenvironment is a source of resistance to MAPK pathway-targeted therapy which is reinforced during combinational treatment, while on the other hand, the increased TNF-α signaling and tumor-associated macrophages following MAPK blockade may be involved in developing an immunosuppressive tumor microenvironment [93]. Here, we developed an effective inhibitor (Z36-MP5) to target Mi-2β ATPase activity. Using both syngeneic and transgenic mouse models, Z36-MP5 induced a response of otherwise anti-PD-1-resistant melanoma to immunotherapy through rescue of interferon-stimulated gene (ISG) expression. The ability to target Mi-2β and recover ISG and inflammatory signals by Z36-MP5 might be further evaluated for integration of combinational immunotherapy in patients with melanoma and other immune resistant cancers in future translational and clinical researches.

Methods

Plasmids and shRNAs. The plasmid of Flag-Mi-2β was generously provided by Dr. Joel Mackay in University of Sydney. To knockdown Mi-2β in B16F10 melanoma cells, mouse specific short hairpin RNAs of TRC Lentiviral Mouse Mi-2β shRNA (TRCN0000086143: TTTACAACTCAGAAGATGGGC and TRCN0000086146: TAAGTTGTGGAACCTCTCAGG) (Open Biosystems- Horizon Discovery) targeting Mi-2β were co-transfected with psPAX2 (Addgene, 12260) and pMD2.G (Addgene, 12259) into HEK293FT cells using Lipofectamine 3000. Lentiviruses were harvested 48 h after the transfection, and then used to infected B16F10 cells for 24 h in the presence of 8 μg/mL polybrene. The infected cells were selected by 2 μg/mL puromycin.

LentiCRISPR v2 constructs for knockout mouse Mi-2β were generated following the online guide of CHOPCHOP (https://chopchop.rc.fas.harvard.edu/) [46]. Briefly, HEK293FT cells in 6-well plates were transfected with 1.5 μg lentiviral plasmid, 1 μg psPAX2, and 0.5 μg pMD2.G. Lentivirus were collected after 2 days after transfections, and then filtered through a 0.45 μm filter. B61F10 Cells were infected with lentivirus for 24 hours, and then refed with fresh medium and selected with 2 μg/mL puromycin.

Cell culture. B16F10 cells were cultured in complete DMEM media (10% FBS and 100U/ml of Penicillin-Streptomycin). B16F10-shMi-2β and B16F10-shScramble cells were maintained in complete DMEM media (10% FBS and 100U/ml of Penicillin-Streptomycin) with 2-5ug/ml of puromycin. CD8 T cells isolated from mice were cultured in complete RPMI 1640 media (10%FBS, 0.05mM 2-mercaptoethanol, 20mM HEPES, 2mM Lglutamine, 1mM sodium pyruvateand 100U/ml streptomycin and penicillin).

Isolation and activation of Pmel-1 T cells. Pmel-1 TCR transgenic mice were purchased from Jackson Laboratory (stock #005023). The CD8 T cells were isolated from spleen and lymph nodes from Pmel-1 transgenic mice using the CD8a$^+$ T Cell Isolation Kit, mouse (Miltenyi Biotec, Order no: 130-104-075) according to the manufacturer's protocol. Freshly isolated CD8 T cells were stimulated with anti-CD3/CD28 beads (Thermo Fisher Scientific #11452D) for 3 days, and then the recombinant mouse IL-2 (Biolegend, #575406) was added at 20ng/ml. After 6 days activation, T cells were used for co-culture with B16F10 cells.

Co-culture assay of B16F10 cells with activated Pmel-1 T cells. B16F10 cells with shMi-2β or shScrambles were transfected with GFP expression vector pcDNA3-EGFP (Plasmid #13031), and the stable cell line was selection with 800 µg/mL G418. For *in vitro* validation, Mi-2β-deficient B16F10 cells (GFP positive) were mixed with control B16F10 cells (GFP negative) at a 1:1 ratio. The cells were treated with 10ng/ml of IFN-γ for 24 hours, and then co-cultured with activated Pmel-1 T cells. After three days, the depletion of Mi-2β knockdown B16F10 cells was determined by FACS, comparing the percentage of knockdown cells (GFP positive) to control B16F10 cells (GFP negative).

Quantitative real-time PCR (RT-qPCR). The total RNA was extracted with QIAGEN RNeasy kit (Invitrogen) for cDNA synthesis with SuperScript II Reverse Transcriptase (Invitrogen). In total, 40 ng cDNA was used for quantitative real-time PCR amplification by TaqMan Gene Expression Master Mix (Thermo Fisher Scientific). The relative transcript levels were normalized with GAPDH expression. The data were calculated with the comparative CT method.

Immunoblot analysis. The lysis buffer (50 mM Tris pH 7.4, 1% Triton X-100, 0.5 mM EDTA, 0.5 mM EGTA,150 mM NaCl, 10% glycerol, 1 mM phenylmethylsulfonyl fluoride and complete protease inhibitor cocktail (Roche)) were used to prepare the whole cell lysates, which was followed by homogenization and centrifuge (14,000 rpm for 15 min at 4° C). Pierce BCA Protein Assay Kit (Thermo Fisher Scientific) was used to detect protein concentration. After SDS-PAGE separation and PVDF membrane (BIO-RAD) transfer of the proteins, the specific primary was probed at 4° C for overnight, before incubated with corresponding horseradish peroxidase (HRP)-conjugated 2nd antibodies. Pierce ECL Western Blotting Substrate (Thermo Fisher Scientific) was used for protein detection. Antibodies were: anti-Mi-2β (ab70469, Abcam) (1:1000), anti-β-actin-peroxidase antibody (AC15) (1:5000, Sigma-Aldrich) and anti-rabbit secondary antibody (A-4914) (1:10000, Sigma-Aldrich).

Chromatin immunoprecipitation (ChIP) assays. ChIP assays were performed and analyzed as previous description [94]. Briefly, B16F10 cells (~1×10^7) were incubated with 1% formaldehyde for 10 minutes for crosslink, with adding glycine for a final concentration of 0.125 M to stop crosslink. Then the nuclear pellets were prepared, and suspended with ChIP lysis buffer. The DNA was fragmented with sonication. Immunoprecipitation was performed with antibodies anti-Mi-2β (ab70469, Abcam), anti-Stat1 (ab239360, Abcam) and IgG control at 4 °C for overnight. The complex was pulled down with A/G agarose beads (#20422, Thermo Fisher Scientific) and crosslink was reversed with heating at 65 °C for overnight. The DNA was purified and eluted for quantitative PCR assay. Primers were designed based on the binding peak analysis with ChIP-Atlas-Peak Browser. All data were normalized to gene desert regions of the IgH loci. The real time PCR was performed in triplicate. Values of [Δ][Δ] Ct method was used to calculate the relative binding enrichment, with the formula: Ct, template (antibody) − Ct, template (IgG) = [Δ] Ct, and the fold enrichments ([Δ][Δ]Ct) were determined using the formula of 2-[Δ] Ct. (experimental)/2-[Δ] Ct (IgH). Standard error from the mean was calculated from replicate [Δ][Δ] Ct values from independent experiments. Primers for Mi-2β ChIP include *Cxcl9* promoter forward: 5’-AGTGCACAGCATCGGTTGAG-3’, *Cxcl9* promoter reverse: 5’-TGTAAAGGGGATTCTGGGTGC-3’;

Cxcl10 promoter forward: 5’-AAAATGACGGCAGCACTTGG-3’, *Cxcl10* promoter reverse: 5’-AGCCAATCAGGACTCAGGGA-3’; *Irf1* promoter forward: 5’-GACCATCATAGGAGCCAGCA-3’, *Irf1* promoter reverse: 5’-TGTTGTAGAGCTAAGCGGCG-3’, and primers for Stat1 ChIP include *Cxcl9* promoter forward: 5’-CGTCCTGGGGAAAACCCTAC-3’, *Cxcl9* promoter reverse: 5’-GGGGTGGTTTCACATCCCTT-3’; *Cxcl10* promoter forward: 5’-CCCTGAGTCCTGATTGGCTG-3’, *Cxcl10* promoter reverse: 5’-AAGGAGCACAAGAGGGGAGA-3’; *Irf1* promoter forward: 5’-TTTCCAAGACAGGCAAGGGG-3’, *Irf1* promoter reverse: 5’-ACTCGGCCTCATCATTTCGG-3’; and IgH forward: 5’- GCCGATCAGAACCAGAACACCTGC-3’ , and IgH reverse: 5’-TGGTGGGGCTGGACAGAGTGTTTC-3’.

Microarray assay. Total RNA was extracted from B16F10 with Mi-2β knockout and the control cells treated with IFN-γ (10ng/mL) for 24 hours with the RNeasy Mini Kit (74104) (Qiagen, Hilden, Germany). The experimental group cells were cultured in triplicate. The experiment was comprised of 6 Mouse Gene 2.0 ST arrays. The arrays were normalized together using the Robust Multiarray Average algorithm and a CDF (Chip Definition File) that maps the probes on the array to unique Entrez Gene identifiers. The expression values are log2-transformed by default. The technical quality of the arrays was assessed by two quality metrics: Relative Log Expression (RLE) and Normalized Unscaled Standard Error (NUSE). For each sample, median RLE values >0.1 or NUSE values >1.05 are considered out of the usual limits. All arrays had median RLE and NUSE values well within these limits. Benjamini-Hochberg FDR correction was applied to obtain FDR-corrected *p* values (*q* values), which represent the probability that a given result is a false positive based on the distribution of all p values on the array. In addition, the FDR *q* value was also recomputed after removing genes that were not expressed above the array-wise median value of at least 3 arrays (i.e., the size of each experimental group). The GEO Series ID is GSE151640, with the link of https://www.ncbi.nlm.nih.gov/geo/query/acc.cgi?acc=GSE151640 and the token: exgreuqmhrcpdkf

ELISA assay. B16F10 cells ($1x10^6$) with or without Mi-2β knockdown were seeded in 6-well plates in complete growth medium. Cell medium was changed to serum-free medium, before treatment with IFN-γ at indicated concentration for 24 hours. The secreted chemokines were measured by mouse Cxcl9 ELISA kit (ab203364) and mouse Cxcl10 ELISA Kit (ab214563), according to the manufacturer's protocols. Isolated graft tumors were prepared and minced with blades, then tumor tissue were cultured in PBS (250 mg/500 µl) for 4 hours at 37 ºC. The secreted amount of the chemokines in the culture were measured by mouse Cxcl9 ELISA kit (ab203364) and mouse Cxcl10 ELISA Kit (ab214563), according to the manufacturer's protocols.

Validation of genes of the epigenetic factors. The gRNA sequences targeting the selected 18 epigenetic factors (3 gRNAs/gene) were cloned into a LentiCRISPRv2GFP vector (Addgene, #82416) following the CHOPCHOP (https://chopchop.rc.fas.harvard.edu/) [46]. Briefly, HEK293FT cells in 6-well plates were transfected with 1.5µg lentiviral plasmid, 1µg psPAX2, and 0.5µg pMD2.G with Lipofectamine™ 3000 Transfection Reagent (ThermoFisher, #L3000001). Lentivirus were collected after 2 days of transfections. After filtered through a 0.45µm filter, the lentivirus were stored at -80 °C. B61F10 cells were infected with lentivirus for 24 hours individually. Infected cells were sorted based on GFP expression by BD FACS Aria II. For *in vitro* co-culture assay, gRNA-targeted gene deficient B16F10 cells (GFP positive) were mixed with control B16F10 cells (GFP negative) at a 1:1 ratio. The cells were treated with 10ng/ml of IFN-γ for 24 hours, and then co-cultured with activated Pmel-1 T cells. After three days, the gene depleted

B16F10 cells was determined by FACS, comparing the percentage of knockdown cells (GFP positive) to control B16F10 cells (GFP negative).

Syngeneic melanoma graft mouse model. Mi-2β knockdown or Scramble B16F10 cells ($1.5X10^5$) were mixed with BD matrigel (Matrix Growth Factor Reduced) (BD, 354230) in 100 µl PBS, and then subcutaneously injected into the right flanks of C57BL/6 mice of 8-10 week old (from the Jackson Laboratory, 000664). Tumor growth was measured with calipers, and size was expressed as one-half of the product of perpendicular length and square width in cubic centimeters every 3 days. For antibody treatment, control IgG antibodies (10mg/kg) or anti-PD-1 (RMP1-14, BioXCell, 10mg/kg) was injected intraperitoneally (i.p.) on day 6, 9, 12, 15 and 18 after tumor cell inoculation. For tumor growth curve, grafts were measured with calipers and established ($0.5*\text{length} \times \text{width}^2$) every three days. For survival tests, mice were euthanized when the tumor size exceeded 1 cm^3. To test Z36-MP5 function in syngeneic mouse model, B16F10 cells ($1.5X10^5$) were mixed with BD matrigel (Matrix Growth Factor Reduced) (BD, 354230) in 100 µl PBS, and then mouse subcutaneous injection and tumor graft monitor were performed as described above. Except that vehicle [5% (w/v) Kolliphor HS 15 (Sigma)] in normal saline or formulated 30 mg/kg Z36-MP5 was administered with i.p. injection once a day starting at day 6, together with i.p. injection of control IgG antibodies (10mg/kg) or anti-PD-1 (RMP1-14, BioXCell, 10mg/kg) on day 6, 9, 12, 15 and 18. The mice were euthanized after indicated days or when the allowable endpoint size (1 cm^3) was reached. All mice were maintained in pathogen-free conditions in the animal facility at Boston University. All animal experiments were performed in accordance with the Guide for the Care and Use of Laboratory Animals of the National Institutes of Health, and the protocol was reviewed and approved by the Animal Science Center (ASC) of Boston University.

Genetically engineered mouse models. *Mi-2β*$^{lox/lox}$ mice were generated and generously provide by Dr. Georgopoulos lab (Massachusetts General Hospital at Harvard Medical School) [36]. Tyr::CreER;*BRaf*^{CA};*Pten*$^{lox/lox}$ mice were purchased from Jackson laboratories (Stock No: 013590). All strains of mice were on the background of C57BL/6J background. Gene activation and silencing were induced with intraperitoneal (i.p.) administration of 100 μL/mouse/day tamoxifen (20mg/mL) for constant 5 days. Mice with measureable tumors were randomly treated with either control IgG antibodies (10mg/kg) or anti-PD-1 (RMP1-14, BioXCell, 10mg/kg) by i.p. administration at day 9, 12, 15, 18 and 21 after Cre activation. To test Z36-MP5 function *in vivo*, vehicle [5% (w/v) Kolliphor HS 15 (Sigma)] in normal saline or formulated 30 mg/kg Z36-MP5 was administered with i.p. injection once a day starting at day 9 after Cre activation, together with i.p. injection of control IgG antibodies (10mg/kg) or anti-PD-1 (RMP1-14, BioXCell, 10mg/kg) starting on day 9, 12, 15, 18 and 21 after Cre activation, as indicated. Tumor growth was then monitored each the other day. All mice were bred and maintained in pathogen-free conditions in the animal facility at Boston University. All animal experiments were done according to protocols approved by the Boston University and in accordance with the guidelines set forth by the US National Institutes of Health.

Kaplan-Meier survival analysis. TCGA data set was downloaded from website (http://tcgabrowser.ethz.ch:3839/TEST/). The melanoma patients (n=454) were divided into CD8 High and CD8 Low groups based on the mRNA expression of CD8. The median gene expression of CD8 was set as the cutoff. For each Gene and CD8 High/Low group, we further divide the samples into High and Low subgroups based on the gene's median expression. The Kaplan-Meier survival curves were generated, and their differences were examined using a log-rank test.

Preparation of tumor-infiltrating T cells. Tumors were minced with scissors, and then digested with the digestion buffer (RPMI 1640 medium, 5% FBS, 1% penicillin-streptomycin, 25 mM HEPES, and 300 U collagenase (Sigma C0130)) on a shaker at 37 °C for 2 hours. Single cells were prepared through a 70 μm cell strainer. Erythrocytes were removed by incubation in red blood cell lysis buffer (R7757, Sigma) at room temperature for 5 min. The cells were prepared in PBS (with concentration of ~2×10^7) for studies.

Flow cytometry. The single-cell suspension were fixed with 2% paraformaldehyde solution (J19943K2, Thermo Scientific). And then the cells were stained with the follow antibodies: anti-mouse CD45 APC (104, BD pharmingen, 561875), anti-mouse CD3e PE (145-2C11, BD pharmingen, 553063), anti-mouse CD4 FITC (RM4-5, BD pharmingen, 553046), anti-mouse CD4 PE/Cy7 (GK1.5, BioLegend, 100421), anti-mouse CD8 FITC (53-6.7, BD pharmingen, 553031), anti-mouse CD8a APC/Cy7 (53-6.7, BioLegend 100713), anti-mouse IFN-γ PE (XMG1.2, eBioscience, 12731181), anti-mouse CD69 PE (H1.2F3, Biolegend, 104508), anti-mouse CD25 Alexa Fluor 488 (PC61.5, eBioscience, 53025182), anti-mouse CD107a-V450 (1D4B, BD, 560648), anti-human/mouse granzyme B FITC (GB11, BioLegend, 515403). The regulatory T cells in TILs were stained with the Mouse Regulatory T Cell Staining kit#1 (88-8111, ThermoFisher Scienctific), with antibodies of anti-mouse CD4 FITC (RM4-5), anti-mouse CD25 APC (PC61.5), and anti-mouse Foxp3 PE (FJK-16s). BD LSRII was used for data acquisition and FlowJo was used for data analysis.

Protein expression and purification. Flag-Mi-2β was expressed and purified from HEK293 cells, which were cultured in DMEM supplemented with 10% Fetal Bovine Serum 100 unites/ml penicillin and 100 μg/ml streptomycin. Flag-Mi-2β in pcDNA3.1 expression vector were transfected into HEK293 cells with Lipofectamine™ 3000 Transfection Reagent (ThermoFisher) for 3 days. The resulted cells were harvested for the nuclear pellet extraction with cytoplasmic lysis buffer (50 mM HEPES, 10 mM KCl, 1.5 mM MgCl2, 1mM DTT, 1mM PMSF and 1X protease inhibitor, pH7.5) on ice for 30 minutes. The nuclear pellet was collected by spun down. The nuclear lysis buffer (50 mM HEPES, 0.5 M NaCl, 1 mM EDTA, 1% Triton X-100, 1.5 mM MgCl2, 1 mM DTT, 1 mM PMSF, and 1Xprotease inhibitor, pH 8) was used to resuspend nuclear pellet for homogenization by sonication. Nuclear extract was incubated with Flag M2 affinity gel beads (Sigma-Aldrich) at 4 °C for overnight. The Flag M2 beads were washed, and Flag-Mi-2β protein was eluted with 300 µg/ml 3XFlag peptide (Sigma-Aldrich), in 20 mM HEPES, 150 mM NaCl, 1 mM DTT, and 10% glycerol, pH 7.5. Protein was confirmed by SDS-PAGE and coomassie stains. All the purified protein samples were concentrated, aliquoted and flash-frozen in liquid nitrogen, and then stored in -80°C for later use.

TCGA data analysis. To analysis the hazard ratio of epigenetic factor in human melanoma samples, we downloaded the ATGC data set of melanoma from http://tcgabrowser.ethz.ch:3839/TEST/ on 2018-09-03. Data of 454 melanoma patient samples were available for analysis. The patients were divided into CD8A high and CD8A low groups based on the gene expression of CD8A. The median CD8A expression was chosen as the cutoff.

ATP-driven nucleosome remodeling reactions. The function of chromatin remodeling enzyme was studied with EpiDyne-FRET (EpiCypher, SKU: 16-4201) according to the protocol. Briefly, Nucleosomes were assembled with the recombinant nucleosome substrates Cy5-labeled human histone octamer (H2A T120C-Cy5) wrapped with 5’ Cy3-labeled DNA (207bp), in which contains a terminally nucleosome positioning Widom 601 element. Cy3-Cy5 FRET is at a maximum level at the assembled starting state. When the histone octamer is relocated towards the DNA 3’ by chromatin remodeler enzymes, Cy3-labeled

DNA 5' end is moved away from the Cy5-labeled octamer, leading to a reduction in FRET signal. The optimal conditions of the Mi-2β enzyme and the ATP concentrations in the 96-well were determined using FRET signal which was read by QuantStudio 12K Flex Real-Time PCR System with capable of Cy3 (Excitation-531 nm/Emission-579 nm)/Cy5 (emission-685 nm) detection. Data is expressed as the ratio of the raw Cy3 and Cy5 emission signals at each time point. For the Mi-2β concentration and reaction time optimization, Flag-tagged Mi-2β at series of concentrations (ranging from 0.4 to 250nM), ATP at a non-limiting concentration (1mM) were added to 96-well white solid plates and incubated for different times (0 to 50 minutes) with the substrate EpiDyne-FRET nucleosome at a saturated concentration (20nM), in the 50 μL reaction buffer containing 50 mM Tris, pH 7.5, 50 mM KCl and 3 mM MgCl2. The nucleosome remodeling reaction was stopped by adding 10 mM EDTA and 0.25 mg/ml Salmon Sperm DNA. The assay had a sufficiently high assay signal, and a minimal substrate conversion for a sufficient assay window was taken. We finally chose 12.5 nM Mi-2β and a reaction time of 15 minutes as the optimal condition for the nucleosome remodeling assay. The ATP titration was performed with Mi-2β using the enzyme concentration and reaction time previously determined, with at ATP concentrations ranging from 0.1 to 300 μM. The Michaelis-Menten equation was performed to calculate the apparent ATP Km. At the ATP concentration of 11.54 μM, Mi-2β showed a 50% change between the maximum and minimum reaction signal levels.

Z-factor was used to determine the assay quality (Z-factors above 0.5 represent an assay with an excellent quality). In the optimization assay procedure, the wells without Mi-2β was defined as 100% inhibition controls, and that containing Mi-2β was regarded as the 0% inhibition controls. The FRET signaling in each well was detected and Cy3/Cy5 ratio was calculated. Then the average (represented as μ) and standard deviations (represented as σ) of the ratios were calculated too. The Z-factor equation is $\text{Z-factor} = 1 - 3 \times (\sigma_{0\%\text{Inhibition}} + \sigma_{100\%\text{Inhibition}}) / (\mu_{0\%\text{Inhibition}} - \mu_{100\%\text{Inhibition}})$. The Z-factor was 0.729 for Mi-2β, which confirmed the optimization of assay conditions including enzyme concentration, ATP concentration and the reaction time.

Homology modeling and screening

Homology Modeling was carried out using Structure Prediction Wizard in Prime. The Homology Model of Mi-2β (CHD4) was generated using the yeast CHD1 structure (PDB code:3MWY) as template and the receptor sequence was obtained from Uniprot. Standard options were used when running the program and one homology model was gotten. For the output structure, the receptor was properly prepared using Protein Preparation Guide. Virtual screening was done in the default workflow process. First, enzyme hinge region ligands database and nucleoside mimetics database from Enamine are was prepared using a LigPrep and 3 low energy conformations are generated for each ligand. Then all ligands are docked to the ATP binding site for Mi-2β using SP docking and postprocessed with Prime MM-GBSA. After minimization, we kept top 1000 ligands from MM-GBSA score for each database. We have identified ligands with methyldihydroimidazopyridinone structure can interact well with the ATP warhead binding region of Mi-2β.

Profile of Z36-MP5 inhibition on ATPases. The Profile of Z36-MP5 inhibition on ATPases was measured by ActivX Biosciences inc. (La Jolla, CA). In briefly, Z36-MP5 was directly added to A375 cell lysates generated with a tip sonicator, and the resulting lysate was clarified by centrifugation at 16100g for 15 minutes to get the native cell lysate. For the ATP acyl phosphate probe-based chemoproteomics, lysine residues in ATP-binding sites were acylated with a desthiobiotin tag, and labeled peptides were isolated by affinity capture. The probe labeling reaction could be blocked by ATPase inhibitors. Labeled peptides were identified on the basis of their MS spectra generated by data-dependent LC-MS/MS.

Duplicated treated samples and control samples were performed and the inhibition results were analyzed as % changes with statistically significance (Student *t*-test score $p<0.05$).

Pharmacokinetics of Z36-MP5 in rats. Compound Z36-MP5 was evaluated in a pharmacokinetic study in male Sprague-Dawley (SD) rats following intraperitoneal injection of Z36-MP5 at 1.0 mg/kg as a solution in 5% DMSO, 30% PEG400, and 65% corn oil. Blood was collected at 0.25 h, 0.5 h, 1 h, 2 h, 4 h, 8 h, and 24 h following intraperitoneal injection. The blood samples were placed in wet ice, and serum was collected after centrifugation. Serum samples were frozen and stored at -80 °C. The serum samples were analyzed utilizing HPLC-coupled tandem mass spectrometry (LC-MS/MS). Values are calculated from arithmetic mean plasma concentrations (n = 3 rats per condition).

Chemical synthesis Z36-MP5

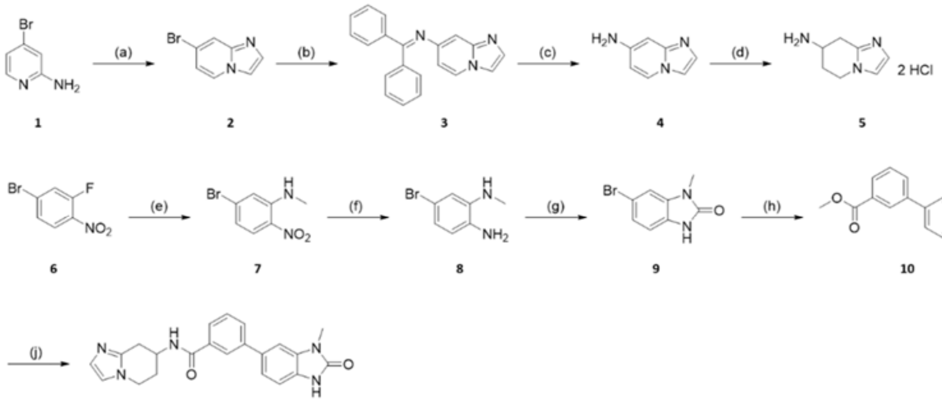

Flash chromatography was performed using silica gel (200−300 mesh). All reactions were monitored by thin-layer chromatography (TLC) on silica gel plates. ^{1}H-NMR spectral data were recorded on Varian Mercury 400 NMR spectrometer, and ^{13}C-NMR was recorded on Varian Mercury 126 NMR spectrometer at ambient temperature. Chemicals shifts (*δ*) were reported in ppm, coupling constants (J) were in hertz, and the splitting patterns were described as follows: s for singlet; d for doublet; t for triplet; q for quartet;

and m for multiplet. Mass spectrometry was conducted using a Thermo Fisher LCQ-DECA spectrometer (ESI-MS mode). All tested compounds were purified to ≥95% purity as determined by high performance liquid chromatography (HPLC).

Reagents and conditions: (a) 50% chloroacetaldehyde in H_2O, EtOH, 80 °C, 2 h; (b) benzophenone imine, $Pd_2(dba)_3$, BINAP, *t*-BuONa, toluene, 85 °C, overnight; (c) 4 M HCl in 1,4-dioxane, room temperature, 24 h; (d) 4 M HCl in 1,4-dioxane, Pd/C, MeOH, 50 °C, 24 h; (e) 2 M methylamine solution in MeOH, EtOH, room temperature, overnight; (f) zinc powder, NH_4Cl, H_2O, MeOH, room temperature, 1 h; (g) carbonyldiimidazole, ACN, reflux, overnight; (h) 3-methoxycarbonylphenylboronic acid, 2.5 M Na_2CO_3, $Pd(PPh_3)_2Cl_2$, LiCl, EtOH, toluene, sealed tube, 95 °C, overnight; (i) $LiOH{\cdot}H_2O$, THF, MeOH, H_2O, rt, overnight; (j) **5**, HATU, DIPEA, DMF, rt, overnight.

Step a: synthesis of 7-bromoimidazo[1,2-a]pyridine, ***2***

A mixture of 4-bromopyridin-2-amine (**1**, 10.4 g, 60.0 mmol) and 50% chloroacetaldehyde in H_2O (18.8 g, 120.0 mmol) in EtOH (150.0 mL) was stirred at 75 °C for 2 hours. After the complete conversion detected by TCL analysis (DCM : MeOH = 10 : 1), the reaction mixture was concentrated under vacuum to afford a yellow thick oil. EA (50.0 mL) was added to the thick oil and the resulting suspension was stirred at room temperature for 30 minutes to generate a yellow suspension. Then the suspension was filtered to afford a light yellow solid which was washed with EA (20.0 mL) and hexanes (20.0 mL) to afford an off-white solid as 7-bromoimidazo[1,2-*a*]pyridine (**2**, 11.1 g, 93.7% yields). LC-MS: 197.12 $[M]^+$.

Step b: synthesis of N-(imidazo[1,2-a]pyridin-7-yl)-1,1-diphenylmethanimine, ***3***

A mixture of 7-bromoimidazo[1,2-*a*]pyridine (**2**, 0.4 g, 2.0 mmol), benzophenone imine (0.7 g, 4.0 mmol), *t*-BuONa (0.4 g, 4.0 mmol), $Pd_2(dba)_3$ (92.0 mg, 0.1 mmol), and BINAP (93.0 mg, 0.15 mmol) in toluene (10.0 mL) was degassed with N_2 for 15 minutes. Then the reaction mixture was allowed to stir at 85 °C overnight. After cooling to room temperature, the resulting mixture was diluted with water (50.0 mL) and extracted with EA (50.0 mL * 3). The combined organic layers were washed with brine (50.0 mL), dried over anhydrous Na_2SO_4, filtered, concentrated under vacuum, absorbed onto silica gel, and purified via flash chromatography (DCM : MeOH = 30 : 1) to afford a yellow oil as *N*-(imidazo[1,2-*a*]pyridin-7-yl)-1,1-diphenylmethanimine (**3**, 0.4 g, 69% yields). LC-MS: 297.40 $[M]^+$.

*Step c: synthesis of imidazo[1,2-a]pyridin-7-amine, **4***

A solution of *N*-(imidazo[1,2-*a*]pyridin-7-yl)-1,1-diphenylmethanimine (**3**, 0.4 g, 1.4 mmol) in 4 M hydrogen chloride solution in 1,4-dioxane was stirred at room temperature for 24 hours to afford a dark brown suspension. After the complete conversion detected by LC-MS analysis, the resulting mixture was filtered to obtain a brown solid which was washed with DCM (5.0 mL) to afford a dark yellow solid. The dark yellow solid was dissolved in MeOH (10.0 mL), aborbed onto celite, and purified via C18 reversed-phase flash column chromatography (H_2O : MeOH = 9 : 1) to afford a brown solid as imidazo[1,2-a]pyridin-7-amine (**4**, 0.15 g, 56% yields). LC-MS: 133.41 $[M]^+$.

*Step d: synthesis of 5,6,7,8-tetrahydroimidazo[1,2-a]pyridin-7-amine dihydrochloride, **5***

A mixture of imidazo[1,2-a]pyridin-7-amine (**4**, 0.1 g, 0.78 mmol), Pd/C (20.0 mg, 20%wt), and 4 M hydrogen chloride solution in 1,4-dioxane (0.2 mL) in MeOH (5.0 mL) was stirred at 50 ºC for 24 hours. After the complete conversion detected by TLC (DCM: MeOH = 10 : 1) and LC-MS analysis, the resulting mixture was concentrated under vacuum to afford a yellow solid. DCM (5.0 mL) was added to the yellow solid and the resulting suspension was stirred at room temperature for 15 minutes to generate a light yellow suspension. Then the suspension was filtered to afford a light yellow solid which was washed with a combined solution of DCM and MeOH (DCM: MeOH = 10:1, 5 mL) to afford an beige solid as 5,6,7,8-tetrahydroimidazo[1,2-a]pyridin-7-amine dihydrochloride (**5**, 0.1 g, 61% yields). LC-MS: 137.10 $[M]^+$.

*Step e: synthesis of 5-bromo-N-methyl-2-nitroaniline, **7***

To a solution of 4-bromo-2-fluoro-1-nitrobenzene (**6**, 4.4 g, 20.0 mmol) in EtOH (50.0 mL) was added 2 M methylamine solution in MeOH (12.0 mL, 240.0 mmol). The reaction mixture was stirred at room temperature overnight. After the complete conversion detected LC-MS analysis, the resulting mixture was concentrated under vacuum, and the residual orange solid was partitioned between water (200.0 mL) and EA (200.0 mL * 3). The combined organic phases were washed with brine, dried over anhydrous Na_2SO_4, filtered, concentrated under vacuum to afford a bright orange solid as 5-bromo-*N*-methyl-2-nitroaniline (**7**, 4.4 g, 97% yields). LC-MS: 232.30 $[M + H]^+$.

*Step f: synthesis of 5-bromo-N^1-methylbenzene-1,2-diamine, **8***

To a suspension of 5-bromo-*N*-methyl-2-nitroaniline (**7**, 3.0 g, 13.0 mmol) and ammonium chloride (7.0 g, 130.0 mmol) in MeOH (17.0 mL) and water (35.0 mL) was added zinc powder (4.2 g, 65.0 mmol) at 0 °C. The reaction mixture was allowed to stir at room temperature for 1 hour. After the complete conversion detected LC-MS analysis, the resulting mixture was filtered and the filtered liquid was concentrated under vacuum to remove the MeOH. Then the residual solution was neutrilized by the addtion of saturated $NaHCO_3$ aqueous solution to PH 7~8 and extracted with EA (100.0 mL * 3). The combined orgainc phases were washed with brine, dried over anhydrous Na_2SO_4, filtered, concentrated under vacuum, absorbed onto aluminum oxide, and purified via flash column chromatography (EA : hexanes = 1 : 99 to 1 : 1) to afford a black solid as 5-bromo-N^1-methylbenzene-1,2-diamine (**8**, 1.8 g, 71% yields). LC-MS: 201.01 $[M]^+$.

*Step g: synthesis of 6-bromo-1-methyl-1,3-dihydro-2H-benzo[d]imidazol-2-one, **9***

To a solution of 5-bromo-N^1-methylbenzene-1,2-diamine (**8**, 1.0 g, 5.0 mmol) in acetonitrile (20.0 mL) was added carbonyldiimidazole (4.0 g, 24.9 mmol). The reaction mixture was refluxed at 85 °C overnight. After cooling, the resulting mixture was concentrated under vacuum to afford a dark brown residue. The residue was partitioned between water (50.0 mL) and EA (50.0 mL * 3). The combined organic layers were washed with brine, dried over anhydrous Na_2SO_4, filtered, concentrated under vacuum, absorbed onto silica gel, and purified via flash column chromatography (DCM : MeOH = 99 : 1 to 95 : 5) to afford a brown-orange solid as 6-bromo-1-methyl-1,3-dihydro-2*H*-benzo[*d*]imidazol-2-one (**9**, 0.5 g, 41% yields). LC-MS: 227.01 $[M]^+$.

*Step h: synthesis of methyl 3-(3-methyl-2-oxo-2,3-dihydro-1H-benzo[d]imidazol-5-yl)benzoate, **10***

A mixture of 6-bromo-1-methyl-1,3-dihydro-2*H*-benzo[*d*]imidazol-2-one (**9**, 70.0 mg, 0.3 mmol), 3-methoxycarbonylphenylboronic acid (80.1 mg, 0.45 mmol), LiCl (38.2 mg, 0.9 mmol), freshly prepared 2.5 M Na_2CO_3 aqueous solution (0.30 mL, 0.75 mmol), and bis(triphenylphosphine)palladium(II) dichloride (10.6 mg, 0.16 mmol) in toluene (4.0 mL) and EtOH (4.0 mL) was degassed with N_2 for 15 minutes. The reaction mixture was sealed in a 20.0 mL vial and stirred at 95 ^oC overnight. After the complete conversion detected LC-MS analysis, the resulting mixture was concentrated under vacuum, absorbed onto silica gel, and purified via flash column chromatography (DCM : MeOH = 99 : 1 to 10 : 1) to afford a white solid as methyl 3-(3-methyl-2-oxo-2,3-dihydro-1*H*-benzo[*d*]imidazol-5-yl)benzoate (**10**, 40.0 mg, 47% yields). LC-MS: 283.15 $[M]^+$.

*Step i: synthesis of 3-(3-methyl-2-oxo-2,3-dihydro-1H-benzo[d]imidazol-5-yl)benzoic acid, **11***

To a solution of methyl 3-(3-methyl-2-oxo-2,3-dihydro-1*H*-benzo[*d*]imidazol-5-yl)benzoate (**10**, 40.0 mg, 0.14 mmol) in MeOH (2.1 mL) and tetrahydrofuran (2.1 mL) was added a solution of $LiOH \cdot H_2O$ (8.9 mg, 0.21 mol) in water (0.7 mL). The reaction mixture was stirred at room temperature overnight. After the complete conversion detected LC-MS analysis, the resulting mixture was concentrated under vacuum to remove the organic solverts and diluted with water (2.0 mL). The aqueous solution was acidified via the addition of 2 M HCl solution in water to PH 4 to obtain a white suspension. After filtration, the off-white solid collected was washed with Et_2O (0.5 mL) to afford a white solid as 3-(3-methyl-2-oxo-2,3-dihydro-1*H*-benzo[*d*]imidazol-5-yl)benzoic acid (**11**, 30.0 mg, 80% yields). LC-MS: 269.39 $[M]^+$.

*Step j: synthesis of 3-(3-methyl-2-oxo-2,3-dihydro-1H-benzo[d]imidazol-5-yl)-N-(5,6,7,8-tetrahydroimidazo[1,2-a]pyridin-7-yl)benzamide, (**Z36-MP5**)*

A mixture of 3-(3-methyl-2-oxo-2,3-dihydro-1*H*-benzo[*d*]imidazol-5-yl)benzoic acid (**11**, 30.0 mg, 0.11 mmol), 5,6,7,8-tetrahydroimidazo[1,2-a]pyridin-7-amine dihydrochloride (**5**, 19.4 mg, 0.11 mmol), and *N*,*N*-diisopropylethylamine (0.12 mL, 0.66 mmol) in anhydrous DMF was stirred at 0 ºC for 5 minutes. The HATU (50.2 mg, 0.13 mmol) was added in one portion. The reaction mixture was stirred at room temperature overnight. After the complete conversion detected LC-MS analysis, the resulting mixture was diluted with water (20.0 mL) and extracted with EA (20.0 mL * 3). The combined orgainc layers were washed with brine, dried over anhydrous Na_2SO_4, filtered, concentrated under vacuum, absorbed onto silica gel, and purified via flash column chromatography (DCM : MeOH = 99 : 1 to 10 : 1) to afford a white solid as 3-(3-methyl-2-oxo-2,3-dihydro-1*H*-benzo[*d*]imidazol-5-yl)-*N*-(5,6,7,8-tetrahydroimidazo[1,2-*a*]pyridin-7-yl)benzamide (**12**, 10.2 mg, 23.9% yields). LC-MS: 388.09 $[M+H]^+$.

Quantification statistical analysis

Animals were grouped randomized. The qualification experiments were blinded by investigators. All samples or animals were included in analysis. All quantitative data were presented as the mean ± SD or SEM of at least three independent experiments. The unpaired, two tailed t-test Comparisons were performed between two groups. Statistical tests were done with biological replicates. The Kaplan-Meier survival curves for survival curve were compared using the log–rank test. $p < 0.05$ was considered statistically significant. *$p < 0.05$, ** $p < 0.01$, *** $p < 0.001$, n.s., not significant.

Acknowledgments

We thank Dr. Katia Georgopoulos lab (Massachusetts General Hospital, Harvard Medical School) and Dr. John Svaren (University of Wisconsin-Madison) for generously providing Mi-2βlox/lox mice. We thank Dr. Joel Mackay (The University of Sydney, Austria) and Dr. Luisa Lanfrancone (European Institute of Oncology) for kindly sharing their plasmids.

Author contributions

R.C. conceived the hypothesis, organized and supervised the study with X.M., P.C., H.L., and X.L. R.C. designed the project with help from X.M., H.L., X.L., B.Z., Z.W. and C.R.G. B.Z., Z.W., X.L., L.Y., J.Z., X.L., and J.H. performed the experiments and contributed to data analysis. R.C. wrote the manuscript with help from C.R.G., J.S., P.T, M.C., and J.Z. for manuscript edition, revision and interpretation. All authors commented on the manuscript. Competing interests: The authors declare no competing interests; Data and materials availability: All data are available in the manuscript or supplementary materials.

Competing financial interests

The authors declare no competing interests.

References

1. Schadendorf, D. & Hauschild, A. Melanoma in 2013: Melanoma--the run of success continues. *Nat Rev Clin Oncol* **11**, 75-76 (2014).

2. Franklin, C., Livingstone, E., Roesch, A., Schilling, B. & Schadendorf, D. Immunotherapy in melanoma: Recent advances and future directions. *Eur J Surg Oncol* **43**, 604-611 (2017).

3. Schadendorf, D. *et al.* Pooled Analysis of Long-Term Survival Data From Phase II and Phase III Trials of Ipilimumab in Unresectable or Metastatic Melanoma. *J Clin Oncol* **33**, 1889-1894 (2015).

4. Ribas, A. *et al.* Association of Pembrolizumab With Tumor Response and Survival Among Patients With Advanced Melanoma. *JAMA* **315**, 1600-1609 (2016).

5. Larkin, J. *et al.* Combined Nivolumab and Ipilimumab or Monotherapy in Untreated Melanoma. *N Engl J Med* **373**, 23-34 (2015).

6. Postow, M.A. *et al.* Nivolumab and ipilimumab versus ipilimumab in untreated melanoma. *N Engl J Med* **372**, 2006-2017 (2015).

7. Ribas, A. & Wolchok, J.D. Cancer immunotherapy using checkpoint blockade. *Science* **359**, 1350-1355 (2018).

8. Hugo, W. *et al.* Genomic and Transcriptomic Features of Response to Anti-PD-1 Therapy in Metastatic Melanoma. *Cell* **165**, 35-44 (2016).

9. Chan, T.A., Wolchok, J.D. & Snyder, A. Genetic Basis for Clinical Response to CTLA-4 Blockade in Melanoma. *N Engl J Med* **373**, 1984 (2015).

10. Gubin, M.M. *et al.* Checkpoint blockade cancer immunotherapy targets tumour-specific mutant antigens. *Nature* **515**, 577-581 (2014).

11. Marincola, F.M., Jaffee, E.M., Hicklin, D.J. & Ferrone, S. Escape of human solid tumors from T-cell recognition: molecular mechanisms and functional significance. *Adv Immunol* **74**, 181-273 (2000).

12. Bronte, V. *et al.* Boosting antitumor responses of T lymphocytes infiltrating human prostate cancers. *J Exp Med* **201**, 1257-1268 (2005).

13. O'Donnell, J.S., Long, G.V., Scolyer, R.A., Teng, M.W. & Smyth, M.J. Resistance to PD1/PDL1 checkpoint inhibition. *Cancer Treat Rev* **52**, 71-81 (2017).

14. Sharma, P., Hu-Lieskovan, S., Wargo, J.A. & Ribas, A. Primary, Adaptive, and Acquired Resistance to Cancer Immunotherapy. *Cell* **168**, 707-723 (2017).

15. Ghorani, E. & Quezada, S.A. Chromatin regulation and immune escape. *Science* **359**, 745-746 (2018).

16. Benci, J.L. *et al.* Tumor Interferon Signaling Regulates a Multigenic Resistance Program to Immune Checkpoint Blockade. *Cell* **167**, 1540-1554 e1512 (2016).

17. Gao, J. *et al.* Loss of IFN-gamma Pathway Genes in Tumor Cells as a Mechanism of Resistance to Anti-CTLA-4 Therapy. *Cell* **167**, 397-404 e399 (2016).

18. Abril-Rodriguez, G. *et al.* PAK4 inhibition improves PD-1 blockade immunotherapy. *Nature Cancer* **1**, 46-58 (2020).

19. Skoulidis, F. *et al.* STK11/LKB1 Mutations and PD-1 Inhibitor Resistance in KRAS-Mutant Lung Adenocarcinoma. *Cancer Discov* **8**, 822-835 (2018).

20. Peng, W. *et al.* Loss of PTEN Promotes Resistance to T Cell-Mediated Immunotherapy. *Cancer Discov* **6**, 202-216 (2016).

21. Miao, D. *et al.* Genomic correlates of response to immune checkpoint therapies in clear cell renal cell carcinoma. *Science* **359**, 801-806 (2018).

22. Pan, D. *et al.* A major chromatin regulator determines resistance of tumor cells to T cell-mediated killing. *Science* **359**, 770-775 (2018).

23. Ni, Z. *et al.* Apical role for BRG1 in cytokine-induced promoter assembly. *Proc Natl Acad Sci U S A* **102**, 14611-14616 (2005).

24. Blackledge, N.P., Rose, N.R. & Klose, R.J. Targeting Polycomb systems to regulate gene expression: modifications to a complex story. *Nat Rev Mol Cell Biol* **16**, 643-649 (2015).

25. Abou El Hassan, M. *et al.* Cancer Cells Hijack PRC2 to Modify Multiple Cytokine Pathways. *PLoS One* **10**, e0126466 (2015).

26. Zingg, D. *et al.* The Histone Methyltransferase Ezh2 Controls Mechanisms of Adaptive Resistance to Tumor Immunotherapy. *Cell Rep* **20**, 854-867 (2017).

27. Li, J. *et al.* Epigenetic driver mutations in ARID1A shape cancer immune phenotype and immunotherapy. *J Clin Invest* (2020).

28. Seelig, H.P. *et al.* The major dermatomyositis-specific Mi-2 autoantigen is a presumed helicase involved in transcriptional activation. *Arthritis Rheum* **38**, 1389-1399 (1995).

29. Kim, J. *et al.* Ikaros DNA-binding proteins direct formation of chromatin remodeling complexes in lymphocytes. *Immunity* **10**, 345-355 (1999).

30. Lai, A.Y. & Wade, P.A. Cancer biology and NuRD: a multifaceted chromatin remodelling complex. *Nat Rev Cancer* **11**, 588-596 (2011).

31. Mueller-Planitz, F., Klinker, H. & Becker, P.B. Nucleosome sliding mechanisms: new twists in a looped history. *Nat Struct Mol Biol* **20**, 1026-1032 (2013).

32. Gomez-Del Arco, P. *et al.* The Chromatin Remodeling Complex Chd4/NuRD Controls Striated Muscle Identity and Metabolic Homeostasis. *Cell Metab* **23**, 881-892 (2016).

33. Gao, H. *et al.* Opposing effects of SWI/SNF and Mi-2/NuRD chromatin remodeling complexes on epigenetic reprogramming by EBF and Pax5. *Proc Natl Acad Sci U S A* **106**, 11258-11263 (2009).

34. Williams, C.J. *et al.* The chromatin remodeler Mi-2beta is required for CD4 expression and T cell development. *Immunity* **20**, 719-733 (2004).

35. Naito, T., Gomez-Del Arco, P., Williams, C.J. & Georgopoulos, K. Antagonistic interactions between Ikaros and the chromatin remodeler Mi-2beta determine silencer activity and Cd4 gene expression. *Immunity* **27**, 723-734 (2007).

36. Kashiwagi, M. *et al.* Direct control of regulatory T cells by keratinocytes. *Nat Immunol* **18**, 334-343 (2017).

37. Pencil, S.D., Toh, Y. & Nicolson, G.L. Candidate metastasis-associated genes of the rat 13762NF mammary adenocarcinoma. *Breast Cancer Res Treat* **25**, 165-174 (1993).

38. Xia, L. *et al.* CHD4 Has Oncogenic Functions in Initiating and Maintaining Epigenetic Suppression of Multiple Tumor Suppressor Genes. *Cancer Cell* **31**, 653-668 e657 (2017).

39. Spranger, S. *et al.* Density of immunogenic antigens does not explain the presence or absence of the T-cell-inflamed tumor microenvironment in melanoma. *Proc Natl Acad Sci U S A* **113**, E7759-E7768 (2016).

40. Galon, J. & Bruni, D. Approaches to treat immune hot, altered and cold tumours with combination immunotherapies. *Nat Rev Drug Discov* **18**, 197-218 (2019).

41. Overwijk, W.W. *et al.* Tumor regression and autoimmunity after reversal of a functionally tolerant state of self-reactive CD8+ T cells. *J Exp Med* **198**, 569-580 (2003).

42. van Elsas, A., Hurwitz, A.A. & Allison, J.P. Combination immunotherapy of B16 melanoma using anti-cytotoxic T lymphocyte-associated antigen 4 (CTLA-4) and granulocyte/macrophage colony-stimulating factor (GM-CSF)-producing vaccines induces rejection of subcutaneous and metastatic tumors accompanied by autoimmune depigmentation. *J Exp Med* **190**, 355-366 (1999).

43. Chen, S. *et al.* Combination of 4-1BB agonist and PD-1 antagonist promotes antitumor effector/memory CD8 T cells in a poorly immunogenic tumor model. *Cancer Immunol Res* **3**, 149-160 (2015).

44. Golstein, P. & Griffiths, G.M. An early history of T cell-mediated cytotoxicity. *Nat Rev Immunol* **18**, 527-535 (2018).

45. Dankort, D. *et al.* Braf(V600E) cooperates with Pten loss to induce metastatic melanoma. *Nat Genet* **41**, 544-552 (2009).

46. Zhu, B. *et al.* The protective role of DOT1L in UV-induced melanomagenesis. *Nat Commun* **9**, 259 (2018).

47. Zaretsky, J.M. *et al.* Mutations Associated with Acquired Resistance to PD-1 Blockade in Melanoma. *N Engl J Med* **375**, 819-829 (2016).

48. Groom, J.R. & Luster, A.D. CXCR3 ligands: redundant, collaborative and antagonistic functions. *Immunol Cell Biol* **89**, 207-215 (2011).

49. Tokunaga, R. *et al.* CXCL9, CXCL10, CXCL11/CXCR3 axis for immune activation - A target for novel cancer therapy. *Cancer Treat Rev* **63**, 40-47 (2018).

50. Li, B. *et al.* Comprehensive analyses of tumor immunity: implications for cancer immunotherapy. *Genome Biol* **17**, 174 (2016).

51. Bornelov, S. *et al.* The Nucleosome Remodeling and Deacetylation Complex Modulates Chromatin Structure at Sites of Active Transcription to Fine-Tune Gene Expression. *Mol Cell* **71**, 56-72 e54 (2018).

52. Jacobson, M.P. *et al.* A hierarchical approach to all-atom protein loop prediction. *Proteins* **55**, 351-367 (2004).

53. Jacobson, M.P., Friesner, R.A., Xiang, Z. & Honig, B. On the role of the crystal environment in determining protein side-chain conformations. *J Mol Biol* **320**, 597-608 (2002).

54. Woodage, T., Basrai, M.A., Baxevanis, A.D., Hieter, P. & Collins, F.S. Characterization of the CHD family of proteins. *Proc Natl Acad Sci U S A* **94**, 11472-11477 (1997).

55. Ramirez, J., Dege, C., Kutateladze, T.G. & Hagman, J. MBD2 and multiple domains of CHD4 are required for transcriptional repression by Mi-2/NuRD complexes. *Mol Cell Biol* **32**, 5078-5088 (2012).

56. UniProt, C. UniProt: a worldwide hub of protein knowledge. *Nucleic Acids Res* **47**, D506-D515 (2019).

57. Yang, J.G., Madrid, T.S., Sevastopoulos, E. & Narlikar, G.J. The chromatin-remodeling enzyme ACF is an ATP-dependent DNA length sensor that regulates nucleosome spacing. *Nat Struct Mol Biol* **13**, 1078-1083 (2006).

58. Low, J.K. *et al.* CHD4 Is a Peripheral Component of the Nucleosome Remodeling and Deacetylase Complex. *J Biol Chem* **291**, 15853-15866 (2016).

59. Lowary, P.T. & Widom, J. New DNA sequence rules for high affinity binding to histone octamer and sequence-directed nucleosome positioning. *J Mol Biol* **276**, 19-42 (1998).

60. Nordin, B.E. *et al.* ATP Acyl Phosphate Reactivity Reveals Native Conformations of Hsp90 Paralogs and Inhibitor Target Engagement. *Biochemistry* **54**, 3024-3036 (2015).

61. McGranahan, N. *et al.* Clonal neoantigens elicit T cell immunoreactivity and sensitivity to immune checkpoint blockade. *Science* **351**, 1463-1469 (2016).

62. Luksza, M. *et al.* A neoantigen fitness model predicts tumour response to checkpoint blockade immunotherapy. *Nature* **551**, 517-520 (2017).

63. Schumacher, T.N. & Schreiber, R.D. Neoantigens in cancer immunotherapy. *Science* **348**, 69-74 (2015).

64. Spranger, S., Bao, R. & Gajewski, T.F. Melanoma-intrinsic beta-catenin signalling prevents anti-tumour immunity. *Nature* **523**, 231-235 (2015).

65. Hodis, E. *et al.* A landscape of driver mutations in melanoma. *Cell* **150**, 251-263 (2012).

66. O'Donnell, J.S., Teng, M.W.L. & Smyth, M.J. Cancer immunoediting and resistance to T cell-based immunotherapy. *Nat Rev Clin Oncol* **16**, 151-167 (2019).

67. Pitt, J.M. *et al.* Targeting the tumor microenvironment: removing obstruction to anticancer immune responses and immunotherapy. *Ann Oncol* **27**, 1482-1492 (2016).

68. Dangaj, D. *et al.* Cooperation between Constitutive and Inducible Chemokines Enables T Cell Engraftment and Immune Attack in Solid Tumors. *Cancer Cell* **35**, 885-900 e810 (2019).

69. Abele, R. & Tampe, R. Modulation of the antigen transport machinery TAP by friends and enemies. *FEBS Lett* **580**, 1156-1163 (2006).

70. Einstein, M.H. *et al.* Genetic variants in TAP are associated with high-grade cervical neoplasia. *Clin Cancer Res* **15**, 1019-1023 (2009).

71. Garrido, F., Aptsiauri, N., Doorduijn, E.M., Garcia Lora, A.M. & van Hall, T. The urgent need to recover MHC class I in cancers for effective immunotherapy. *Curr Opin Immunol* **39**, 44-51 (2016).

72. Basha, G. *et al.* A CD74-dependent MHC class I endolysosomal cross-presentation pathway. *Nat Immunol* **13**, 237-245 (2012).

73. Shin, D.S. *et al.* Primary Resistance to PD-1 Blockade Mediated by JAK1/2 Mutations. *Cancer Discov* **7**, 188-201 (2017).

74. Vredevoogd, D.W. *et al.* Augmenting Immunotherapy Impact by Lowering Tumor TNF Cytotoxicity Threshold. *Cell* **178**, 585-599 e515 (2019).

75. Manguso, R.T. *et al.* In vivo CRISPR screening identifies Ptpn2 as a cancer immunotherapy target. *Nature* **547**, 413-418 (2017).

76. Yatim, N. *et al.* RIPK1 and NF-kappaB signaling in dying cells determines cross-priming of CD8(+) T cells. *Science* **350**, 328-334 (2015).

77. Chen, G. *et al.* Exosomal PD-L1 contributes to immunosuppression and is associated with anti-PD-1 response. *Nature* **560**, 382-386 (2018).

78. Sosman, J.A. *et al.* Survival in BRAF V600-mutant advanced melanoma treated with vemurafenib. *N Engl J Med* **366**, 707-714 (2012).

79. Flaherty, K.T. *et al.* Combined BRAF and MEK inhibition in melanoma with BRAF V600 mutations. *N Engl J Med* **367**, 1694-1703 (2012).

80. Long, G.V. *et al.* Dabrafenib and trametinib versus dabrafenib and placebo for Val600 BRAF-mutant melanoma: a multicentre, double-blind, phase 3 randomised controlled trial. *Lancet* **386**, 444-451 (2015).

81. Hu-Lieskovan, S. *et al.* Improved antitumor activity of immunotherapy with BRAF and MEK inhibitors in BRAF(V600E) melanoma. *Sci Transl Med* **7**, 279ra241 (2015).

82. Koya, R.C. *et al.* BRAF inhibitor vemurafenib improves the antitumor activity of adoptive cell immunotherapy. *Cancer Res* **72**, 3928-3937 (2012).

83. Frederick, D.T. *et al.* BRAF inhibition is associated with enhanced melanoma antigen expression and a more favorable tumor microenvironment in patients with metastatic melanoma. *Clin Cancer Res* **19**, 1225-1231 (2013).

84. Liu, L. *et al.* The BRAF and MEK Inhibitors Dabrafenib and Trametinib: Effects on Immune Function and in Combination with Immunomodulatory Antibodies Targeting PD-1, PD-L1, and CTLA-4. *Clin Cancer Res* **21**, 1639-1651 (2015).

85. Heidorn, S.J. *et al.* Kinase-dead BRAF and oncogenic RAS cooperate to drive tumor progression through CRAF. *Cell* **140**, 209-221 (2010).

86. Poulikakos, P.I., Zhang, C., Bollag, G., Shokat, K.M. & Rosen, N. RAF inhibitors transactivate RAF dimers and ERK signalling in cells with wild-type BRAF. *Nature* **464**, 427-430 (2010).

87. Steinberg, S.M. *et al.* BRAF inhibition alleviates immune suppression in murine autochthonous melanoma. *Cancer Immunol Res* **2**, 1044-1050 (2014).

88. Knight, D.A. *et al.* Host immunity contributes to the anti-melanoma activity of BRAF inhibitors. *J Clin Invest* **123**, 1371-1381 (2013).

89. Yu, C. *et al.* Combination of Immunotherapy With Targeted Therapy: Theory and Practice in Metastatic Melanoma. *Front Immunol* **10**, 990 (2019).

90. Ribas, A., Hodi, F.S., Callahan, M., Konto, C. & Wolchok, J. Hepatotoxicity with combination of vemurafenib and ipilimumab. *N Engl J Med* **368**, 1365-1366 (2013).

91. Amin, A. *et al.* Phase II study of vemurafenib followed by ipilimumab in patients with previously untreated BRAF-mutated metastatic melanoma. *J Immunother Cancer* **4**, 44 (2016).

92. Minor, D.R., Puzanov, I., Callahan, M.K., Hug, B.A. & Hoos, A. Severe gastrointestinal toxicity with administration of trametinib in combination with dabrafenib and ipilimumab. *Pigment Cell Melanoma Res* **28**, 611-612 (2015).

93. Smith, M.P. *et al.* The immune microenvironment confers resistance to MAPK pathway inhibitors through macrophage-derived TNFalpha. *Cancer Discov* **4**, 1214-1229 (2014).

94. Zhu, B., Zhang, M., Byrum, S.D., Tackett, A.J. & Davie, J.K. TBX2 blocks myogenesis and promotes proliferation in rhabdomyosarcoma cells. *Int J Cancer* **135**, 785-797 (2014).

Fig. 1

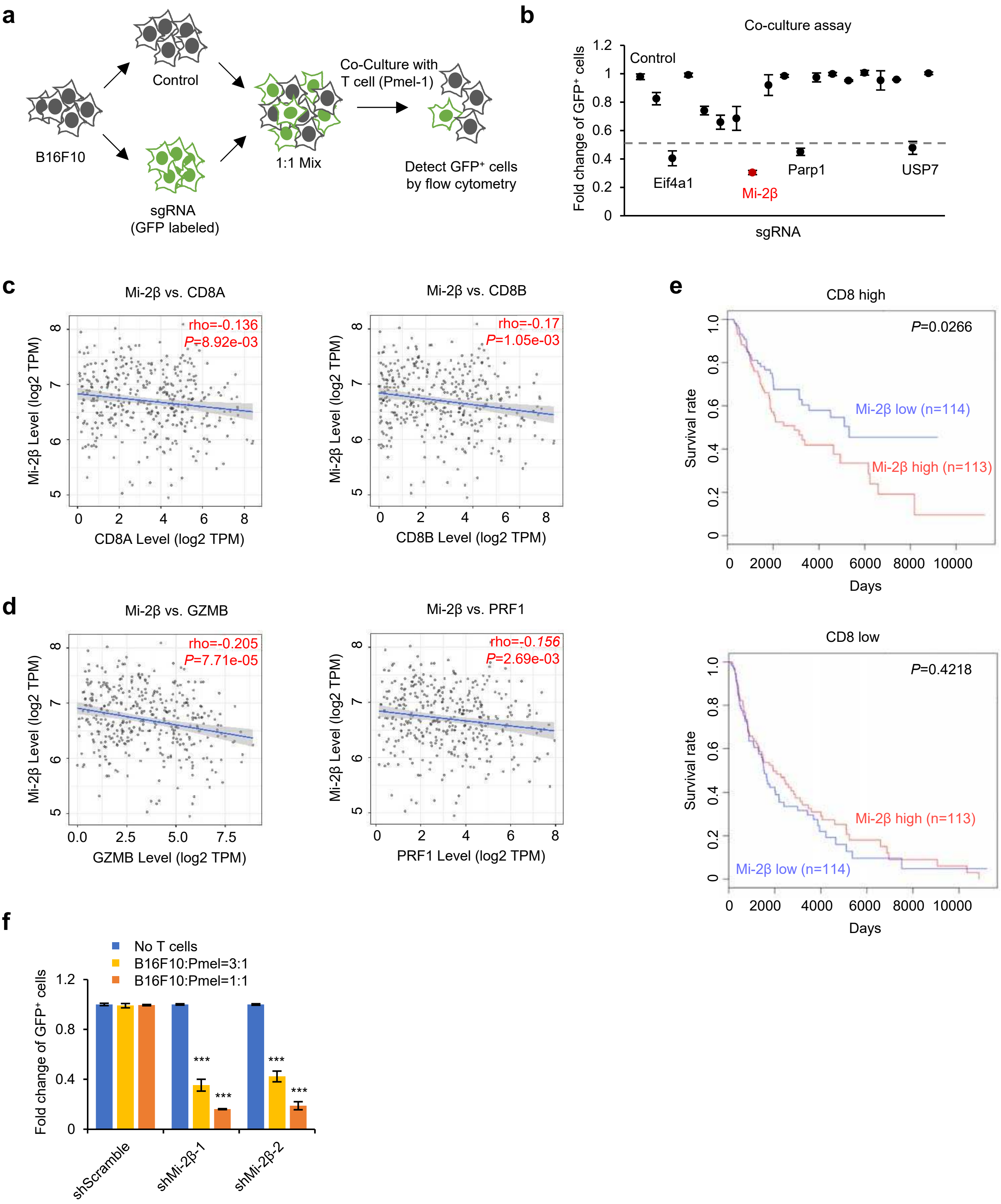
a
B16F10
Control
sgRNA
(GFP labeled)
1:1 Mix
Co-Culture with
T cell (Pmel-1)
Detect GFP⁺ cells
by flow cytometry
b
Co-culture assay
Fold change of GFP⁺ cells
1.2
1
0.8
0.6
0.4
0.2
0
Control
Eif4a1
Mi-2β
Parp1
USP7
sgRNA
c
Mi-2β vs. CD8A
rho=-0.136
P=8.92e-03
Mi-2β Level (log2 TPM)
CD8A Level (log2 TPM)
Mi-2β vs. CD8B
rho=-0.17
P=1.05e-03
CD8B Level (log2 TPM)
d
Mi-2β vs. GZMB
rho=-0.205
P=7.71e-05
GZMB Level (log2 TPM)
Mi-2β vs. PRF1
rho=-0.156
P=2.69e-03
PRF1 Level (log2 TPM)
e
CD8 high
P=0.0266
Survival rate
Mi-2β low (n=114)
Mi-2β high (n=113)
Days
CD8 low
P=0.4218
Mi-2β high (n=113)
Mi-2β low (n=114)
0
2000
4000
6000
8000
10000
f
No T cells
B16F10:Pmel=3:1
B16F10:Pmel=1:1
Fold change of GFP⁺ cells
1.2
0.8
0.4
0
***
shScramble
shMi-2β-1
shMi-2β-2

Fig. 1. Identification of Mi-2β regulating melanoma cell resistance to T cell-mediated killing. a, A schematic for co-culture assay. GFP-labelled B16F10 cells with target gene knockout were mixed with non-labelled control cell at a 1:1 ratio, which were then co-cultured with activated Pmel-1 T cells (at a ratio of 1:1) for 3 days. Survival GFP positive tumor cells were assayed with flow cytometry. **b,** Targeted genes for overcoming resistance to Pmel-1 T cell killing. Targeted genes were plotted based on the survival change of knockout tumor cells compared with control cells. The dash line represents survival ratio changes for 0.5 fold. **c,** Analysis of correlation between Mi-2β mRNA level and CD8A or CD8B as T cell infiltration markers in TCGA SKCM-Metastasis (n=368). Plots show the Spearman's correlation. **d,** Analysis of correlation between Mi-2β mRNA level and GZMB or PRF1 level as cytotoxicity markers. Analysis was performed as indicated in **(c)**. **e,** The survival curve of melanoma patients with different Mi-2β mRNA level. All patients in TCGA melanoma were divided into CD8 high or CD8 low groups based on the median expression. The available patients were further split into high- or low-expressing groups according to the median of Mi-2β mRNA level expression. Kaplan-Meier survival curves were shown, with the difference was examined using a log-rank test. **f,** GFP-labelled Mi-2β knockdown or shScramble B16F10 cells mixed with non-labelled B16F10 parental cells, and then were co-cultured with activated Pmel-1 T cells as indicated ratio for three days. The fold changes of the survival GFP-positive tumor cell were assayed with flow cytometry. Values represent mean ± SD *** $P < 0.001$.

Fig. 2

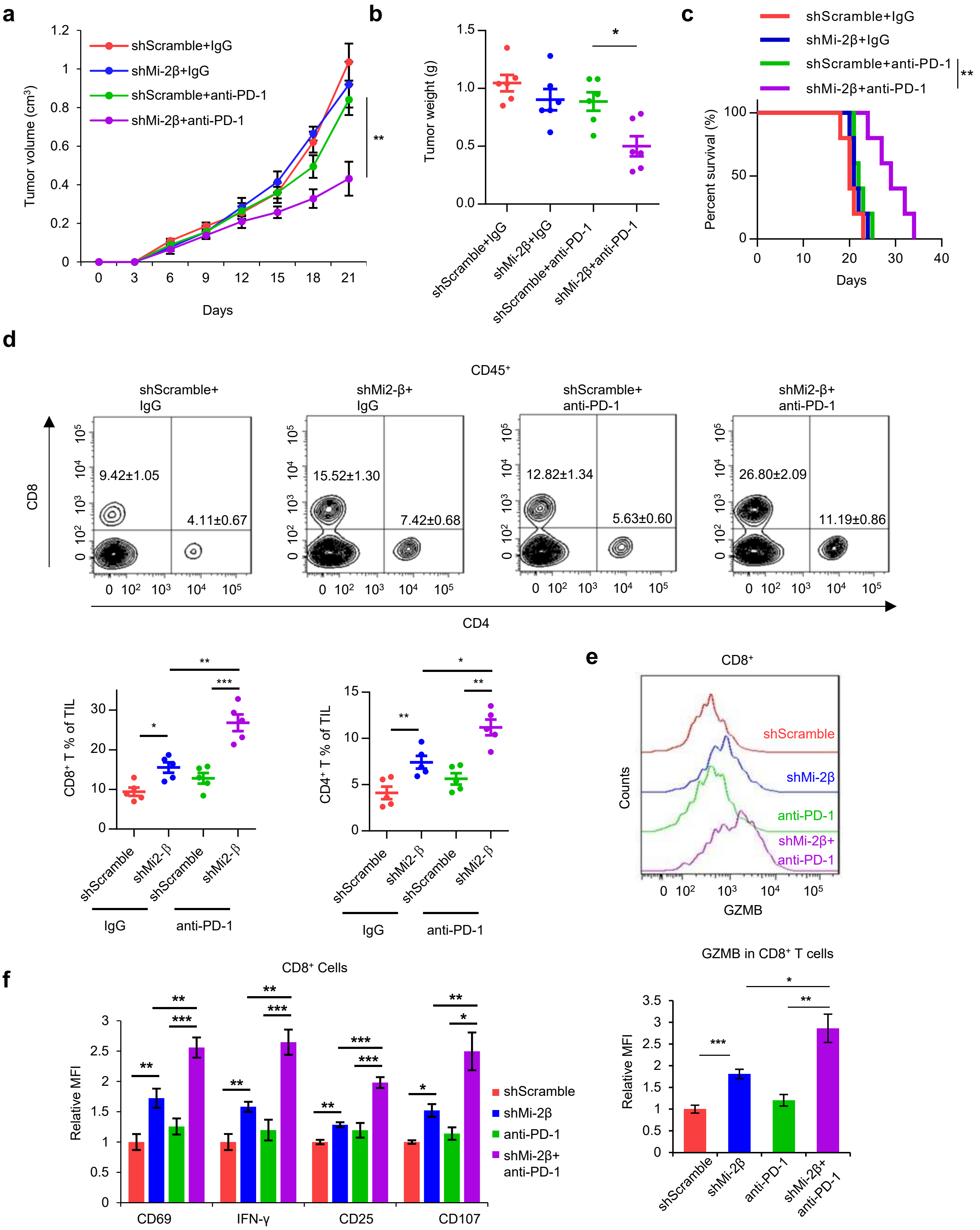

a
Tumor volume (cm^3)
Days
shScramble+IgG
shMi-2β+IgG
shScramble+anti-PD-1
shMi-2β+anti-PD-1
**
0
0.2
0.4
0.6
0.8
1
1.2
0
3
6
9
12
15
18
21
b
Tumor weight (g)
0.0
0.5
1.0
1.5
*
shScramble+IgG
shMi-2β+IgG
shScramble+anti-PD-1
shMi-2β+anti-PD-1
c
shScramble+IgG
shMi-2β+IgG
shScramble+anti-PD-1
shMi-2β+anti-PD-1
**
Percent survival (%)
100
50
0
0
10
20
30
40
Days
d
CD45$^+$
shScramble+ IgG
shMi2-β+ IgG
shScramble+ anti-PD-1
shMi2-β+ anti-PD-1
CD8
CD4
9.42±1.05
4.11±0.67
15.52±1.30
7.42±0.68
12.82±1.34
5.63±0.60
26.80±2.09
11.19±0.86
0
10^2
10^3
10^4
10^5
CD8$^+$ T % of TIL
0
10
20
30
*
**
***
shScramble
shMi2-β
shScramble
shMi2-β
IgG
anti-PD-1
CD4$^+$ T % of TIL
0
5
10
15
**
*
**
shScramble
shMi2-β
shScramble
shMi2-β
IgG
anti-PD-1
e
CD8$^+$
Counts
shScramble
shMi-2β
anti-PD-1
shMi-2β+ anti-PD-1
0
10^2
10^3
10^4
10^5
GZMB
GZMB in CD8$^+$ T cells
Relative MFI
0
0.5
1
1.5
2
2.5
3
3.5
***
*
**
shScramble
shMi-2β
anti-PD-1
shMi-2β+ anti-PD-1
f
CD8$^+$ Cells
Relative MFI
0
0.5
1
1.5
2
2.5
3
**
**
***
**
**
***
**
***
***
*
**
*
CD69
IFN-γ
CD25
CD107
shScramble
shMi-2β
anti-PD-1
shMi-2β+ anti-PD-1

Fig. 2. Mi-2β silencing improved the response to the anti-PD-1 therapy
a-c, Mice bearing Mi-2β knockdown or shScramble B16F10 cells were treated with i.p. injection of control IgG (10mg/kg) or anti-PD-1 (10mg/kg) antibodies at day 6, 9, 12, 15 and 18 after tumor cell inoculation, tumor volume (**a**), tumor weight (**b**) and mouse survival (**c**) were measured. Each group n=5. Tumor-infiltrating lymph cells in graft tumor were measured by flow cytometry. **d**, The population of $CD8^+$ and $CD4^+$ T cells were gated within $CD45^+$ T cells. **e,** The Granzyme B expression in $CD8^+$ T was measured and quantified with flow cytometry. **f,** Expression of activation markers of $CD8^+$ T cells were measured by flow cytometry assay. MFI represents mean fluorescence intensity. Log-rank test was used to determine statistical significance of *P* value for mouse Kaplan-Meier survival curves. Values represent mean ± SEM. $^*P < 0.05$, $^{**}P < 0.01$, $^{***} P < 0.001$.

Fig. 3

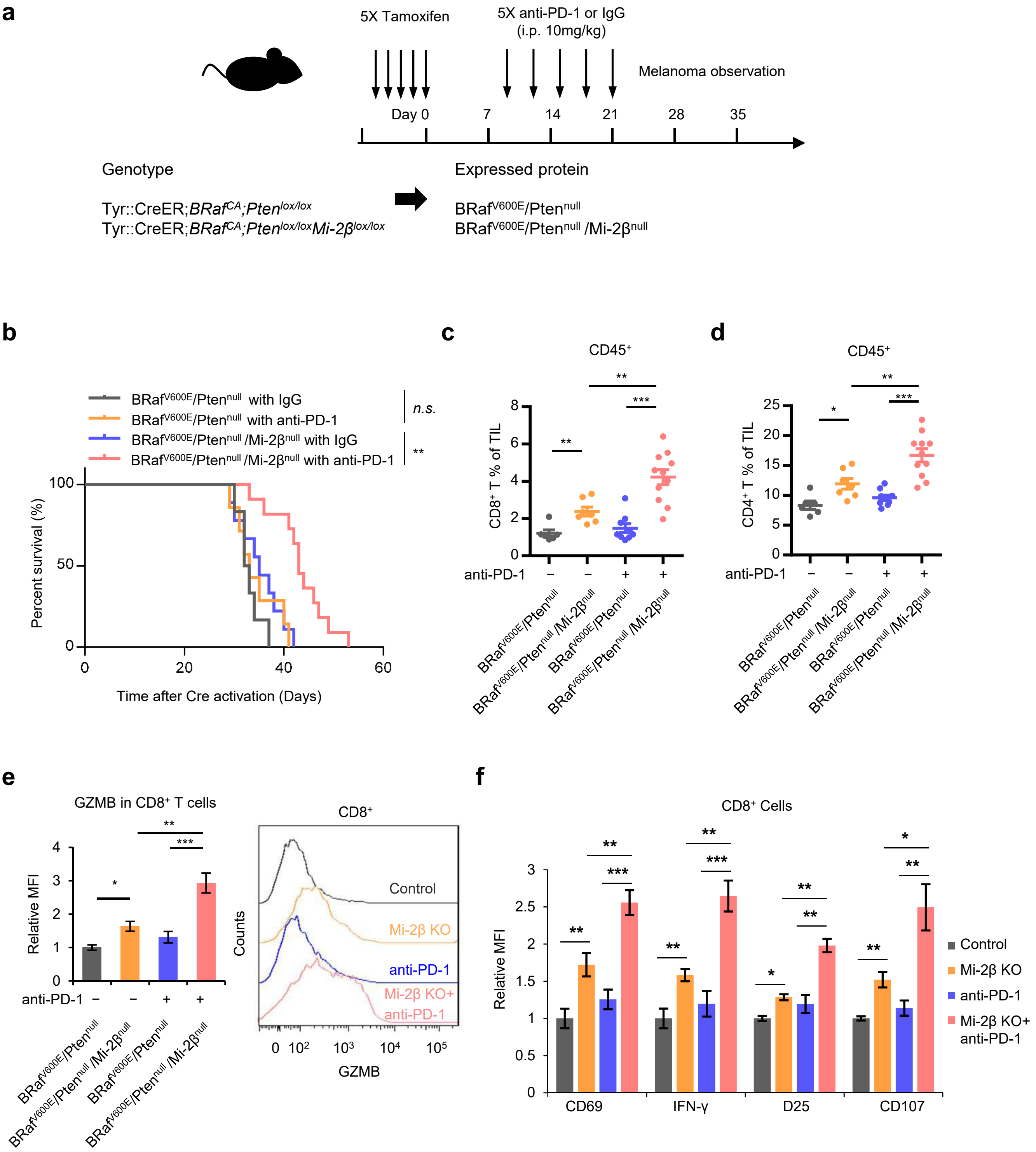
a
5X Tamoxifen
5X anti-PD-1 or IgG
(i.p. 10mg/kg)
Melanoma observation
Day 0
7
14
21
28
35
Genotype
Tyr::CreER;*BRaf^{CA};Pten$^{lox/lox}$*
Tyr::CreER;*BRaf^{CA};Pten$^{lox/lox}$Mi-2β$^{lox/lox}$*
Expressed protein
BRaf^{V600E}/Pten^{null}
BRaf^{V600E}/Pten^{null} /Mi-2β^{null}
b
BRaf^{V600E}/Pten^{null} with IgG
BRaf^{V600E}/Pten^{null} with anti-PD-1
BRaf^{V600E}/Pten^{null} /Mi-2β^{null} with IgG
BRaf^{V600E}/Pten^{null} /Mi-2β^{null} with anti-PD-1
n.s.
**
Percent survival (%)
100
50
0
0
20
40
60
Time after Cre activation (Days)
c
CD45^{+}
CD8^{+} T % of TIL
8
6
4
2
0
**
**
***
anti-PD-1
–
–
+
+
BRaf^{V600E}/Pten^{null}
BRaf^{V600E}/Pten^{null} /Mi-2β^{null}
BRaf^{V600E}/Pten^{null}
BRaf^{V600E}/Pten^{null} /Mi-2β^{null}
d
CD45^{+}
CD4^{+} T % of TIL
25
20
15
10
5
0
*
**
***
anti-PD-1
–
–
+
+
BRaf^{V600E}/Pten^{null}
BRaf^{V600E}/Pten^{null} /Mi-2β^{null}
BRaf^{V600E}/Pten^{null}
BRaf^{V600E}/Pten^{null} /Mi-2β^{null}
e
GZMB in CD8^{+} T cells
Relative MFI
4
3
2
1
0
*
**
***
anti-PD-1
–
–
+
+
BRaf^{V600E}/Pten^{null}
BRaf^{V600E}/Pten^{null} /Mi-2β^{null}
BRaf^{V600E}/Pten^{null}
BRaf^{V600E}/Pten^{null} /Mi-2β^{null}
CD8^{+}
Counts
Control
Mi-2β KO
anti-PD-1
Mi-2β KO+
anti-PD-1
0
10^{2}
10^{3}
10^{4}
10^{5}
GZMB
f
CD8^{+} Cells
Relative MFI
3
2.5
2
1.5
1
0.5
0
**
**
***
**
**
***
*
**
**
**
*
**
CD69
IFN-γ
D25
CD107
Control
Mi-2β KO
anti-PD-1
Mi-2β KO+
anti-PD-1

Fig. 3. Mi-2β deficiency induces responses to anti-PD-1 treatment for melanoma *in vivo*

a, A schematic for experimental strategy with anti-PD-1 treatment on genetically engineered melanoma mouse model. Mice carrying conditional alleles of *Tyr::CreER;BRaf*^{CA}*;Pten*$^{lox/lox}$ or *Tyr::CreER;BRaf*^{CA}*;Pten*$^{lox/lox}$*Mi-2β*$^{lox/lox}$ were administered with tamoxifen for constant 5 days to activate CreER to cause melanocyte-specific conversion of *Braf*^{CA} to *Braf*^{V600E}, and the conversion of the *Pten*$^{lox/lox}$ and *Mi-2β*$^{lox/lox}$ alleles to null alleles, which expressed proteins of BRaf^{V600E}/Pten^{null} or BRaf^{V600E}/Pten^{null} /Mi-2β^{null}, respectively. Mice with measurable tumors were randomly treated with either control IgG (10mg/kg) or anti-PD-1 (10mg/kg) antibodies by i.p. administration at day 9, 12, 15, 18 and 21 after Cre activation. **b,** Mouse survival of BRaf^{V600E}/Pten^{null} mice treated with IgG (n=6) or anti-PD-1 (n=7), and of BRaf^{V600E}/Pten^{null} /Mi-2β^{null} mice treated with IgG (n=9) or anti-PD-1 (n=11). Log-rank test was used for *P* value calculation. **c-d**, TILs were assayed with flow cytometry assay for the population of CD8$^+$ cells (**c**) and CD4$^+$ T cells (**d**) gated within CD45$^+$ T cells. **e,** Granzyme B expression in CD8$^+$ T was determined and quantified with flow cytometry. **f,** Expression of activation markers on CD8$^+$ T cells were determined with flow cytometry assay. MFI represents mean fluorescence intensity. Values represent mean ± SEM. $^*P < 0.05$, $^{**}P < 0.01$, $^{***} P < 0.001$.

Fig. 4

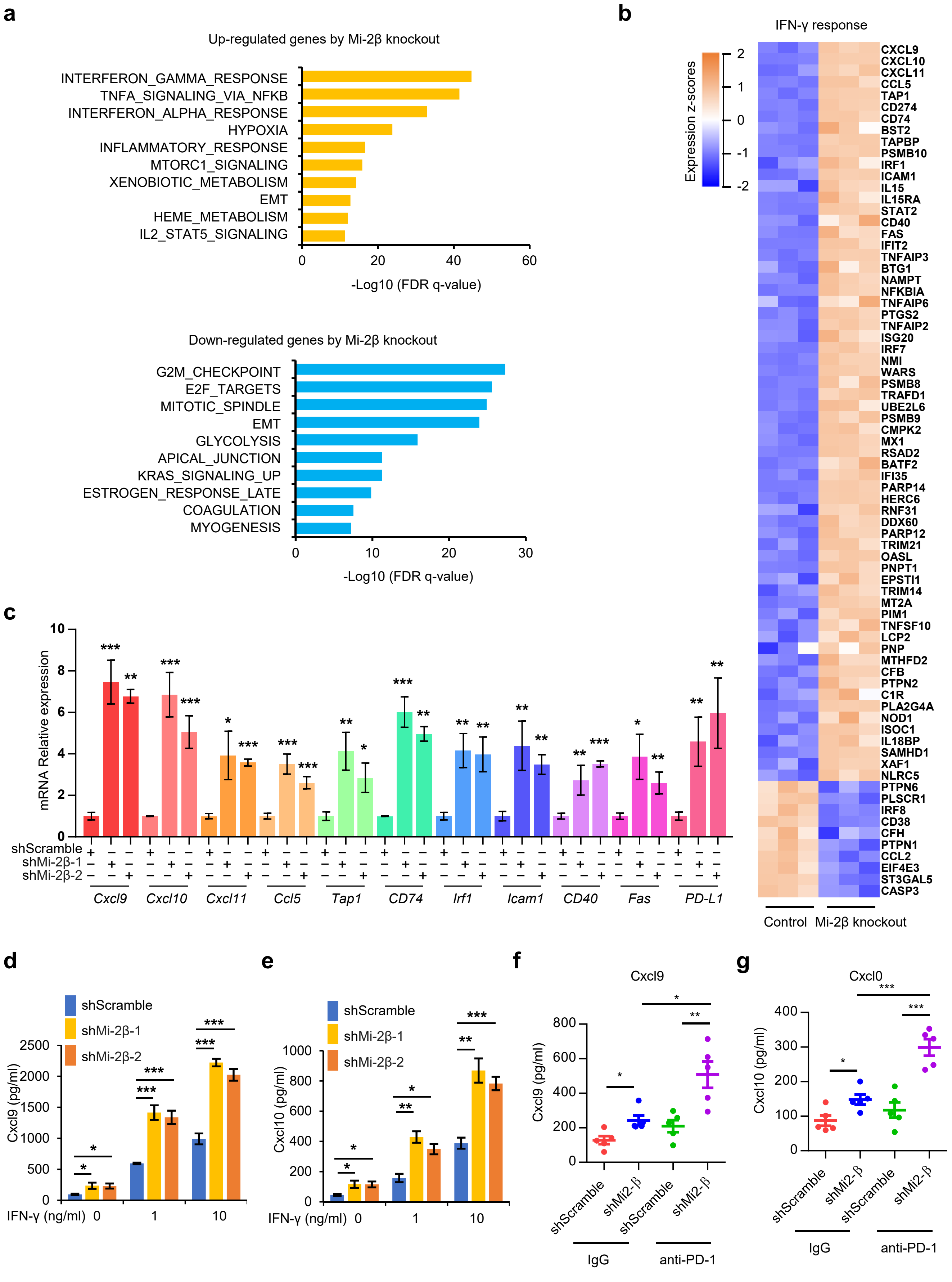
a
Up-regulated genes by Mi-2β knockout
INTERFERON_GAMMA_RESPONSE
TNFA_SIGNALING_VIA_NFKB
INTERFERON_ALPHA_RESPONSE
HYPOXIA
INFLAMMATORY_RESPONSE
MTORC1_SIGNALING
XENOBIOTIC_METABOLISM
EMT
HEME_METABOLISM
IL2_STAT5_SIGNALING
0
20
40
60
-Log10 (FDR q-value)
Down-regulated genes by Mi-2β knockout
G2M_CHECKPOINT
E2F_TARGETS
MITOTIC_SPINDLE
EMT
GLYCOLYSIS
APICAL_JUNCTION
KRAS_SIGNALING_UP
ESTROGEN_RESPONSE_LATE
COAGULATION
MYOGENESIS
0
10
20
30
-Log10 (FDR q-value)
b
IFN-γ response
Expression z-scores
2
1
0
-1
-2
CXCL9
CXCL10
CXCL11
CCL5
TAP1
CD274
CD74
BST2
TAPBP
PSMB10
IRF1
ICAM1
IL15
IL15RA
STAT2
CD40
FAS
IFIT2
TNFAIP3
BTG1
NAMPT
NFKBIA
TNFAIP6
PTGS2
TNFAIP2
ISG20
IRF7
NMI
WARS
PSMB8
TRAFD1
UBE2L6
PSMB9
CMPK2
MX1
RSAD2
BATF2
IFI35
PARP14
HERC6
RNF31
DDX60
PARP12
TRIM21
OASL
PNPT1
EPSTI1
TRIM14
MT2A
PIM1
TNFSF10
LCP2
PNP
MTHFD2
CFB
PTPN2
C1R
PLA2G4A
NOD1
ISOC1
IL18BP
SAMHD1
XAF1
NLRC5
PTPN6
PLSCR1
IRF8
CD38
CFH
PTPN1
CCL2
EIF4E3
ST3GAL5
CASP3
Control
Mi-2β knockout
c
mRNA Relative expression
10
8
6
4
2
0
shScramble
shMi-2β-1
shMi-2β-2
Cxcl9
Cxcl10
Cxcl11
Ccl5
Tap1
CD74
Irf1
Icam1
CD40
Fas
PD-L1
***
**
*
d
shScramble
shMi-2β-1
shMi-2β-2
Cxcl9 (pg/ml)
2500
2000
1500
1000
500
0
IFN-γ (ng/ml)
0
1
10
e
shScramble
shMi-2β-1
shMi-2β-2
Cxcl10 (pg/ml)
1000
800
600
400
200
0
IFN-γ (ng/ml)
0
1
10
f
Cxcl9
Cxcl9 (pg/ml)
800
600
400
200
0
shScramble
shMi2-β
shScramble
shMi2-β
IgG
anti-PD-1
g
Cxcl0
Cxcl10 (pg/ml)
400
300
200
100
0
shScramble
shMi2-β
shScramble
shMi2-β
IgG
anti-PD-1

Fig. 4. The enhanced IFN-γ signaling by Mi-2β knockout in melanoma

a, Microarray data analyzed for hallmark gene sets enriched for upregulated or downregulated mRNA in Mi-2β knockout and control B16F10 cells treated with IFN-γ for 24 hours. **b,** Heat map showing expression value (z-score expression) of IFN-γ signaling genes in control and Mi-2β knockout B16F10 cells in microarray data. **c,** The expressions of Mi-2β-regulated IFN-γ signaling genes were measured in IFN-γ-stimulated B16F10 cells with Mi-2β silencing by RT-qPCR. Values represent mean ± SD. **d-e,** The amount of secret Cxcl9 (**d**) or Cxcl10 (**e**) were measured in IFN-γ (0, 1, or 10 ng/mL, for 24 hours)-stimulated B16F10 cells with Mi-2β silencing by ELISA assay. Values represent mean ± SD. **f-g,** The graft melanomas were isolated to be cultured in PBS with the same amount cells for 4 hours (n=5), and then the secreted amount of the chemokines Cxcl9 (**f**) and Cxcl10 (**g**) in the culture medium were measured by ELISA assays. Values represent mean ± SEM. *$P < 0.05$, **$P < 0.01$, *** $P < 0.001$.

Fig. 5

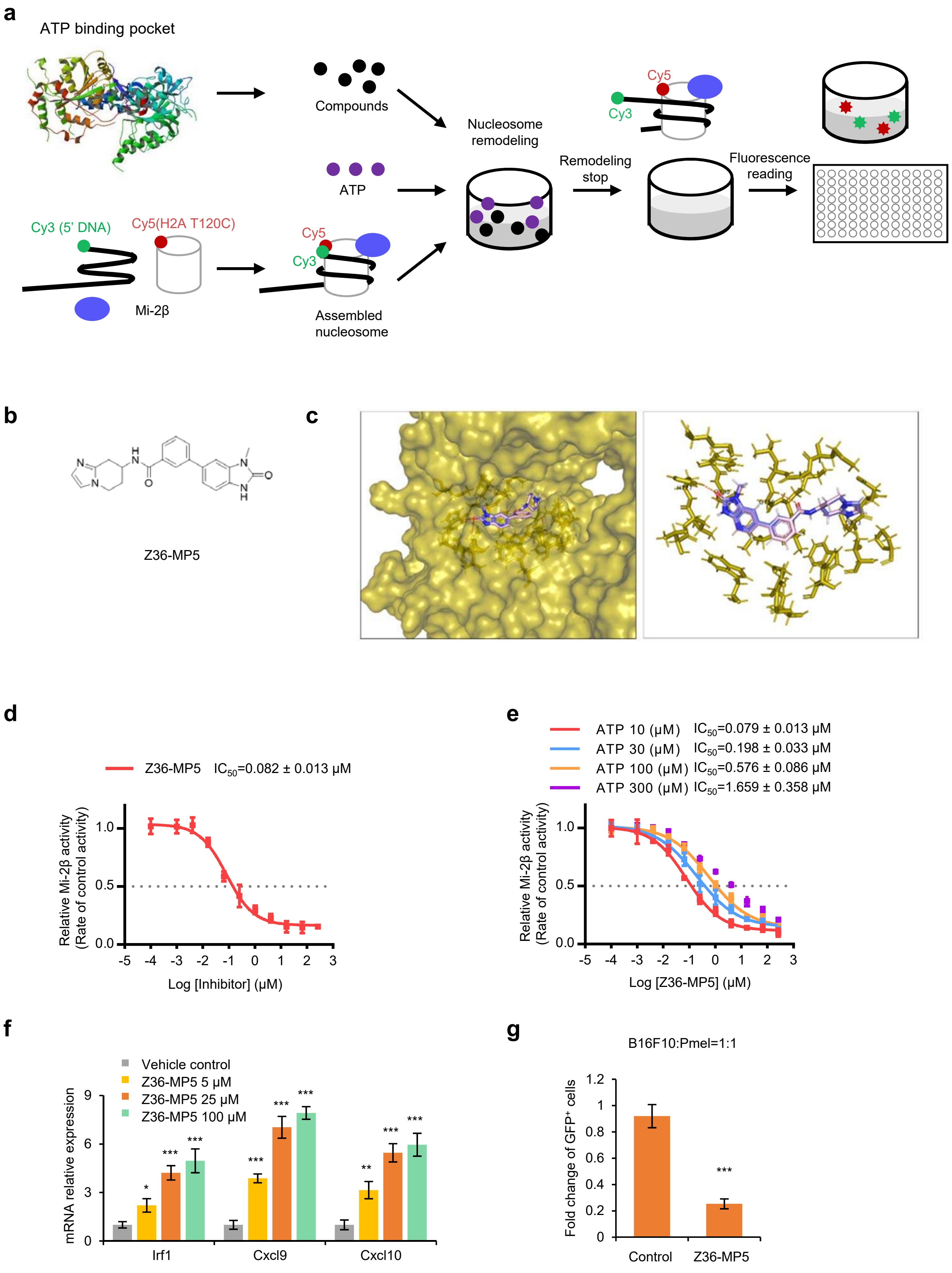
a
ATP binding pocket
Compounds
ATP
Cy3 (5' DNA)
Cy5(H2A T120C)
Mi-2β
Cy5
Cy3
Assembled nucleosome
Nucleosome remodeling
Remodeling stop
Cy5
Cy3
Fluorescence reading
b
Z36-MP5
c
d
Z36-MP5 IC$_{50}$=0.082 ± 0.013 μM
Relative Mi-2β activity (Rate of control activity)
1.0
0.5
0.0
-5 -4 -3 -2 -1 0 1 2 3
Log [Inhibitor] (μM)
e
ATP 10 (μM) IC$_{50}$=0.079 ± 0.013 μM
ATP 30 (μM) IC$_{50}$=0.198 ± 0.033 μM
ATP 100 (μM) IC$_{50}$=0.576 ± 0.086 μM
ATP 300 (μM) IC$_{50}$=1.659 ± 0.358 μM
Relative Mi-2β activity (Rate of control activity)
1.0
0.5
0.0
-5 -4 -3 -2 -1 0 1 2 3
Log [Z36-MP5] (μM)
f
Vehicle control
Z36-MP5 5 μM
Z36-MP5 25 μM
Z36-MP5 100 μM
mRNA relative expression
0
3
6
9
*
***
***
***
***
***
**
***
***
Irf1
Cxcl9
Cxcl10
g
B16F10:Pmel=1:1
Fold change of GFP$^+$ cells
0
0.2
0.4
0.6
0.8
1
1.2
***
Control
Z36-MP5

Fig. 5. Z36-MP5 was developed as a selective Mi-2β inhibitor

a, Schematic representing *in vitro* screen assay for testing Mi-2β chromatin modulatory activity using FRET-based nucleosome repositioning assay. **b,** The chemical structure of Z36-MP5. **c,** Orientations of Z36-MP5 to homologized Mi-2β. Z36-MP5 was docked into the ATP binding pocket of homologized Mi-2β. The methyl group of Z36-MP5 extended to a solvent-exposed channel lined with the side chains of Tyr729, Leu755, Met966, and Ile1163, with generating H-bonds via the O atom of keto group with His727, O atom of amide group with Gly756, and protonated N atom of imidazole group with Asp873. The atoms of Z36-MP5 were colored as follows: carbon pink, oxygen red, nitrogen blue, and hydrogen white. The H-bonds between Z36-MP5 and homologized Mi-2β were shown as light-yellow dash lines. **d,** The inhibitory activity of Z36-MP5 for Mi-2β chromatin modulatory activity, measured as fold changes of Mi-2β activity treated with control vehicle. Data, including IC_{50}, presents as means ± SD. **e,** The inhibitory activity of Z36-MP5 with IC_{50} values against Mi-2β at different ATP concentrations. Data are presented means ± SD. **f,** The expression of Cxcl9, Cxcl10 and Irf1 mRNA in B16F10 cells treated with Z36-MP5 as indicated concentration for 24 hours was determined with RT-qPCR assay. **g,** Z36-MP5-treated (25 μM) GFP-labelled B16F10 cells were pretreated with 10ng/ml of IFN-γ for 24 hours, before co-culture with activated Pmel-1 T cells at a ratio of 1:1 for three days. The fold changes of survival GFP-positive tumor cells were assayed with flow cytometry. Values represent mean ± SD $^{*}P < 0.05$, $^{**}P < 0.01$, $^{***}P < 0.001$.

Fig. 6

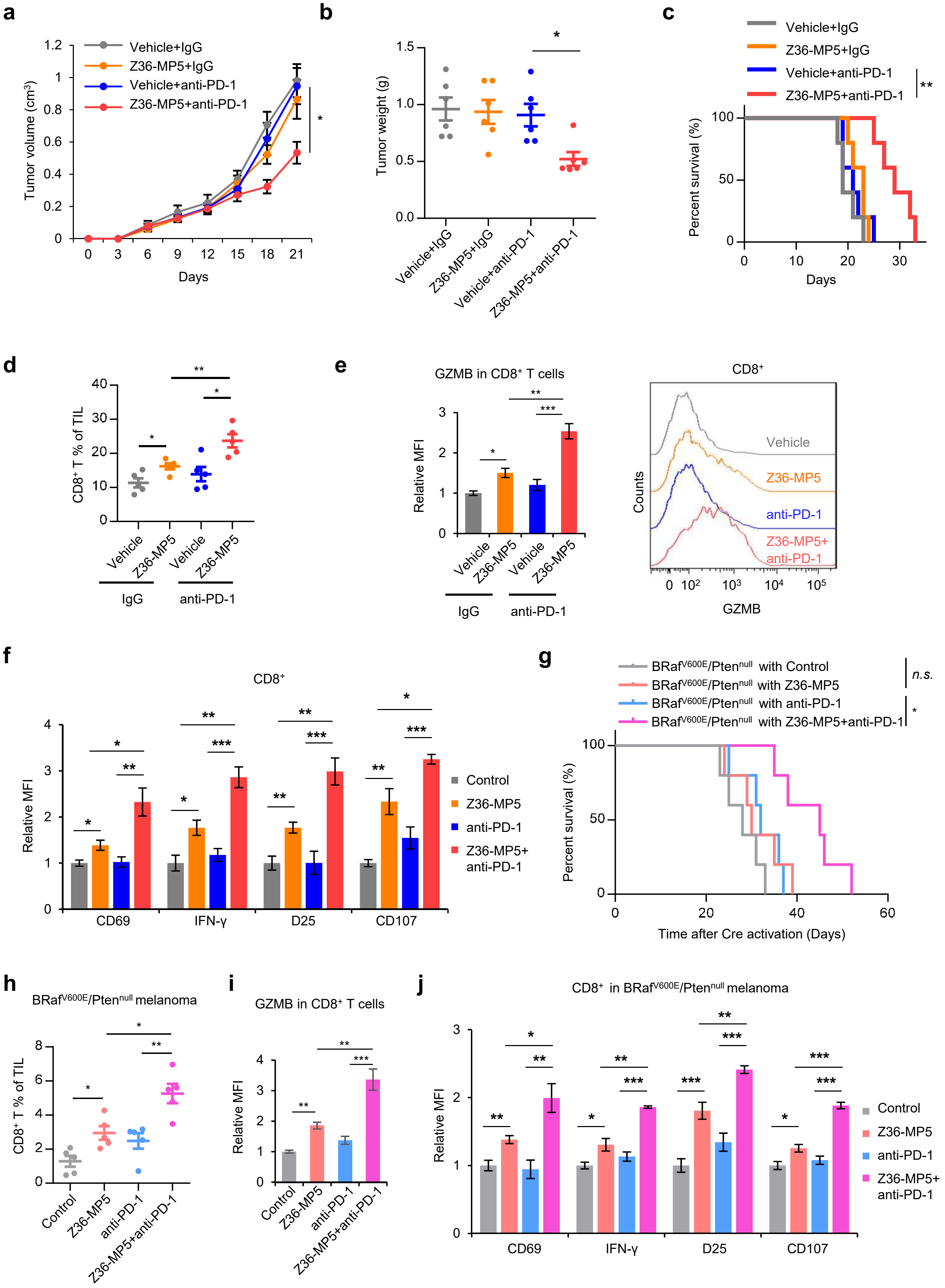
a
Tumor volume (cm³)
1.2
1
0.8
0.6
0.4
0.2
0
0 3 6 9 12 15 18 21
Days
Vehicle+IgG
Z36-MP5+IgG
Vehicle+anti-PD-1
Z36-MP5+anti-PD-1
*
b
Tumor weight (g)
1.5
1.0
0.5
0.0
*
Vehicle+IgG
Z36-MP5+IgG
Vehicle+anti-PD-1
Z36-MP5+anti-PD-1
c
Vehicle+IgG
Z36-MP5+IgG
Vehicle+anti-PD-1
Z36-MP5+anti-PD-1
**
Percent survival (%)
100
50
0
0 10 20 30
Days
d
CD8⁺ T % of TIL
40
30
20
10
0
**
*
*
Vehicle
Z36-MP5
Vehicle
Z36-MP5
IgG
anti-PD-1
e
GZMB in CD8⁺ T cells
Relative MFI
3
2
1
0
**
***
*
Vehicle
Z36-MP5
Vehicle
Z36-MP5
IgG
anti-PD-1
CD8⁺
Counts
Vehicle
Z36-MP5
anti-PD-1
Z36-MP5+
anti-PD-1
0 10² 10³ 10⁴ 10⁵
GZMB
f
CD8⁺
Relative MFI
4
3
2
1
0
*
*
**
**
*
***
**
**
***
*
**
***
CD69
IFN-γ
D25
CD107
Control
Z36-MP5
anti-PD-1
Z36-MP5+
anti-PD-1
g
BRaf^V600E/Pten^null with Control
BRaf^V600E/Pten^null with Z36-MP5
BRaf^V600E/Pten^null with anti-PD-1
BRaf^V600E/Pten^null with Z36-MP5+anti-PD-1
n.s.
*
Percent survival (%)
100
50
0
0 20 40 60
Time after Cre activation (Days)
h
BRaf^V600E/Pten^null melanoma
CD8⁺ T % of TIL
8
6
4
2
0
*
*
**
Control
Z36-MP5
anti-PD-1
Z36-MP5+anti-PD-1
i
GZMB in CD8⁺ T cells
Relative MFI
4
3
2
1
0
**
***
**
Control
Z36-MP5
anti-PD-1
Z36-MP5+anti-PD-1
j
CD8⁺ in BRaf^V600E/Pten^null melanoma
Relative MFI
3
2
1
0
*
**
**
**
***
*
**
***
***
***
***
*
CD69
IFN-γ
D25
CD107
Control
Z36-MP5
anti-PD-1
Z36-MP5+
anti-PD-1

Fig. 6. Combinational treatment with Z36-MP5 and anti-PD-1 antibodies suppressed cold melanoma growth

Mice bearing B16F10 cells were treated with control IgG or anti-PD-1 antibody, and vehicle control or Z36-MP5, as indicated. **a-b,** Tumor volume (**a**), and tumor weight (**b**) were measured. For each group n=5. **c,** Survival curve of mice with B16F10 cell grafts treated with control IgG or anti-PD-1 antibody, and vehicle control or Z36-MP5 as indicated was shown, with log-rank test for *P* value. **d,** Tumor-infiltrating lymph cells in tumor graft of each group mice were measured by flow cytometry. The population of $CD8^+$ was gated within $CD45^+$ T cells (Percentage of mean ± SEM). **e,** Granzyme B expression in $CD8^+$ T was determined and quantified. **f,** Expression of activation markers on $CD8^+$ T cells were determined with flow cytometry assay. MFI, mean fluorescence intensity. **g,** Mice carrying conditional alleles of $Tyr::CreER;BRaf^{CA};Pten^{lox/lox}$ were administered with tamoxifen for constant 5 days to activate CreER to cause melanocyte-specific conversion of $Braf^{CA}$ to $Braf^{V600E}$, and the conversion of the $Pten^{lox/lox}$ alleles to null, which express proteins of $\mathrm{BRaf}^{\mathrm{V600E}}/\mathrm{Pten}^{\mathrm{null}}$. Mice with measurable tumors were randomly treated with either control IgG (10mg/kg) or anti-PD-1 antibodies (10mg/kg) and/or Z36-MP5 (30mg/kg/day) by i.p. administration as indicated. For each group n=5. Mouse survival was shown with log-rank test for *p* value. **h-j,** Tumor infiltrating lymph cells (TILs) were assayed by flow cytometry to detect the population of $CD8^+$ T cells (**h**) gated within $CD45^+$ T cells. The expression of Granzyme B (**i**) and activation markers (**j**) in $CD8^+$ T was determined and quantified with flow cytometry assay. MFI, mean fluorescence intensity. Values represent mean ± SEM. $*P < 0.05$, $**P < 0.01$, $***P < 0.001$.

Extended Data Fig. 1

a

Gene	In CD8 High melanoma Hazard ratio	*p* value	In CD8 Low melanoma Hazard ratio	*p* value
EP400	3.077725034	0.009308	1.394838883	0.19255
Mi-2β	3.04172964	0.005057	0.941015851	0.830518
PRDM4	2.961124795	0.008813	1.210983739	0.416542
USP7	2.651929483	0.029028	0.997004792	0.992765
WDR5	2.434532166	0.005791	1.494383478	0.089879
EIF4A1	2.400954909	0.022633	1.139344114	0.57291
SMARCD1	2.377998009	0.009434	1.296210437	0.268984
NCOA6	2.322416345	0.014943	1.237998488	0.449286
CARM1	2.238366202	0.034001	1.502047368	0.103204
SSRP1	2.135438979	0.023566	0.833931286	0.38984
NOP2	2.080974635	0.006177	1.306468121	0.167779
RCOR1	1.990697365	0.045799	0.846541023	0.46292
HDGF	1.955529658	0.019302	1.154629805	0.490705
RSAD1	1.921663999	0.038278	1.08334709	0.729356
FBL	1.919388828	0.013922	1.159731629	0.404587
HDAC4	1.834004067	0.016545	1.019634897	0.918457
PARP1	1.803669284	0.048059	1.478467699	0.06788
RPS6KA4	1.742078968	0.041251	1.347419903	0.067517
IGHMBP2	1.511938346	0.026357	1.069187784	0.655259
CHD7	1.502499164	0.029759	1.019155831	0.901018
SKA1	1.483982942	0.031181	1.124368885	0.345802
TBL1X	1.43219622	0.021107	0.938361306	0.46205
HMGA1	1.399686515	0.029087	0.991273431	0.939065
SP140	0.768734953	0.028619	0.871050369	0.110468
ATM	0.732597615	0.048307	0.788387476	0.05981
HIST4H4	0.732471944	0.024692	1.212789354	0.063891
SMARCA1	0.731147036	0.028807	1.004283811	0.963612
SAP30	0.699107547	0.044097	0.797226467	0.070709
CENPQ	0.694417749	0.030499	0.811653659	0.070862
BAZ2B	0.682722632	0.02704	0.834731264	0.127366
PARP10	0.671937122	0.009003	0.970910507	0.811989
CBX7	0.669175702	0.009027	0.836586235	0.082602
ZCWPW1	0.664555481	0.01047	0.907483414	0.339016
SP140L	0.642056347	0.003639	0.884322465	0.115257
NBN	0.62962183	0.024395	0.794977803	0.135232
DDX60L	0.629429879	0.001169	0.831138542	0.052775
MTF2	0.628240004	0.019587	0.816130629	0.163629
KAT2B	0.619503511	0.000862	0.907903199	0.308433
DTX3L	0.609078015	0.006684	0.810641019	0.083021
PARP14	0.579181221	0.002461	0.798902129	0.060219
DHX58	0.579105591	0.000805	1.117977278	0.304337
DZIP3	0.557090151	0.0014	0.837524823	0.211229
SP110	0.549607372	0.00616	0.944204756	0.70924
ZMYM6	0.548495177	0.011895	0.724698648	0.054367
AEBP2	0.527322576	0.00836	0.857521906	0.420235
BRD7	0.517959176	0.023703	0.819168682	0.297593
ING4	0.516180263	0.028097	0.745467502	0.131765
PARP9	0.510245158	0.000195	0.858791564	0.166766
SP100	0.506549491	0.000969	0.841069607	0.197369
PHF1	0.497779549	0.018615	0.950183057	0.78662
H2AFV	0.484234238	0.030851	1.106401561	0.672329
CBX3	0.470368599	0.001441	0.910166189	0.611973
DPY30	0.430340646	0.031163	0.81318161	0.397192
PHF12	0.417466293	0.042671	0.928983009	0.783979
HP1BP3	0.412182147	0.016378	1.102962699	0.722581

b

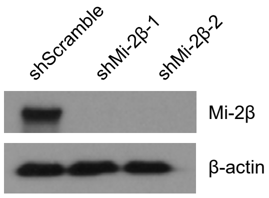

Extended Data Fig. 1. Hazard ratio of epigenetic factors dependent on CD8 T cell infiltration
a, Hazard ratio of epigenetic factor in melanoma patients depending on level of CD8 T infiltration. All patients in TCGA melanoma were divided into CD8 high or CD8 low groups based on CD8A median expression. The hazard ratio and *P* values were calculated. The genes (n=55), whose mRNA expression levels significantly correlated with hazard ratio in patients with high CD8 T cell infiltration only, but not in patients with low CD8 T cell infiltration, were shown. **b,** Western blot assay showing the efficiency of shMi-2β knockdown in B16F10 cells.

Extended Data Fig. 2

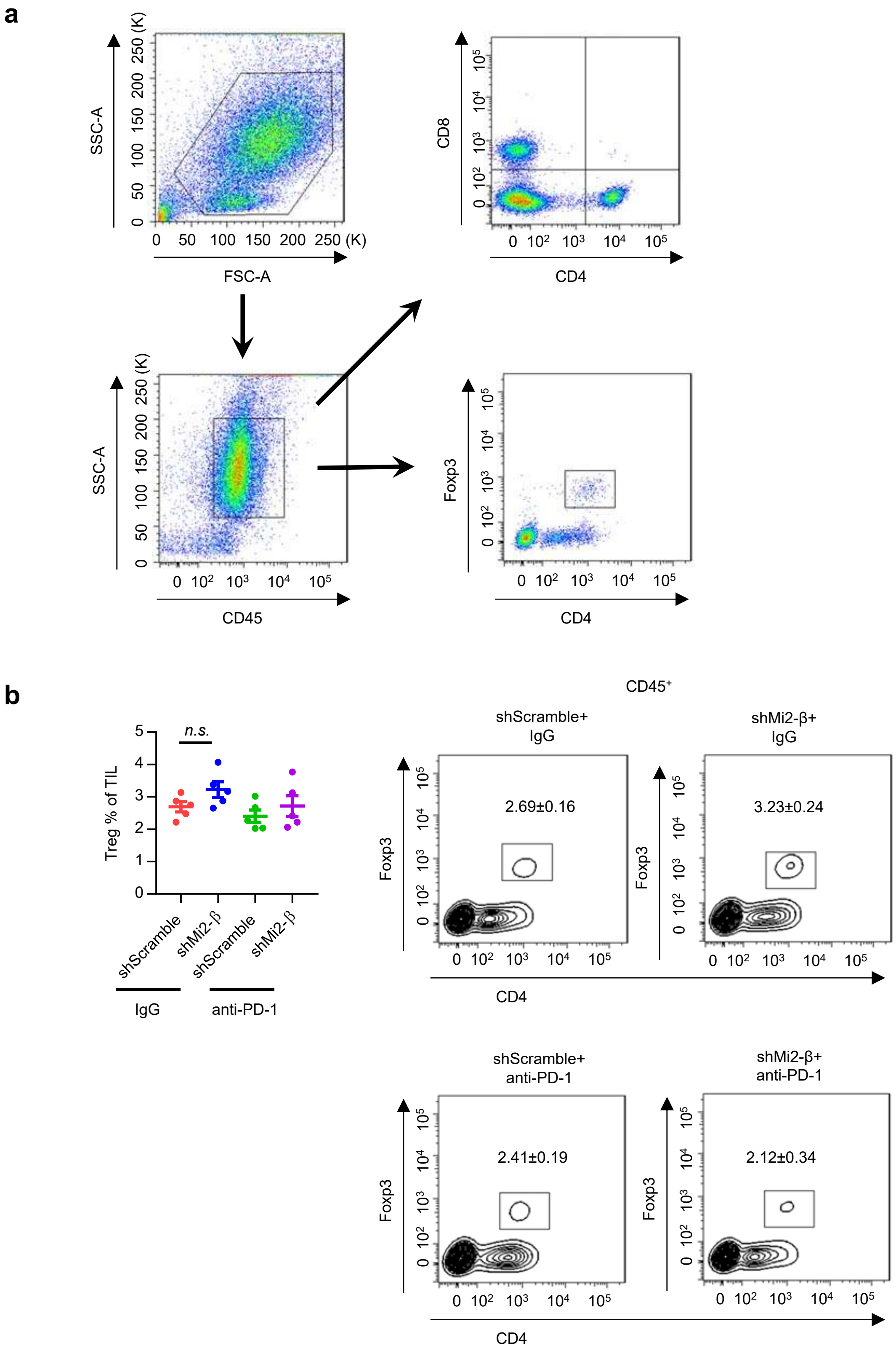

Extended Data Fig. 2. Treg population in Mi-2β silencing melanoma graft with anti-PD-1
Mice bearing graft of Mi-2β knockdown or shScramble B16F10 cells were treated with i.p. injection of control IgG (10mg/kg) or anti-PD-1 antibodies (10mg/kg) at day 6, 9, 12, 15 and 18 after tumor cell inoculation. Each group n=5. Tumor-infiltrating lymph cells were assayed by flow cytometry. **a,** The representative gating cell population were shown. **b,** The population of Treg cells were quantified within CD45$^+$ T cells. Values represent mean ± SEM. *n.s.* represents no significance.

Extended Data Fig. 3

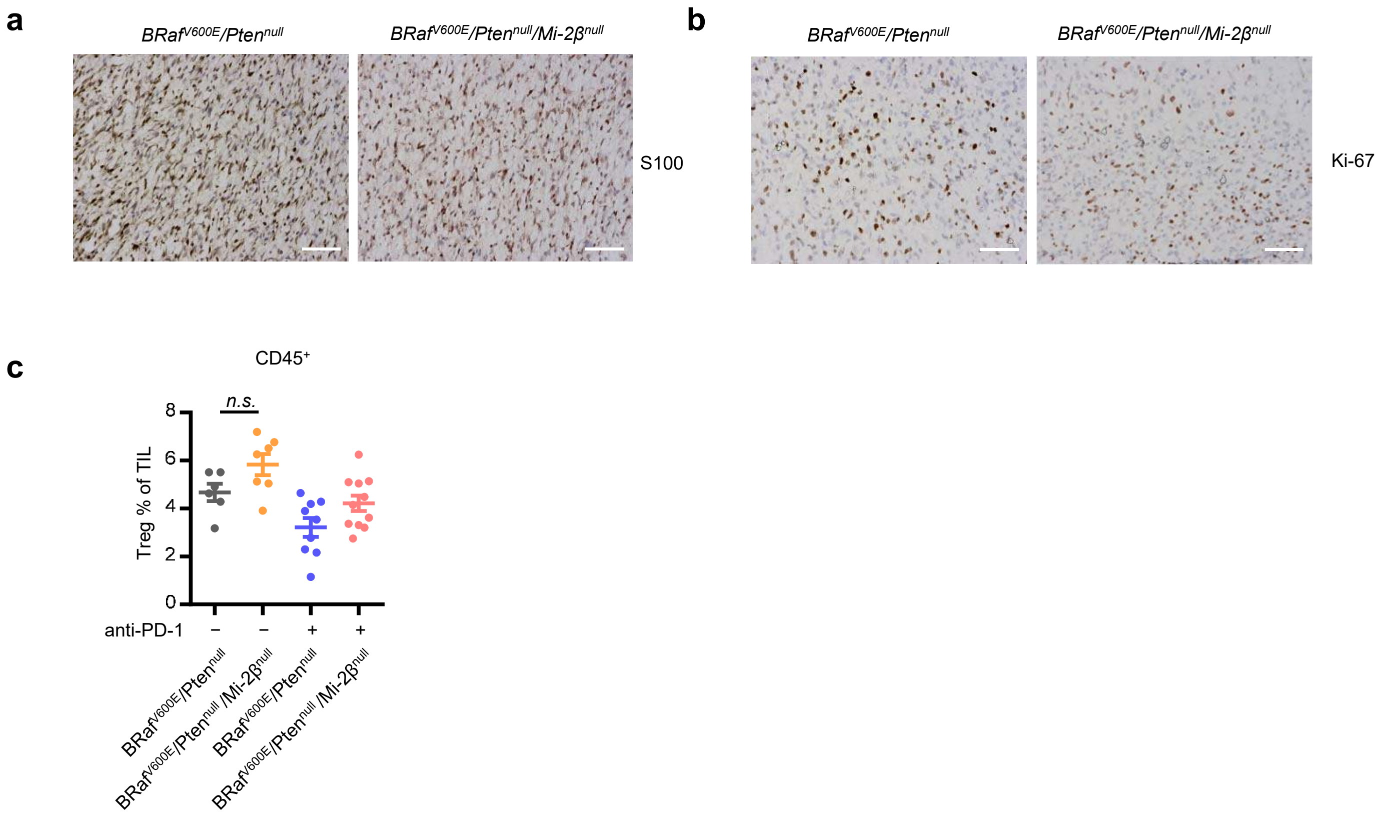

Extended Data Fig. 3. Analysis of Mi-2β deficient melanoma tumor

a-b, The melanomas from BRaf^{V600E}/Pten^{null} mice and BRaf^{V600E}/Pten^{null} /Mi-2β^{null} mice were prepared and processed for immunohistochemistry staining to detect the expression of melanoma marker of S100 (**a**), and tumor proliferation marker of Ki-67 (**b**). **c,** Treg cells in TILs were assayed by flow cytometry assay for the population within CD45^{+} T cells for each groups. Values represent mean ± SEM. Scale bar=200 µm. *n.s.* represents no significance.

Extended Data Fig. 4

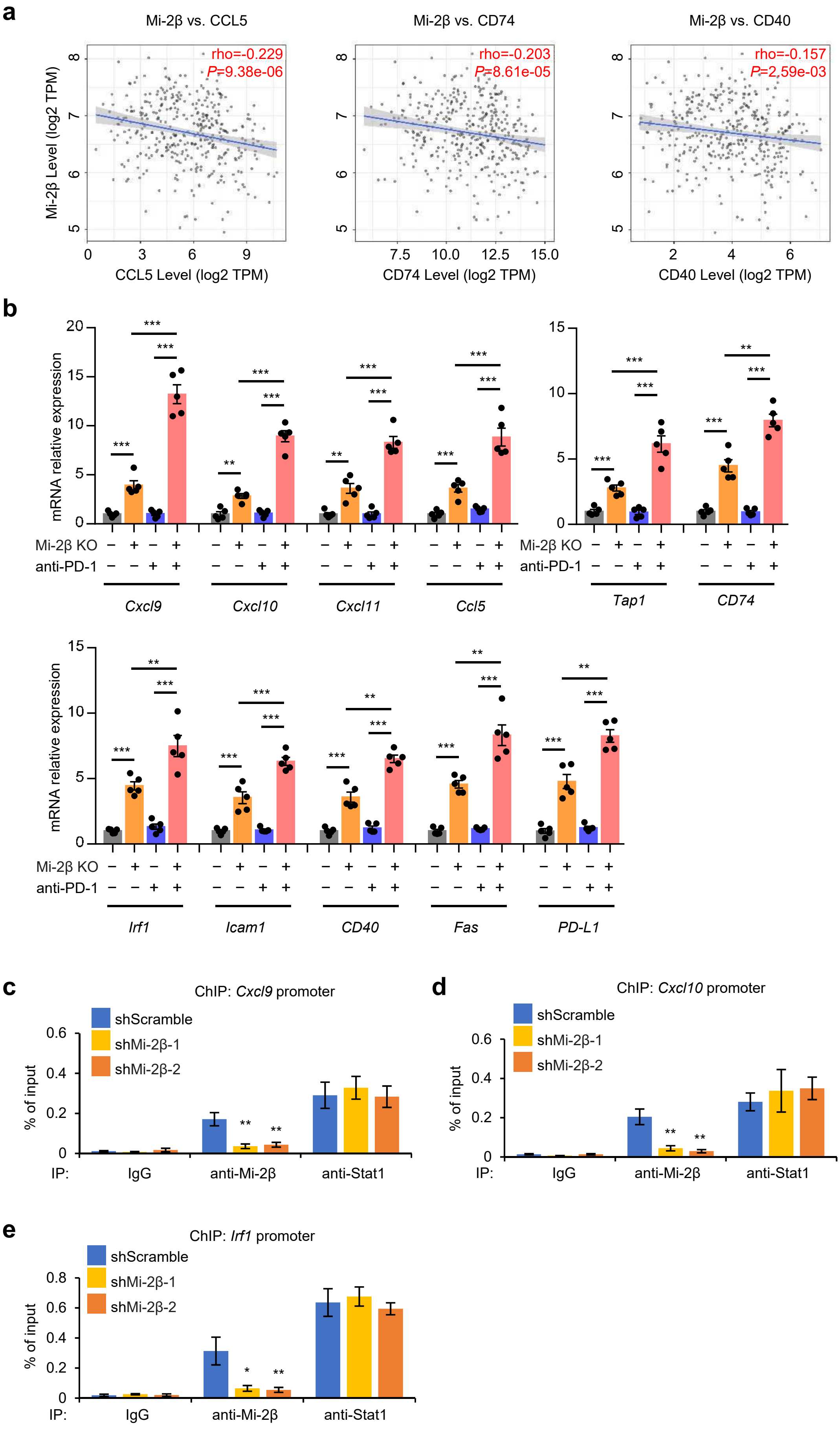

Extended Data Fig. 4. Mi-2β directly regulates inflammatory genes

a, Plots showed the Spearman's correlation between Mi-2β mRNA level and CCL5, CD74 or CD40 mRNA expression level in RNA-seq data in TCGA SKCM-Metastasis (n=368). **b,** The Mi-2β-regulated downstream target genes in IFN-γ signaling were measured in $\mathrm{BRaf}^{\mathrm{V600E}}/\mathrm{Pten}^{\mathrm{null}}$ and $\mathrm{BRaf}^{\mathrm{V600E}}/\mathrm{Pten}^{\mathrm{null}}$ /$\mathrm{Mi\text{-}2\beta}^{\mathrm{null}}$ melanoma in mice treated with IgG control and/or anti-PD-1 with RT-qPCR assay. Values represent mean ± SEM. **c-e,** ChIP assays were performed to detect Mi-2β binding on the promoter of *Cxcl9* (**c**), *Cxcl10* (**d**) and *Irf1* (**e**) genes in both shScramble and Mi-2β knockdown B16F10 cells, and IP with anti-Stat1 was used as the positive binding control. Values represent mean ± SD. $^{*}p < 0.05$, $^{**}p < 0.01$, $^{***}p < 0.001$.

Extended Data Fig. 5

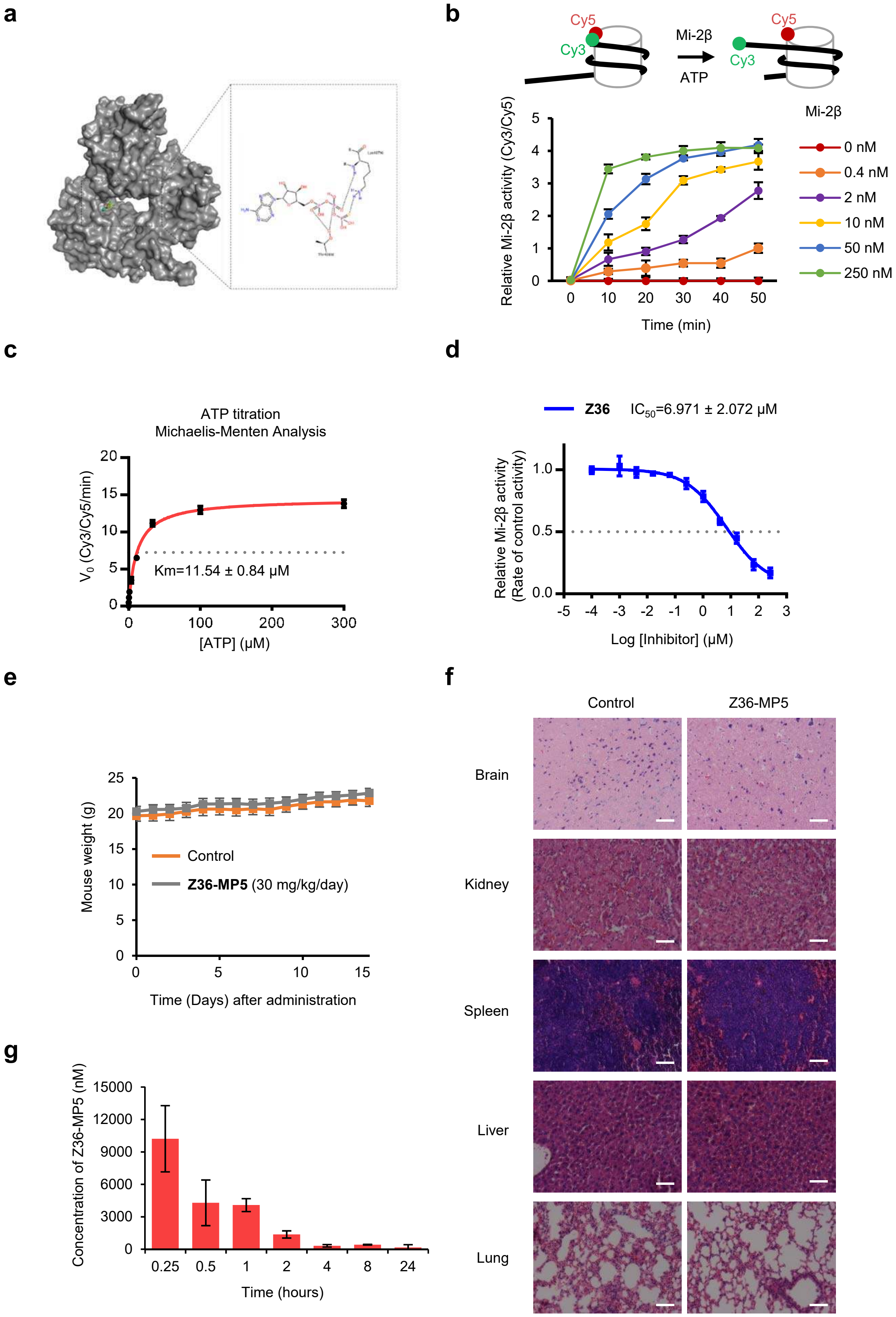

Extended Data Fig. 5. ***In vitro*** **assays for Mi-2β inhibitors**

a, The candidate protein structure for homology modelling. 3MWY depicted the interaction of ATP and its binding pocket. **b,** The FRET-based nucleosome repositioning assays were performed with different concentrations of Mi-2β and a non-limiting ATP concentration (1 mM) for the indicated incubation time. Values represent mean ± SD. **c,** The ATP titration (concentrations ranging from 0.1 to 300 μM) was performed with the FRET-based nucleosome repositioning assays. The Michaelis-Menten equation was performed to calculate the apparent ATP Km, with the ATP Km of 11.54 μM. **d,** The inhibitory activity of Z36 for Mi-2β chromatin modulatory activity, measured as fold changes of Mi-2β activity treated with control vehicle. Data presents as means ± SD. **e,** The body weight changes of C57BL/6J mice treated with Z36-MP5 (30mg/kg/day) for 2 weeks. Data are mean ± SD (n=5). **f,** H&E staining of tissues in C57BL/6J mice treated with or without Z36-MP5 (30mg/kg/day) for 2 weeks. Scale bar=200 μm. **g,** Blood concentration profiles of Z36-MP5 after a single-dose intraperitoneal injection into 3 male Sprague-Dawley (SD) rats. Values represents the mean ± SD.

Extended Data Fig. 6

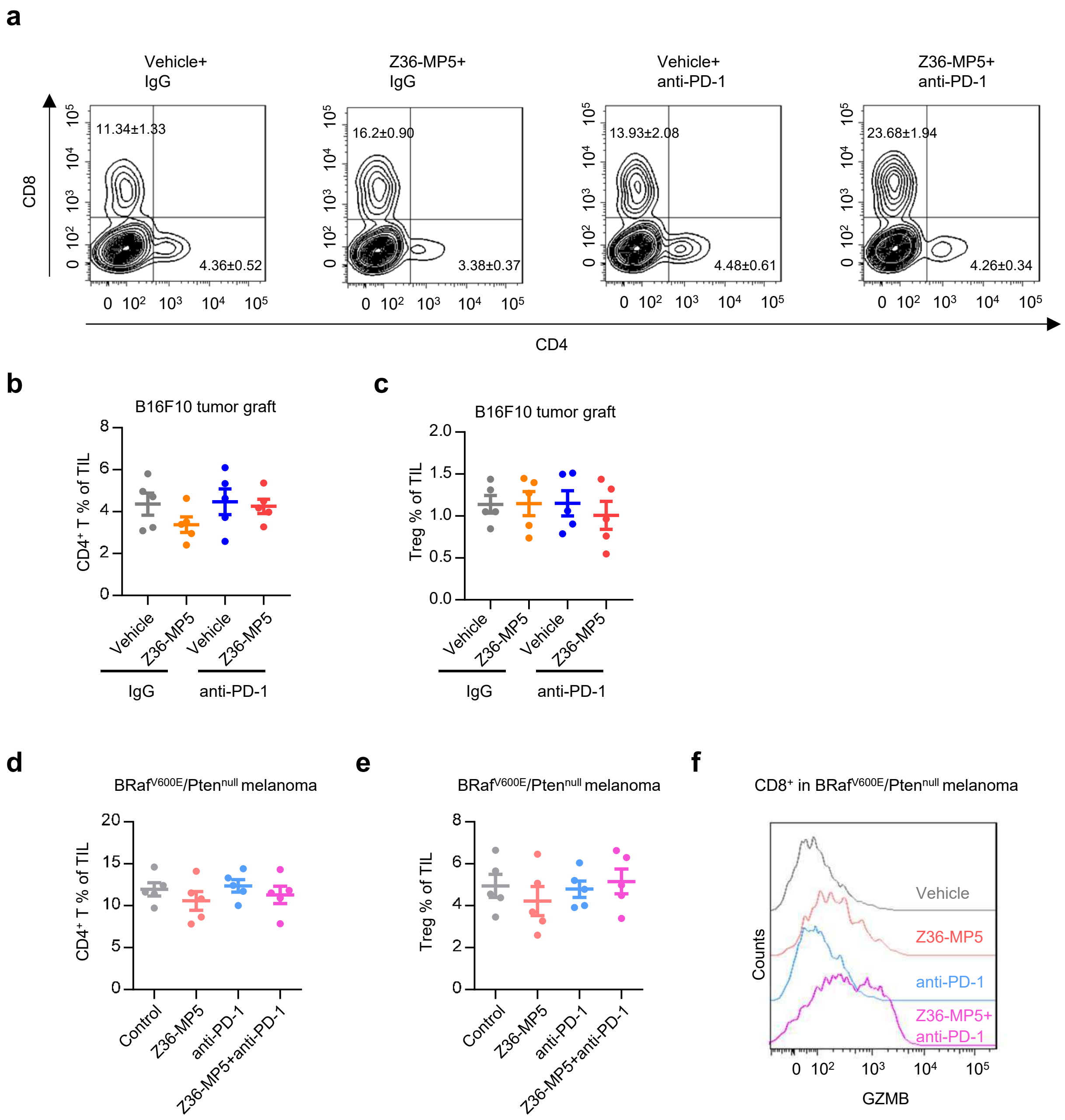

Extended Data Fig. 6. Combinational treatment of Z36-MP5 and anti-PD-1 antibodies in melanoma
Mice bearing B16F10 cells were treated with control IgG or anti-PD-1 antibody, and vehicle control or Z36-MP5, as indicated. For each group n=5. Tumor-infiltrating lymph cells were assayed by flow cytometry for CD4 and CD8 T cell population. **a,** The representative figure of flow cytometry for $CD4^+$ and $CD8^+$ T cells. **b,** The population of $CD4^+$ T cell in total $CD45^+$ cells. **c,** Treg cell population in $CD45^+$ cell. **d-f,** Transgenic mice expressing $BRaf^{V600E}/Pten^{null}$ with measurable tumors were randomly treated with either control IgG antibodies (10mg/kg) or anti-PD-1 antibodies (10mg/kg) and Z36-MP5 (30mg/kg/day) or vehicle control by i.p. administration. For each group n=5. TILs were assayed by flow cytometry assay. The population of tumor-infiltrating $CD4^+$ T cells **(d)** and Treg cells **(e)** gated within $CD45^+$ T cells, and the expression of Granzyme B **(f)** in $CD8^+$ T cell were determined and quantified with flow cytometry assay. MFI, mean fluorescence intensity. Values represent mean ± SEM.

Extended Data Table 1. Top 10 GSEA-Hallmark upregulated genes

Gene Set Name	# Genes in Gene Set (K)	# Genes in Overlap (k)	k/K	p-value	FDR q-value
HALLMARK_INTERFERON_GAMMA_RESPONSE	200	66	0.33	4.15E-47	2.08E-45
HALLMARK_TNFA_SIGNALING_VIA_NFKB	200	63	0.315	1.31E-43	3.28E-42
HALLMARK_INTERFERON_ALPHA_RESPONSE	97	41	0.423	7.5E-35	1.25E-33
HALLMARK_HYPOXIA	200	46	0.23	1.29E-25	1.61E-24
HALLMARK_INFLAMMATORY_RESPONSE	200	38	0.19	2.35E-18	2.35E-17
HALLMARK_MTORC1_SIGNALING	200	37	0.185	1.65E-17	1.37E-16
HALLMARK_XENOBIOTIC_METABOLISM	200	35	0.175	7.35E-16	5.25E-15
HALLMARK_EPITHELIAL_MESENCHYMAL_TRANSITION	200	33	0.165	2.85E-14	1.78E-13
HALLMARK_HEME_METABOLISM	200	32	0.16	1.68E-13	9.35E-13
HALLMARK_IL2_STAT5_SIGNALING	200	31	0.155	9.57E-13	4.79E-12

Extended Data Table 2. Top 10 GSEA-Hallmark downregulated genes

Gene Set Name	# Genes in Gene Set (K)	# Genes in Overlap (k)	k/K	p-value	FDR q-value
HALLMARK_G2M_CHECKPOINT	200	50	0.25	9.96E-30	4.98E-28
HALLMARK_E2F_TARGETS	200	48	0.24	9.97E-28	2.49E-26
HALLMARK_MITOTIC_SPINDLE	199	47	0.236	7.55E-27	1.26E-25
HALLMARK_EPITHELIAL_MESENCHYMAL_TRANSITION	200	46	0.23	8.92E-26	1.12E-24
HALLMARK_GLYCOLYSIS	200	37	0.185	1.24E-17	1.24E-16
HALLMARK_APICAL_JUNCTION	200	31	0.155	7.63E-13	5.45E-12
HALLMARK_KRAS_SIGNALING_UP	200	31	0.155	7.63E-13	5.45E-12
HALLMARK_ESTROGEN_RESPONSE_LATE	200	29	0.145	2.24E-11	1.4E-10
HALLMARK_COAGULATION	138	21	0.152	5.19E-09	2.88E-08
HALLMARK_MYOGENESIS	200	25	0.125	1.19E-08	5.94E-08

Extended Data Table 3. Profile of Z36-MP5 inhibition on ATPases

ATPase	**Reference**	**Sequence**	**Labeling Site**	**Inhibition (%) by 1µM Z36-MP5**
AARS	UniRef100_P49588	AGGKHNDLDDVGKDVYHHTFFEMLGSWSFGDYFK	ATP Binding Site	-29.97
ABCB10	UniRef100_Q9NRK6	NVHFAYPARPEVPIFQDFSLSIPSGSVTALVGPSGSGKSTVLSLLLR	ATP Binding Site	-6.14
ABCB6	UniRef100_Q9NP58	ETLQDVSFTVMPGQTLALVGPSGAGKSTILR	ATP Binding Site	8.49
ABCB7	UniRef100_O75027	VAIVGGSGSGKSTIVR	ATP Binding Site	0.34
ABCC1	UniRef100_P33527	TGAGKSSLTLGLFR	ATP Binding Site	-0.23
ABCC1	UniRef100_P33527	SDPPTLNGITFSIPEGALVAVVGQVGCGKSSLLSALLAEMDKVEGHVAIK	ATP Binding Site	-7.84
ABCC10	UniRef100_Q5T3U5	TGSGKSSLLLVLFR	ATP Binding Site	-3.83
ABCC2	UniRef100_Q92887	TGAGKSSLTNCLFR	ATP Binding Site	4.09
ABCC3	UniRef100_O15438	TGAGKSSMTLCLFR	ATP Binding Site	4.57
ABCC3	UniRef100_O15438	GALVAVVGPVGCGKSSLVSALLGEMEK	ATP Binding Site	9.43
ABCC4	UniRef100_O15439	TGAGKSSLISALFR	ATP Binding Site	1.76
ABCC4	UniRef100_O15439	ASETPTLQGLSFTVRPGELLAVVGPVGAGKSSLLSAVLGELAPSHGLVSVHGR	ATP Binding Site	8.93
ABCD3	UniRef100_P28288	SGANVLICGPNGCGKSSLFR	ATP Binding Site	3.07
ABCD4	UniRef100_O14678	ISEGQSLLITGNTGTGKTSLLR	ATP Binding Site	11.24
ABCE1	UniRef100_P61221	LPIPRPGEVLGLVGTNGIGKSTALK	ATP Binding Site	-4.76
ABCF1	UniRef100_Q8NE71	ICIVGPNGVGKSTLLLLLTGK	ATP Binding Site	-8.08
ABCF2	UniRef100_Q9UG63	VALVGPNGAGKSTLLK	ATP Binding Site	-7.92
ABCF2	UniRef100_Q9UG63	YGLIGLNGIGKSMLLSAIGK	ATP Binding Site	26.88
ABCF3	UniRef100_Q9NUQ8	ICVVGENGAGKSTMLK	ATP Binding Site	5.45
ACACA	UniRef100_Q13085	DVDDGLQAAEEVGYPVMIKASEGGGGK	ATP Binding Site	6.21
ACACB	UniRef100_O00763	IGFPLMIKASEGGGGK	ATP Binding Site	-1.87
ACLY	UniRef100_P53396	GKLGLVGVNLTLDGVK	ATP Binding Site	-6.87
ACLY	UniRef100_P53396	LLQDHPWLLSQNLVVKPDQLIKR	ATP Binding Site	2.00
ACTA2, ACTB, ACTBL2, ACTC1, ACTG1	UniRef100_P68032, UniRef100_Q562R1, UniRef100_P63261, UniRef100_P60709, UniRef100_P62736	KYSVWIGGSILASLSTFQQMWISK	ATP Binding Site	-15.29
ACTR2	UniRef100_P61160	VVVCDNGTGFVKCGYAGSNFPEHIFPALVGRPIIR	ATP Binding Site	-16.82
ACTR2	UniRef100_P61160	KHMVFLGGAVLADIMK	ATP Binding Site	-2.20
ACTR3	UniRef100_P61158	DREVGIPPEQSLETAKAVK	ATP Binding Site	5.36
ACTR3	UniRef100_P61158	LPACVVDCGTGYTKLGYAGNTEPQFIIPSCIAIK	ATP Binding Site	-0.28
AFG3L2	UniRef100_Q9Y4W6	GAILTGPPGTGKTLLAK	ATP Binding Site	-4.85
AHCY	UniRef100_P23526	SKFDNLYGCR	ATP Binding Site	-10.85
AK1	UniRef100_P00568	TKIIFVVGGPGSGKGTQCEK	ATP Binding Site	-7.19
AK1	UniRef100_P00568	IIFVVGGPGSGKGTQCEK	ATP Binding Site	-9.87
AK2	UniRef100_P54819	AVLLGPPGAGKGTQAPR	ATP Binding Site	-4.75
AK3	UniRef100_Q9UIJ7, UniRef100_Q7Z4Y4	AVIMGAPGSGKGTVSSR	ATP Binding Site	19.58
AK4	UniRef100_P27144	AVILGPPGSGKGTVCQR	ATP Binding Site	-9.19

AK5	UniRef100_Q9Y6K8	IIFIIGGPGSGKGTQCEK	ATP Binding Site	2.21
AK7	UniRef100_Q96M32	ICILGPPAVGKSSIAK	ATP Binding Site	13.86
ALDH16A1	UniRef100_Q8IZ83	DSSGNLHGYVAEGGAKDIR	ATP Binding Site	-1.13
ALDH18A1	UniRef100_P54886	LIDIFYPGDQQSVTFGTKSR	ATP Binding Site	-6.95
APRT	UniRef100_P07741	GKLPGPTLWASYSLEYGK	ATP Binding Site	0.39
ASNA1	UniRef100_O43681	WIFVGGKGGVGK	ATP Binding Site	-3.04
ASNA1	UniRef100_O43681	HKIQAKYLDQMEDLYEDFHIVK	ATP Binding Site	0.73
ASS1	UniRef100_P00966	QHGIPIPVTPKNPWSMDENLMHISYEAGILENPK	ATP Binding Site	0.53
ATAD1	UniRef100_Q8NBU5	HVDLLEVAQETDGFSGSDLKEMCR	ATP Binding Site	15.67
ATG7	UniRef100_O95352	QPLYEFEDCLGGGKPKALAAADR	ATP Binding Site	-0.18
ATG7	UniRef100_O95352	FLLLTFADLKK	ATP Binding Site	-6.20
ATIC	UniRef100_P31939	KKNGNYCVLQMDQSYKPDENEVR	ATP Binding Site	4.08
ATP5B	UniRef100_P06576	IGLFGGAGVGKTVLIMELINNVAK	ATP Binding Site	-14.96
BAT1	UniRef100_Q13838	SGMGKTAVFVLATLQQLEPVTGQVSVLVMCHTR	ATP Binding Site	-9.58
BAT1, DDX39	UniRef100_Q13838, UniRef100_O00148	YQQFKDFQR	ATP Binding Site	-10.93
CCT2	UniRef100_P78371	GMDKILLSSGR	ATP Binding Site	-6.50
CCT3	UniRef100_P49368	ISIPVDISDSDMMLNIINSSITTKAISR	ATP Binding Site	10.09
CCT4	UniRef100_P50991	DALSDLALHFLNKMK	ATP Binding Site	11.95
CCT5	UniRef100_P48643	ISDSVLVDIKDTEPLIQTAKTTLGSK	ATP Binding Site	-2.48
CCT7	UniRef100_Q99832	GKATISNDGATILK	ATP Binding Site	10.91
CCT8	UniRef100_P50990	TSIMSKQYGNEVFLAK	ATP Binding Site	9.18
CHD8	UniRef100_Q9HCK8	LNTITPVVGKKRK	ATP Binding Site	-44.26
CLPB	UniRef100_Q9H078	RKENGWYDEEHPLVFLFLGSSGIGKTELAK	ATP Binding Site	-9.00
CLPX	UniRef100_O76031	SNILLLGPTGSGKTLLAQTLAK	ATP Binding Site	0.44
CMPK1	UniRef100_P30085	MKPLVVFVLGGPGAGKGTQCAR	ATP Binding Site	2.41
CNP	UniRef100_P09543	AIFTGYYGKGKPVPTQGSR	ATP Binding Site	-17.28
COASY	UniRef100_Q13057	SKLLPELLQPYTER	ATP Binding Site	-3.39
COASY	UniRef100_Q13057	MLGNLLRPPYERPELPTCLYVIGLTGISGSGKSSIAQR	ATP Binding Site	23.55
CPS1	UniRef100_P31327	IGSSMKSVGEVMAIGR	Other	1.16
DCTPP1	UniRef100_Q9H773	KYTELPHGAISEDQAVGPADIPCDSTGQTST	ATP Binding Site	12.74
DDX18	UniRef100_Q9NVP1	TGSGKTLAFLIPAVELIVK	ATP Binding Site	-5.33
DDX21	UniRef100_Q9NR30	TGTGKTFSFAIPLIEK	ATP Binding Site	3.05
DDX28	UniRef100_Q9NUL7	HVVCAAETGSGKTLSYLLPLLQR	ATP Binding Site	-5.30
DDX39	UniRef100_O00148	SGMGKTAVFVLATLQQIEPVNGQVTVLVMCHTR	ATP Binding Site	-8.90
DDX3X	UniRef100_O00571, UniRef100_F7BMH3	DLMACAQTGSGKTAAFLLPILSQIYSDGPGEALR	ATP Binding Site	11.22
DERA	UniRef100_Q9Y315	TVKKEWQAAWLLK	ATP Binding Site	6.01
DHX15	UniRef100_O43143	HQSFVLVGETGSGKTTQIPQWCVEYMR	ATP Binding Site	-5.22
DHX36	UniRef100_Q9H2U1	ELVNLIDNHQVTVISGETGCGKTTQVTQFILDNYIER	ATP Binding Site	-20.12
DYNC1H1	UniRef100_Q14204	LGGSPFGPAGTGKTESVK	ATP Binding Site	-1.99
DYNC1H1	UniRef100_Q14204	QPQGHLLLIGVSGAGKTTLSR	ATP Binding Site	0.38
ENPP1	UniRef100_P22413	TFPNHYSIVTGLYPESHGIIDNKMYDPK	ATP Binding Site	8.04
EPRS	UniRef100_P07814	WEFKHPQPFLR	ATP Binding Site	0.78
FDPS	UniRef100_P14324	IGTDIQDNKCSWLVVQCLQR	ATP Binding Site	29.13
GARS	UniRef100_P41250	TSGHVDKFADFMVK	ATP Binding Site	16.66
GART	UniRef100_P22102	ASGLAAGKGVIVAK	ATP Binding Site	-8.85

GART	UniRef100_P22102	SAGVQCFGPTAEAAQLESSKR	ATP Binding Site	-7.56
GART	UniRef100_P22102	SGCKVDLGGFAGLFDLK	ATP Binding Site	-2.13
GATB	UniRef100_O75879	IKQIQLEQDSGK	ATP Binding Site	-15.35
GATB	UniRef100_O75879	KHYFYADLPAGYQITQQR	ATP Binding Site	-4.32
GMPS	UniRef100_P49915	AELIKTHHNDTELIR	Other	-13.99
GMPS	UniRef100_P49915	LGIQVKVINAAHSFYNGTTTLPISDEDRTPR	Other	14.54
GSS	UniRef100_P48637	CPDIATQLAGTKK	ATP Binding Site	-5.02
GSS	UniRef100_P48637	TKAIEHADGGVAAGVAVLDNPYPV	ATP Binding Site	7.54
HARS	UniRef100_P12081	TICSSVDKLDKVSWEEVKNEMVGEK	ATP Binding Site	4.68
HDDC3	UniRef100_Q8N4P3	RKDPEGTPYINHPIGVAR	ATP Binding Site	1.23
HDDC3	UniRef100_Q8N4P3	LVEEVTDDKTLPKLER	ATP Binding Site	17.25
HNRNPU	UniRef100_Q00839	KDCEVVMMIGLPGAGKTTWVTK	ATP Binding Site	6.85
HPRT1	UniRef100_Q6LET3, UniRef100_P00492	LKSYCNDQSTGDIK	ATP Binding Site	12.92
HSP60	UniRef100_P10809	TVIIEQSWGSPKVTK	ATP Binding Site	11.39
HSP90AA	UniRef100_P07900	TLTIVDTGIGMTKADLINNLGTIAKSGTK	ATP Binding Site	-1.29
HSP90AA, HSP90AA2, HSP90AB1	UniRef100_Q14568, UniRef100_P08238, UniRef100_P07900	ADLINNLGTIAKSGTK	ATP Binding Site	-5.50
HSP90AB1	UniRef100_P08238	TLTLVDTGIGMTKADLINNLGTIAKSGTK	ATP Binding Site	-3.22
HSP90AB1, HSP90AB3P	UniRef100_P08238, UniRef100_Q58FF7	RAPFDLFENKKK	ATP Binding Site	-16.94
HSP90B2P, TRA1	UniRef100_P14625, UniRef100_Q58FF3	GLFDEYGSKK	ATP Binding Site	-6.72
HSPA1A	UniRef100_P08107	LIGDAAKNQVALNPQNTVFDAKR	ATP Binding Site	-9.44
HSPA1A	UniRef100_P08107	LIGDAAKNQVALNPQNTVFDAK	ATP Binding Site	-15.23
HSPA2	UniRef100_P54652	LIGDAAKNQVAMNPTNTIFDAKR	ATP Binding Site	-1.50
HSPA2	UniRef100_P54652	LIGDAAKNQVAMNPTNTIFDAK	ATP Binding Site	-5.18
HSPA5	UniRef100_P11021	LIGDAAKNQLTSNPENTVFDAKR	ATP Binding Site	-16.08
HSPA5	UniRef100_P11021	LIGDAAKNQLTSNPENTVFDAK	ATP Binding Site	-7.84
HSPA8	UniRef100_P11142	LIGDAAKNQVAMNPTNTVFDAKR	ATP Binding Site	3.27
HSPA8	UniRef100_P11142	LIGDAAKNQVAMNPTNTVFDAK	ATP Binding Site	4.45
HSPA9	UniRef100_P38646	LVGMPAKR	ATP Binding Site	-4.09
HYOU1	UniRef100_Q9Y4L1	RKTPVIVTLKENER	ATP Binding Site	-13.34
HYOU1	UniRef100_Q9Y4L1	KTPVIVTLKENER	ATP Binding Site	-6.78
IDI1	UniRef100_Q13907	QQVQLLAEMCILIDENDNKIGAETKK	ATP Binding Site	5.48
KARS	UniRef100_Q15046	KEICNAYTELNDPMR	ATP Binding Site	2.22
KIAA0564	UniRef100_A3KMH1	LGHILVVDEADKAPTNVTCILKTLVENGEMILADGRR	ATP Binding Site	11.07
LIG1	UniRef100_P18858	VREDKQPEQATTSAQVACLYR	ATP Binding Site	-7.76
LONP1	UniRef100_P36776	ILCFYGPPGVGKTSIAR	Other	1.81
MCCC1	UniRef100_Q96RQ3	HQKIIEEAPAPGIK	ATP Binding Site	-6.46
MCCC1	UniRef100_Q96RQ3	IGYPVMIKAVR	ATP Binding Site	4.45
MCM4	UniRef100_P33991	SLFSDKQMIK	ATP Binding Site	4.98
MCM6	UniRef100_Q14566	SQFLKHVEEFSPR	ATP Binding Site	-5.23
MCM6	UniRef100_Q14566	GDINVCIVGDPSTAKSQFLK	ATP Binding Site	-2.54
MDN1	UniRef100_Q9NU22	VVSAGTYPVLIQGETSVGKTSLIQWLAAATGNHCVR	ATP Binding Site	3.28
ME2	UniRef100_P23368	SIVDNWPENHVKAVVVTDGER	ATP Binding Site	-6.47

ME2	UniRef100_P23368	AKIDSYQEPFTHSAPESIPDTFEDAVNILKPSTIIGVAGAGR	ATP Binding Site	-16.71
MMAB	UniRef100_Q96EY8	RPKDDQVFEAVGTTDELSSAIGFALELVTEK	ATP Binding Site	-4.08
MTHFD1	UniRef100_P11586	YVVVTGITPTPLGEGKSTTTIGLVQALGAHLYQNVFACVR	ATP Binding Site	-6.16
MTHFD1L	UniRef100_Q6UB35, UniRef100_Q5JYA8	YVLVAGITPTPLGEGKSTVTIGLVQALTAHLNVNSFACLR	ATP Binding Site	1.16
MVK	UniRef100_Q03426	GLHSKLTGAGGGGCGITLLKPGLEQPEVEATK	ATP Binding Site	15.38
MYO1E	UniRef100_Q12965	NMIIDRENQCVIISGESGAGKTVAAK	ATP Binding Site	4.66
NADK2	UniRef100_Q4G0N4	VVVVAKTTR	ATP Binding Site	-11.03
NADSYN1	UniRef100_Q6IA69	YDCSSADINPIGGISKTDLR	ATP Binding Site	-2.19
NARS	UniRef100_O43776	FPVEIKSFYMQR	ATP Binding Site	2.36
NDUFA10	UniRef100_O95299	VITVDGNICTGKGK	ATP Binding Site	14.09
NME1, NME2	UniRef100_P15531, UniRef100_P22392	TFIAIKPDGVQR	ATP Binding Site	-1.52
NME3	UniRef100_Q13232	GDFCIEVGKNLIHGSDSVESAR	ATP Binding Site	1.91
NMNAT3	UniRef100_Q96T66	DHLHQTGMYQVIQGIISPVNDTYGKK	ATP Binding Site	9.62
NOP2	UniRef100_P46087	VLLDAPCSGTGVISKDPAVK	ATP Binding Site	1.98
NRK1	UniRef100_Q9NWW6	TFIIGISGVTNSGKTTLAK	ATP Binding Site	0.34
NSF	UniRef100_P46459	VWIGIKK	ATP Binding Site	6.03
NSF	UniRef100_P46459	GILLYGPPGCGKTLLAR	ATP Binding Site	-6.18
NT5E	UniRef100_P21589, UniRef100_Q53Z63	GVDVVVGGHSNTFLYTGNPPSKEVPAGKYPFIVTSDDGR	ATP Binding Site	-9.95
NTPCR	UniRef100_Q9BSD7	HVFLTGPPGVGKTTLIHK	ATP Binding Site	-14.99
NUDT1	UniRef100_P36639	VLLGMKK	ATP Binding Site	25.70
NUDT1	UniRef100_P36639	WNGFGGKVQEGETIEDGAR	ATP Binding Site	22.17
NUDT1	UniRef100_P36639	LYTLVLVLQPQRVLLGMKK	ATP Binding Site	18.32
NUDT2	UniRef100_P50583	NKPKTVIYWLAEVKDYDVEIR	ATP Binding Site	19.18
NUDT2	UniRef100_P50583	VDNNAIEFLLLQASDGIHHWTPPKGHVEPGEDDLETALR	ATP Binding Site	11.64
NUDT7	UniRef100_P0C024	APGEVCFPGGKRDPTDMDDAATALR	ATP Binding Site	19.75
NVL	UniRef100_O15381	ALGLVTPAGVLLAGPPGCGKTLLAK	ATP Binding Site	-1.13
NVL	UniRef100_O15381	GVLLHGPPGCGKTLLAHAIAGELDLPILK	ATP Binding Site	-8.26
OLA1	UniRef100_Q9NTK5	IGIVGLPNVGKSTFFNVLTNSQASAENFPFCTIDPNESR	ATP Binding Site	-0.68
PAICS	UniRef100_P22234	TKEVYELLDSPGK	ATP Binding Site	19.51
PC	UniRef100_P11498	HQKVVEIAPAAHLDPQLR	ATP Binding Site	-15.19
PCCA	UniRef100_P05165	EIGYPVMIKASAGGGGK	ATP Binding Site	-5.50
PCCA	UniRef100_P05165	NQKVVEEAPSIFLDAETRR	ATP Binding Site	-10.70
PDE12	UniRef100_Q6L8Q7	IKQHEGLATFYR	ATP Binding Site	-5.87
PEX1	UniRef100_O43933	NGALLLTGGKGSGK	ATP Binding Site	-4.27
PFAS	UniRef100_O15067	HWFFKGQLHVDGQK	ATP Binding Site	-4.58
PFKFB2	UniRef100_O60825	VFFVESVCDDPDVIAANILEVKVSSPDYPER	ATP Binding Site	14.74
PFKM	UniRef100_P08237	SFMNNWEVYKLLAHVRPPVSK	ATP Binding Site	-8.93
PGK1	UniRef100_P00558	ALESPERPFLAILGGAKVADK	ATP Binding Site	-4.49
PKM, PKM2	UniRef100_P14618, UniRef100_Q504U3	AEGSDVANAVLDGADCIMLSGETAKGDYPLEAVR	ATP Binding Site	28.24
PMS2	UniRef100_P54278	HHTSKIQEFADLTQVETFGFRGEALSSLCALSDVTISTCHASAK	ATP Binding Site	3.36
PMVK	UniRef100_Q15126	SGKDFVTEALQSR	ATP Binding Site	-5.60
POLR3A	UniRef100_O14802	MAQELKYGDIVER	ATP Binding Site	4.31

PPCS	UniRef100_Q9HAB8	MVPKLLSPLVK	ATP Binding Site	-7.44
PPCS	UniRef100_Q9HAB8	AFIISFKLETDPAIVINR	ATP Binding Site	-9.61
PRKAG1	UniRef100_P54619	LPVIDPESGNTLYILTHKR	ATP Binding Site	-11.56
PRKAG1	UniRef100_P54619	GRVVDIYSKFDVINLAAEK	ATP Binding Site	-7.08
PRKAG1, PRKAG2	UniRef100_P54619, UniRef100_Q9UGJ0	VVDIYSKFDVINLAAEK	ATP Binding Site	-7.97
PRKAG2	UniRef100_Q9UGJ0	ISALPVVDESGKVVDIYSKFDVINLAAEK	ATP Binding Site	-22.54
PRPS1	UniRef100_P60891, UniRef100_Q53FW2	NCTIVSPDAGGAKR	ATP Binding Site	-22.26
PRPS1L1, PRPS2	UniRef100_P21108, UniRef100_P11908	NCIIVSPDAGGAKR	ATP Binding Site	-13.63
PSMC1	UniRef100_P62191	GVILYGPPGTGKTLLAK	ATP Binding Site	-7.42
PSMC2	UniRef100_P35998	GVLLFGPPGTGKTLCAR	ATP Binding Site	-6.44
PSMC3	UniRef100_P17980	GVLMYGPPGTGKTLLAR	ATP Binding Site	5.71
PSMC4	UniRef100_P43686	GVLMYGPPGCGKTMLAK	ATP Binding Site	13.36
PSMC5	UniRef100_P62195	GVLLYGPPGTGKTLLAR	ATP Binding Site	-3.98
PSMC6	UniRef100_P62333	GCLLYGPPGTGKTLLAR	ATP Binding Site	-0.83
PSMD9	UniRef100_O00233	HNIICLQNDHKAVMK	ATP Binding Site	2.13
QARS	UniRef100_P47897	TGDKWCIYPTYDYTHCLCDSIEHITHSLCTKEFQAR	ATP Binding Site	-7.77
RAD17	UniRef100_O75943	QGGSILLITGPPGCGKTTTLK	ATP Binding Site	15.62
RBKS	UniRef100_Q9H477	FFIGFGGKGANQCVQAAR	ATP Binding Site	-1.64
RFC1	UniRef100_P35251	AALLSGPPGVGKTTTASLVCQELGYSYVELNASDTR	ATP Binding Site	-12.52
RFC2	UniRef100_P35250	EGNVPNIIIAGPPGTGKTTSILCLAR	ATP Binding Site	1.52
RFC4	UniRef100_P35249	SLEGADLPNLLFYGPPGTGKTSTILAAAR	ATP Binding Site	-6.66
RFC5	UniRef100_P40937	FINEDRLPHLLLYGPPGTGKTSTILACAK	ATP Binding Site	2.11
RFK	UniRef100_Q969G6	GSKQLGIPTANFPEQVVDNLPADISTGIYYGWASVGSGDVHK	ATP Binding Site	10.06
RUVBL1	UniRef100_Q9Y265	AVLLAGPPGTGKTALALAIAQELGSK	ATP Binding Site	-15.57
RUVBL2	UniRef100_Q9Y230	AVLIAGQPGTGKTAIAMGMAQALGPDTPFTAIAGSEIFSLEMSK	ATP Binding Site	-0.97
SARS	UniRef100_P49591, UniRef100_Q53HA4	KLDLEAWFPGSGAFR	ATP Binding Site	3.57
SKIV2L	UniRef100_Q15477	HDSVFVAAHTSAGKTVVAEYAIALAQK	ATP Binding Site	-3.49
SLC25A24	UniRef100_Q6NUK1	LAVGKTGQYSGIYDCAK	ATP Binding Site	11.88
SMC1A	UniRef100_Q14683	FTAIIGPNGSGKSNLMDAISFVLGEK	ATP Binding Site	5.67
SMC3	UniRef100_Q9UQE7	NGSGKSNFFYAIQFVLSDEFSHLRPEQR	ATP Binding Site	-10.19
SMC4	UniRef100_Q9NTJ3	LMITHIVNQNFKSYAGEK	ATP Binding Site	-7.11
SNRNP200	UniRef100_O75643	LATYGITVAELTGDHQLCKEEISATQIIVCTPEKWDIITR	ATP Binding Site	-14.27
SPG7	UniRef100_Q9UQ90	GALLLGPPGCGKTLLAK	ATP Binding Site	0.12
SUCLA2	UniRef100_Q9P2R7	GKGTFESGLK	ATP Binding Site	-0.65
SUCLA2	UniRef100_Q9P2R7	DVVIKAQVLAGGR	ATP Binding Site	9.97
TCP1	UniRef100_P17987	VLCELADLQDKEVGDGTTSVVIIAAELLK	ATP Binding Site	6.76
TK2	UniRef100_O00142	TTCLEFFSNATDVEVLTEPVSKWR	ATP Binding Site	14.43
TOP2A, TOP2B	UniRef100_Q02880, UniRef100_P11388	KVTGGRNGYGAK	ATP Binding Site	11.93
TOR1A	UniRef100_O14656	KPLTLSLHGWTGTGKNFVSK	ATP Binding Site	4.27
TOR1B	UniRef100_O14657	KPLTLSLHGWAGTGKNFVSQIVAENLHPK	ATP Binding Site	2.00
TOR2A, TOR2X	UniRef100_Q8N2E6, UniRef100_Q5JU69	AFVRDPAPTKPLVLSLHGWTGTGKSYVSSLLAHYLFQGGLR	ATP Binding Site	0.38

TOR3A	UniRef100_Q9H497, UniRef100_Q5W0C6	ALALSFHGWSGTGKNFVAR	ATP Binding Site	6.55
TOR4A	UniRef100_Q9NXH8	DYLATHVHSRPLLLALHGPSGVGKSHVGR	ATP Binding Site	5.38
TRA1	UniRef100_P14625	NLGTIAKSGTSEFLNK	ATP Binding Site	-8.56
TRAP1	UniRef100_Q12931	SGSKAFLDALQNQAEASSK	ATP Binding Site	-10.78
TRAP1	UniRef100_Q12931	VLIQTKATDILPK	ATP Binding Site	-11.57
TRMU	UniRef100_O75648	TPNPDIVCNKHIK	ATP Binding Site	-13.98
TRMU	UniRef100_O75648	LLQAADSFKDQTFFLSQVSQDALRR	ATP Binding Site	-2.57
TTL	UniRef100_Q8NG68	KKEDGEGNVWIAKSSAGAK	ATP Binding Site	10.59
TTL	UniRef100_Q8NG68	SSAGAKGEGILISSEASELLDFIDNQGQVHVIQK	ATP Binding Site	-14.46
TTLL12	UniRef100_Q14166	WGEDNHWICKPWNLAR	ATP Binding Site	-5.29
TTLL12	UniRef100_Q14166	LSQERPGVLLNQFPCENLLTVKDCLASIAR	ATP Binding Site	-17.65
UBA1	UniRef100_P22314	GNVQVVIPFLTESYSSSQDPPEKSIPICTLK	ATP Binding Site	-4.55
UBA2	UniRef100_Q9UBT2	VHLAEKGDGAELIWDKDDPSAMDFVTSAANLR	ATP Binding Site	0.55
UBA2	UniRef100_Q9UBT2	GDGAELIWDKDDPSAMDFVTSAANLR	ATP Binding Site	7.64
UBA3	UniRef100_Q8TBC4	DIGRPKAEVAAEFLNDRVPNCNVVPHFNK	ATP Binding Site	-11.62
UBA5	UniRef100_Q9GZZ9	LFFQPHQAGLSKVQAAEHTLR	ATP Binding Site	-12.85
UBA6	UniRef100_A0AVT1	GMITVTDPDLIEKSNLNR	ATP Binding Site	3.60
UPF1	UniRef100_Q92900	TVLQRPLSLIQGPPGTGKTVTSATIVYHLAR	ATP Binding Site	-1.93
UPF1	UniRef100_Q92900	QGNGPVLVCAPSNIAVDQLTEKIHQTGLK	ATP Binding Site	-3.51
VCP	UniRef100_Q0IIN5, UniRef100_P55072	GILLYGPPGTGKTLIAR	ATP Binding Site	-8.02
VCP	UniRef100_Q0IIN5, UniRef100_P55072	GVLFYGPPGCGKTLLAK	ATP Binding Site	-2.36
VCP	UniRef100_Q0IIN5, UniRef100_P55072	TLLAKAIANECQANFISIK	ATP Binding Site	-7.20
VCP	UniRef100_Q0IIN5, UniRef100_P55072	IVSQLLTLMDGLKQR	ATP Binding Site	7.80
VPS4A, VPS4B	UniRef100_O75351, UniRef100_Q9UN37	GILLFGPPGTGKSYLAK	ATP Binding Site	-2.55
XRCC3	UniRef100_O43542	SSAGKTQLALQLCLAVQFPR	ATP Binding Site	-4.81
XRCC5	UniRef100_P13010	FFMGNQVLKVFAAR	ATP Binding Site	2.24
XRCC6	UniRef100_P12956	IQVTPPGFQLVFLPFADDKR	ATP Binding Site	10.61
YME1L1	UniRef100_Q96TA2	GILLVGPPGTGKTLLAR	ATP Binding Site	-10.37

Figures

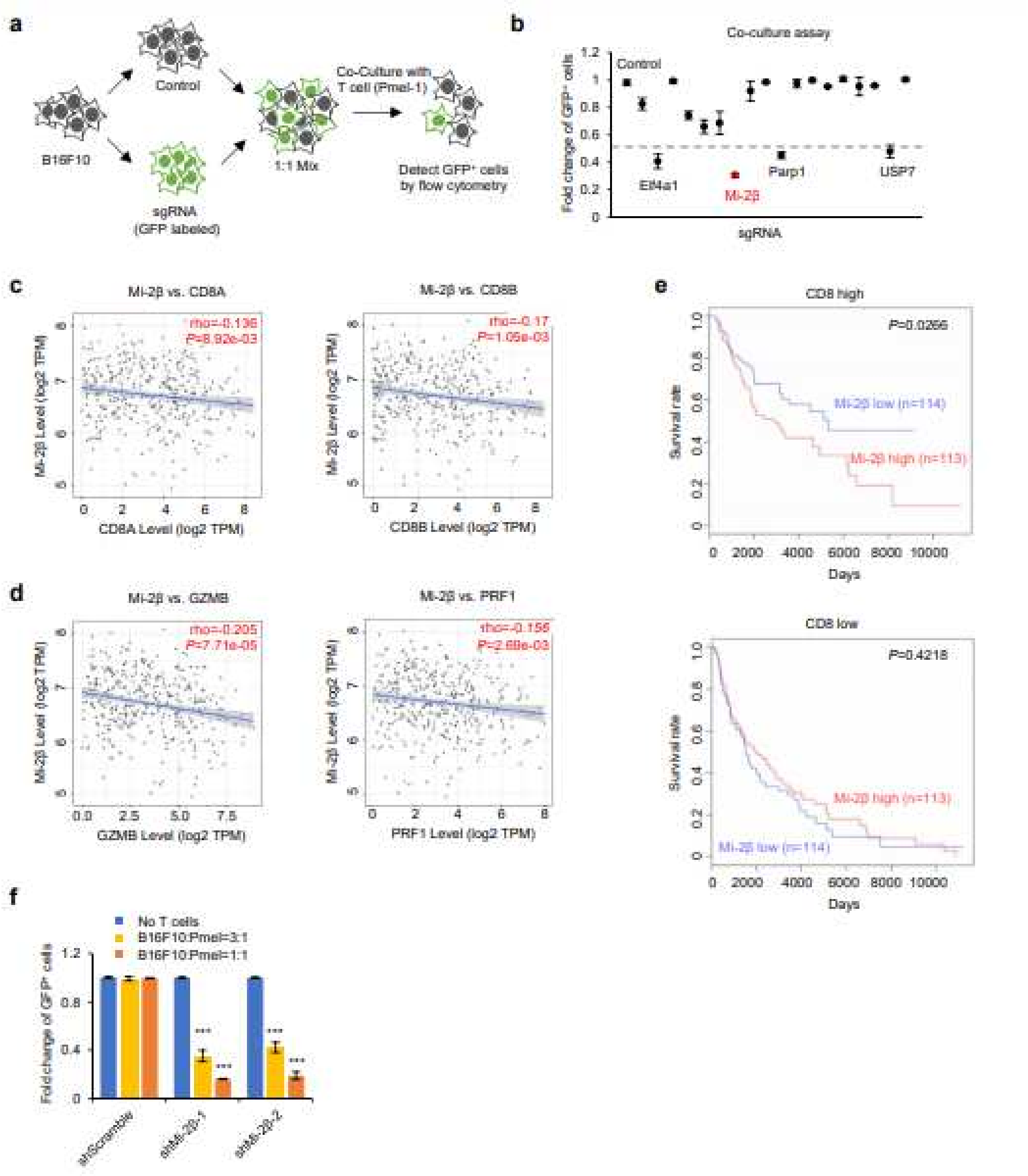

Figure 1

Identification of Mi-2β regulating melanoma cell resistance to T cell-mediated killing. a, A schematic for co-culture assay. GFP-labelled B16F10 cells with target gene knockout were mixed with non-labelled control cell at a 1:1 ratio, which were then co-cultured with activated Pmel-1 T cells (at a ratio of 1:1) for 3 days. Survival GFP positive tumor cells were assayed with flow cytometry. b, Targeted genes for overcoming resistance to Pmel-1 T cell killing. Targeted genes were plotted based on the survival change of knockout tumor cells compared with control cells. The dash line represents survival ratio changes for 0.5 fold. c, Analysis of correlation between Mi-2β mRNA level and CD8A or CD8B as T cell infiltration markers in TCGA SKCM-Metastasis (n=368). Plots show the Spearman's correlation. d, Analysis of correlation between Mi-2β mRNA level and GZMB or PRF1 level as cytotoxicity markers. Analysis was performed as indicated in (c). e, The survival curve of melanoma patients with different Mi2β mRNA level.

All patients in TCGA melanoma were divided into CD8 high or CD8 low groups based on the median expression. The available patients were further split into high- or low-expressing groups according to the median of Mi-2β mRNA level expression. Kaplan-Meier survival curves were shown, with the difference was examined using a log-rank test. f, GFP-labelled Mi-2β knockdown or shScramble B16F10 cells mixed with non-labelled B16F10 parental cells, and then were co-cultured with activated Pmel-1 T cells as indicated ratio for three days. The fold changes of the survival GFP-positive tumor cell were assayed with flow cytometry. Values represent mean ± SD *** P < 0.001.

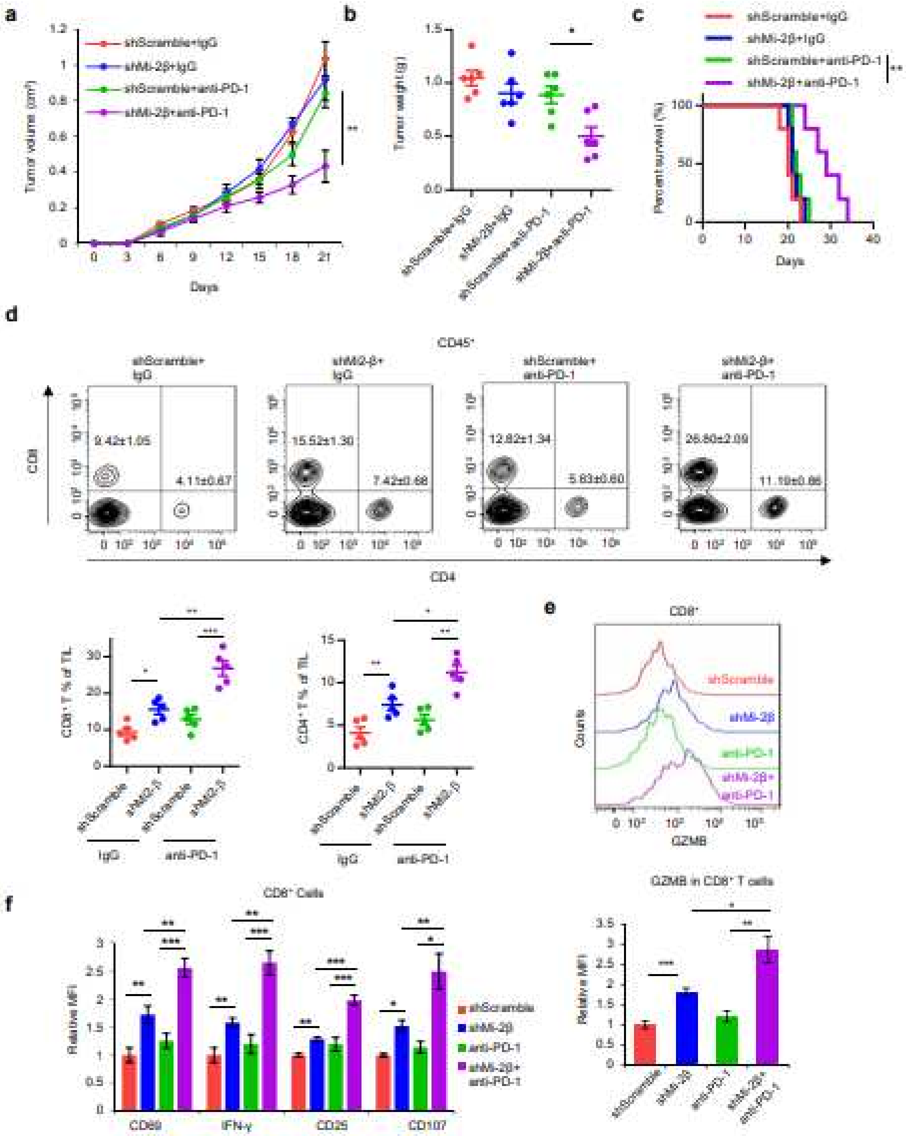

Figure 2

Mi-2β silencing improved the response to the anti-PD-1 therapy a-c, Mice bearing Mi-2β knockdown or shScramble B16F10 cells were treated with i.p. injection of control IgG (10mg/kg) or anti-PD-1 (10mg/kg) antibodies at day 6, 9, 12, 15 and 18 after tumor cell inoculation, tumor volume (a), tumor weight (b) and mouse survival (c) were measured. Each group n=5. Tumor-infiltrating lymph cells in graft tumor were measured by flow cytometry. d, The population of CD8+ and CD4+ T cells were gated within CD45+ T cells. e, The Granzyme B expression in CD8+ T was measured and quantified with flow cytometry. f, Expression of activation markers of CD8+ T cells were measured by flow cytometry assay. MFI represents mean fluorescence intensity. Log-rank test was used to determine statistical significance of P value for mouse Kaplan-Meier survival curves. Values represent mean ± SEM. *P < 0.05, **P < 0.01, *** P < 0.001.

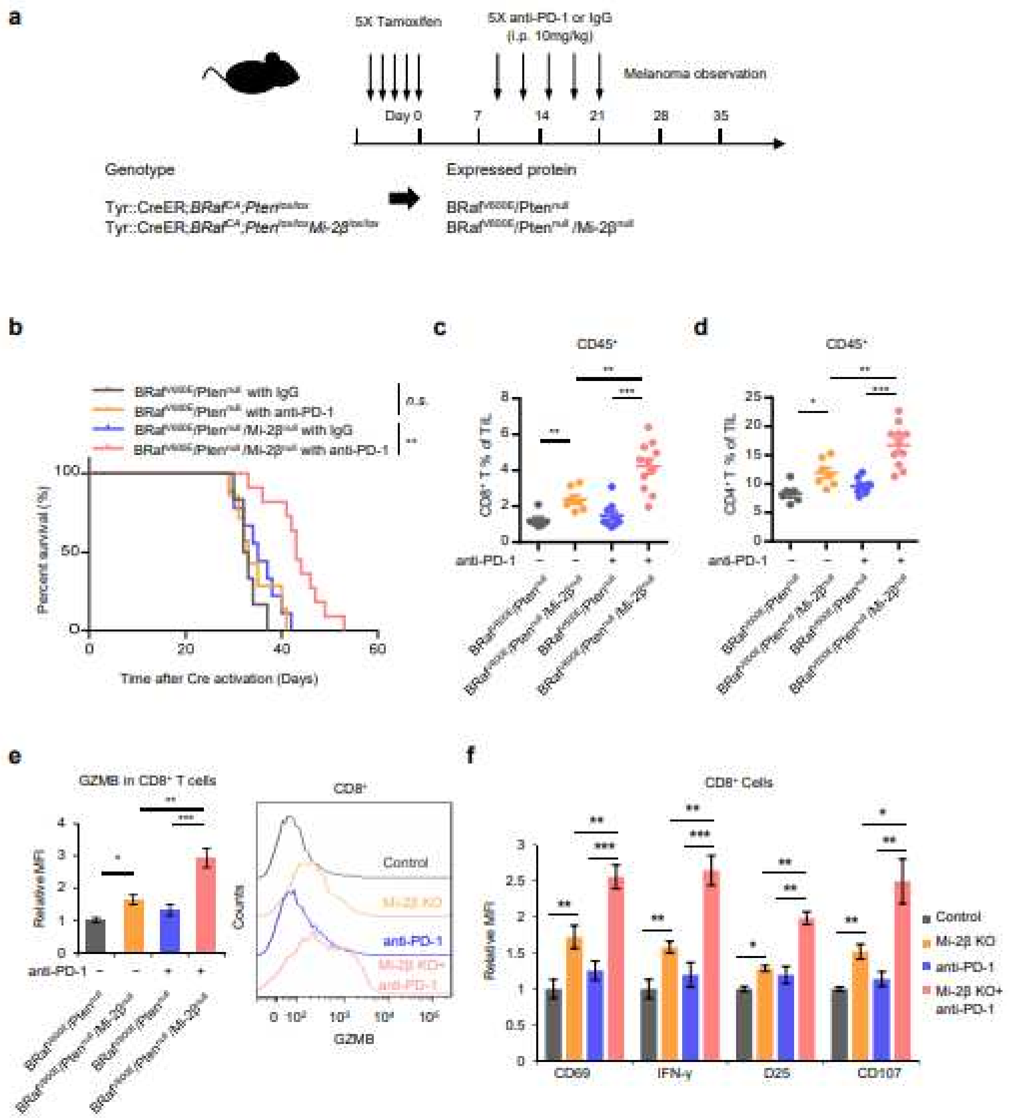

Figure 3

Mi-2β deficiency induces responses to anti-PD-1 treatment for melanoma in vivo a, A schematic for experimental strategy with anti-PD-1 treatment on genetically engineered melanoma mouse model. Mice carrying conditional alleles of Tyr::CreER;BRafCA;Ptenlox/lox or Tyr::CreER;BRafCA;Ptenlox/loxMi-2βlox/lox were administered with tamoxifen for constant 5 days to activate CreER to cause melanocyte-specific conversion of BrafCA to BrafV600E, and the conversion of the Ptenlox/lox and Mi-2βlox/lox alleles to null alleles, which expressed proteins of BRafV600E/Ptennull or BRafV600E/Ptennull /Mi-2βnull, respectively. Mice with measurable tumors were randomly treated with either control IgG (10mg/kg) or anti-PD-1 (10mg/kg) antibodies by i.p. administration at day 9, 12, 15, 18 and 21 after Cre activation. b, Mouse survival of BRafV600E/Ptennull mice treated with IgG (n=6) or anti-PD-1 (n=7), and of BRafV600E/Ptennull /Mi-2βnull mice treated with IgG (n=9) or anti-PD-1 (n=11). Log-rank test was used for P value calculation. c-d, TILs were assayed with flow cytometry assay for the population of CD8+ cells (c) and CD4+ T cells (d) gated within CD45+ T cells. e, Granzyme B expression in CD8+ T was determined and quantified with flow cytometry. f, Expression of activation markers on CD8+ T cells were determined with flow cytometry assay. MFI represents mean fluorescence intensity. Values represent mean ± SEM. *P < 0.05, **P < 0.01, *** P < 0.001.

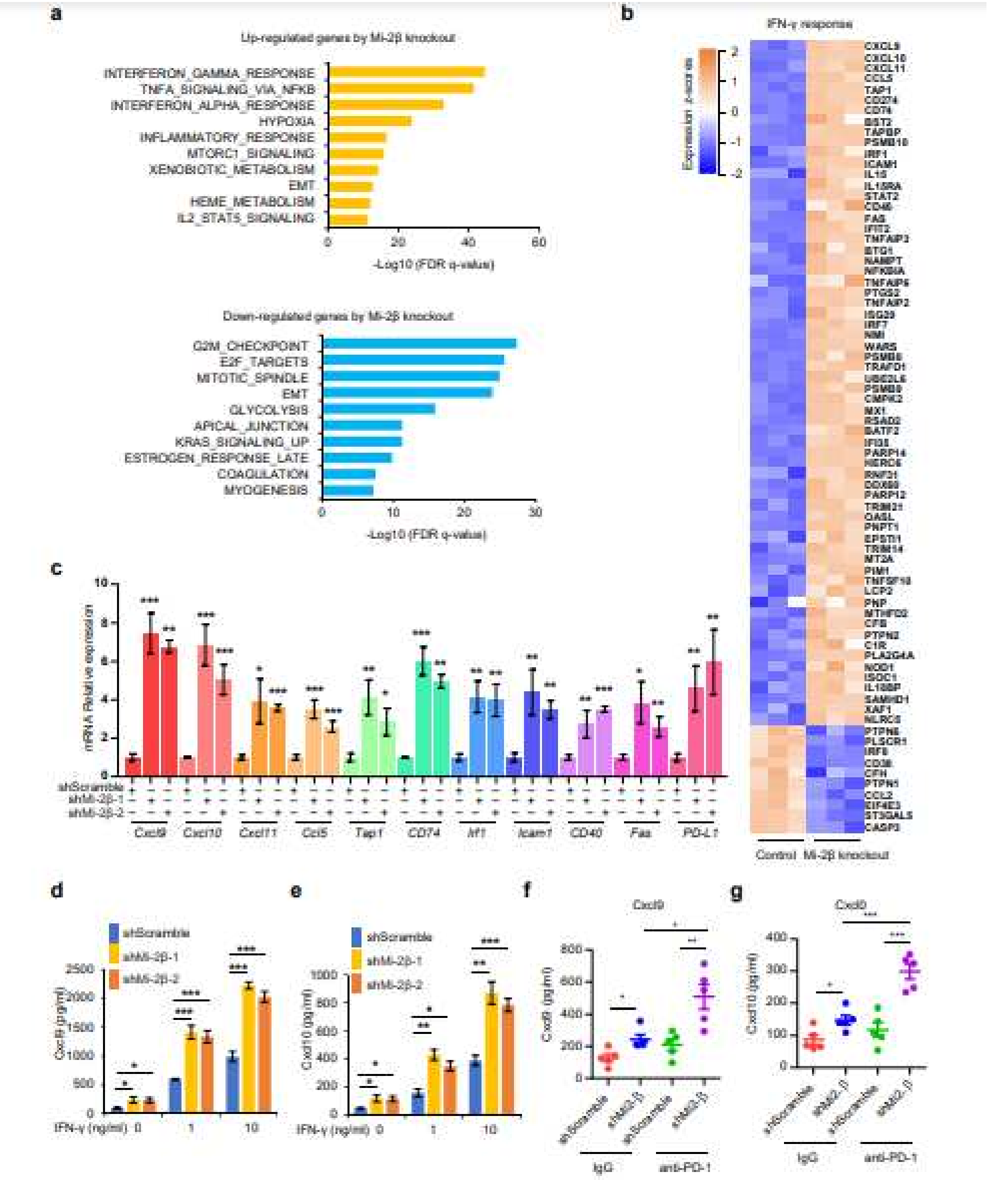

Figure 4

The enhanced IFN-γ signaling by Mi-2β knockout in melanoma a, Microarray data analyzed for hallmark gene sets enriched for upregulated or downregulated mRNA in Mi-2β knockout and control B16F10 cells treated with IFN-γ for 24 hours. b, Heat map showing expression value (z-score expression) of IFN-γ signaling genes in control and Mi-2β knockout B16F10 cells in microarray data. c, The expressions of Mi-2β-regulated IFN-γ signaling genes were measured in IFN-γ-stimulated B16F10 cells with Mi-2β silencing by RT-qPCR. Values represent mean ± SD. d-e, The amount of secret Cxcl9 (d) or Cxcl10 (e) were measured in IFN-γ (0, 1, or 10 ng/mL, for 24 hours)- stimulated B16F10 cells with Mi-2β silencing by

ELISA assay. Values represent mean ± SD. f-g, The graft melanomas were isolated to be cultured in PBS with the same amount cells for 4 hours (n=5), and then the secreted amount of the chemokines Cxcl9 (f) and Cxcl10 (g) in the culture medium were measured by ELISA assays. Values represent mean ± SEM. *P < 0.05, **P < 0.01, *** P < 0.001.

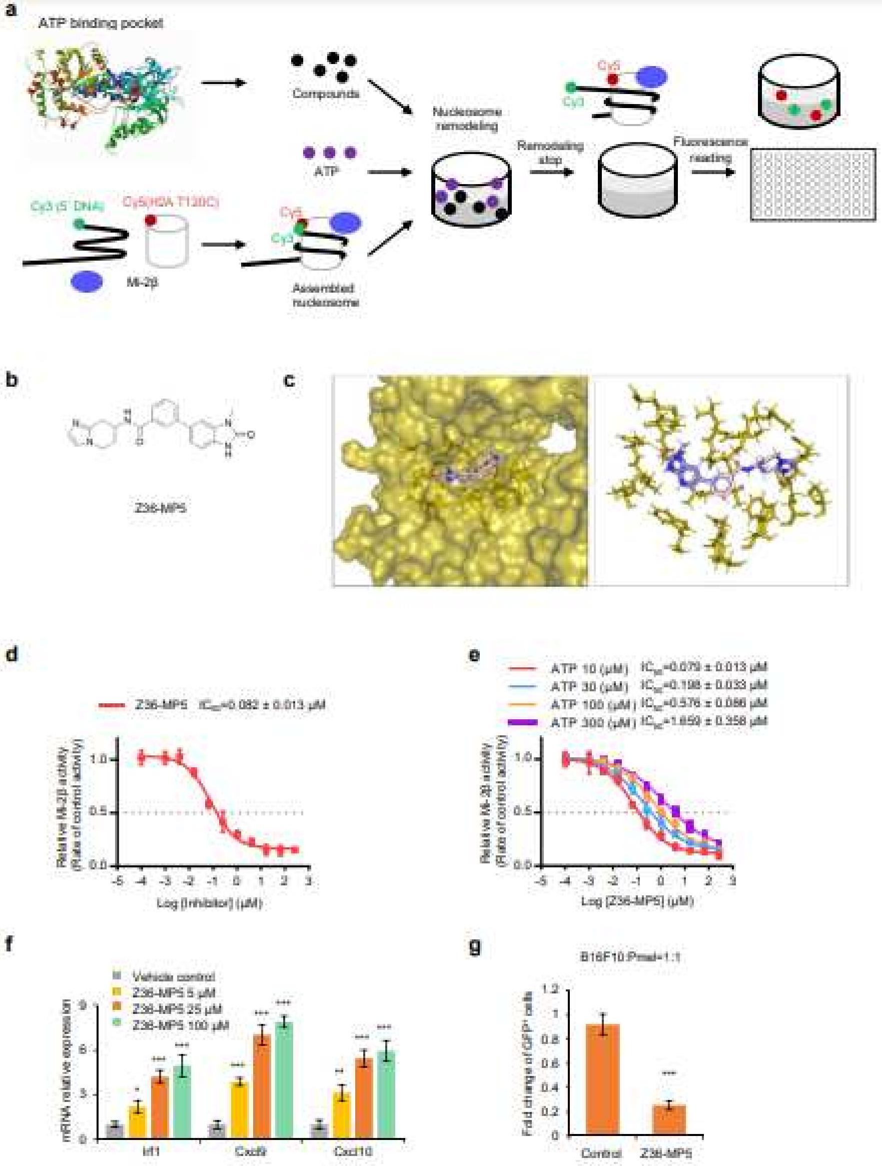

Figure 5

Z36-MP5 was developed as a selective Mi-2β inhibitor a, Schematic representing in vitro screen assay for testing Mi-2β chromatin modulatory activity using FRET-based nucleosome repositioning assay. b, The chemical structure of Z36-MP5. c, Orientations of Z36-MP5 to homologized Mi-2β. Z36-MP5 was docked into the ATP binding pocket of homologized Mi2β. The methyl group of Z36-MP5 extended to a solvent-exposed channel lined with the side chains of Tyr729, Leu755, Met966, and Ile1163, with generating H-bonds via the O atom of keto group with His727, O atom of amide group with Gly756, and protonated N atom of imidazole group with Asp873. The atoms of Z36-MP5 were colored as follows: carbon pink, oxygen red, nitrogen blue, and hydrogen white. The H-bonds between Z36-MP5 and homologized Mi-2β were shown as light-yellow dash lines. d, The inhibitory activity of Z36-MP5 for Mi-2β chromatin modulatory activity, measured as fold changes of Mi2β activity treated with control vehicle. Data, including IC50, presents as means ± SD. e, The inhibitory activity of Z36-MP5 with IC50 values against Mi-2β at different ATP concentrations. Data are presented means ± SD. f, The expression of Cxcl9, Cxcl10 and Irf1 mRNA in B16F10 cells treated with Z36-MP5 as indicated concentration for 24 hours was determined with RT-qPCR assay. g, Z36-MP5-treated (25 μM) GFP-labelled B16F10 cells were pretreated with 10ng/ml of IFN-γ for 24 hours, before co-culture with activated Pmel-1 T cells at a ratio of 1:1 for three days. The fold changes of survival GFP-positive tumor cells were assayed with flow cytometry. Values represent mean ± SD *P < 0.05, **P < 0.01, *** P < 0.001.

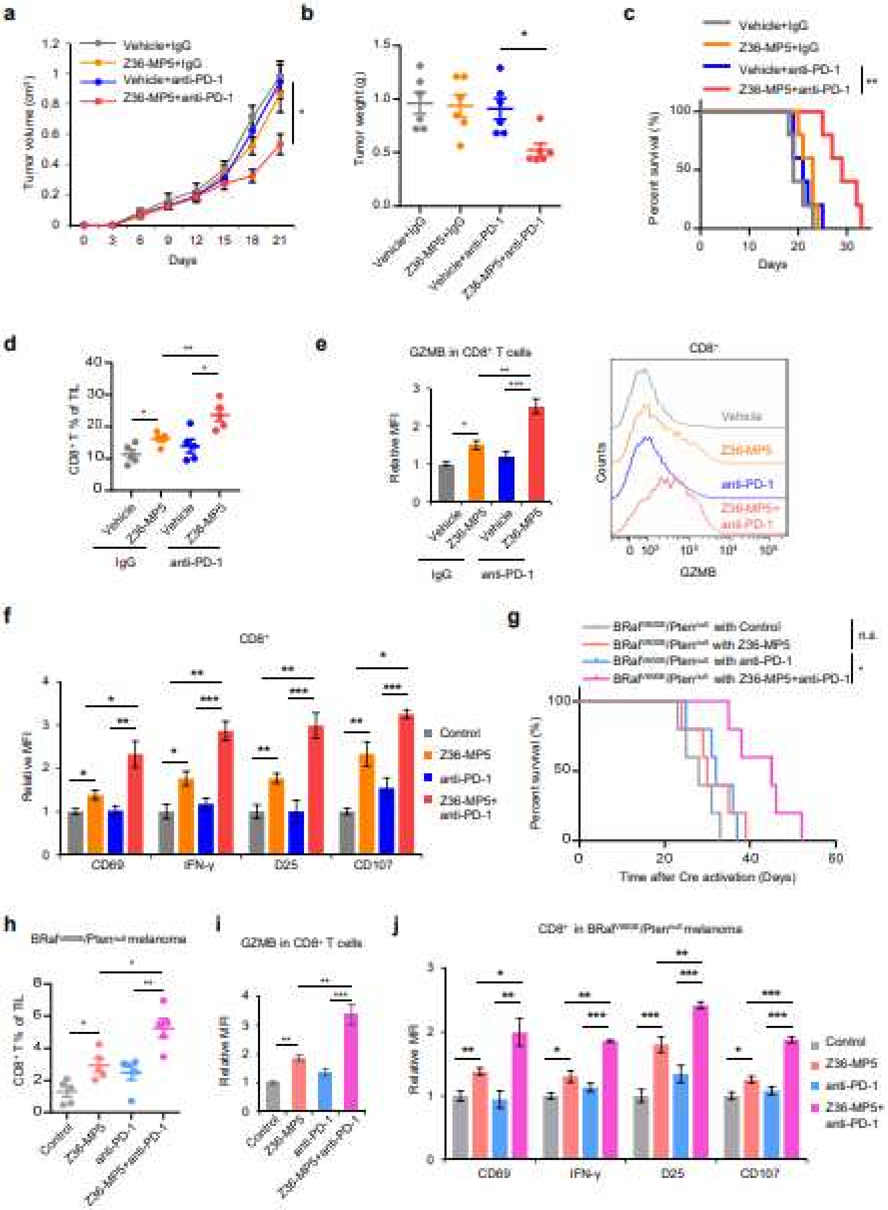

Figure 6

Combinational treatment with Z36-MP5 and anti-PD-1 antibodies suppressed cold melanoma growth Mice bearing B16F10 cells were treated with control IgG or anti-PD-1 antibody, and vehicle control or Z36-

MP5, as indicated. a-b, Tumor volume (a), and tumor weight (b) were measured. For each group n=5. c, Survival curve of mice with B16F10 cell grafts treated with control IgG or anti-PD-1 antibody, and vehicle control or Z36-MP5 as indicated was shown, with log-rank test for P value. d, Tumorinfiltrating lymph cells in tumor graft of each group mice were measured by flow cytometry. The population of CD8+ was gated within CD45+ T cells (Percentage of mean ± SEM). e, Granzyme B expression in CD8+ T was determined and quantified. f, Expression of activation markers on CD8+ T cells were determined with flow cytometry assay. MFI, mean fluorescence intensity. g, Mice carrying conditional alleles of Tyr::CreER;BRafCA;Ptenlox/lox were administered with tamoxifen for constant 5 days to activate CreER to cause melanocyte-specific conversion of BrafCA to BrafV600E, and the conversion of the Ptenlox/lox alleles to null, which express proteins of BRafV600E/Ptennull. Mice with measurable tumors were randomly treated with either control IgG (10mg/kg) or anti-PD-1 antibodies (10mg/kg) and/or Z36- MP5 (30mg/kg/day) by i.p. administration as indicated. For each group n=5. Mouse survival was shown with log-rank test for p value. h-j, Tumor infiltrating lymph cells (TILs) were assayed by flow cytometry to detect the population of CD8+ T cells (h) gated within CD45+ T cells. The expression of Granzyme B (i) and activation markers (j) in CD8+ T was determined and quantified with flow cytometry assay. MFI, mean fluorescence intensity. Values represent mean ± SEM. $^*P < 0.05$, $^{**}P < 0.01$, $^{***} P < 0.001$.